4

Ocean Wave Energy Harvesting

4.1 Introduction to Ocean Wave Energy Harvesting

Uneven heating around the globe results in winds that generate ocean waves. As a result, water particles adopt circular motions as part of the waves [1,2]. This motion carries kinetic energy and the amount of this energy is related to the speed and duration of the wind, the depth, and area of the water body affected by the wind, and the seabed conditions. Waves occur only in the volume of the water closest to its surface, whereas in tides, the entire water body moves, from the surface to the seabed [2]. The total power of waves breaking around the world's coastlines is estimated at 2–3 million megawatts. The west coasts of the United States and Europe and the coasts of Japan and New Zealand are good sites for harnessing wave energy [1].

Ocean wave energy systems convert the kinetic and potential energy contained in the natural oscillations of ocean waves into electricity. There are a variety of mechanisms for the utilization of this energy source. One method to harness wave energy is to bend or focus the waves into a narrow channel of concentration, to increase their power and size. Then waves can be channeled into a catch basin or used directly to spin turbines [1]. The energy of the waves is converted into electricity by means of surge devices and oscillating column devices. Wave energy conversion (WEC) is one of the most feasible future technologies; however, since it is not mature enough, construction cost of wave power plants are considerably high. These energy systems are not developed and maturated commercially due to the complexities, sea conditions, and difficulty of interconnection and transmission of electricity through turbulent water bodies. In addition, they may require higher operation and maintenance costs in comparison to the land power systems due to their location at sea.

A typical ocean wave energy harvesting system consists of a wave power absorber, a turbine, a generator, and power electronic interfaces. The absorber captures the kinetic energy of the ocean waves. The absorbed mechanical kinetic energy of the waves is either conveyed to turbines or the absorber directly drives the generator. The turbine is used to drive the shaft of the electric generator. Turbines are generally used with systems that feature rotational generators. In other methods, a linear motion generator is used, and this can be directly driven by the power absorber or movement of the device. Both linear and rotational generators produce variable frequency and variable amplitude AC voltage. This AC voltage is rectified to DC voltage in order to take advantage of the DC energy transmission capabilities of salty ocean water. DC transmission in salty water does not require an additional cable for the negative polarity. Thus, it will be more cost-effective than transmitting the power in AC form, which requires three-phase cables. Transmission cable length varies depending on the location of the application, which is either nearshore or offshore. However, the principles are the same for both types of applications. After the DC

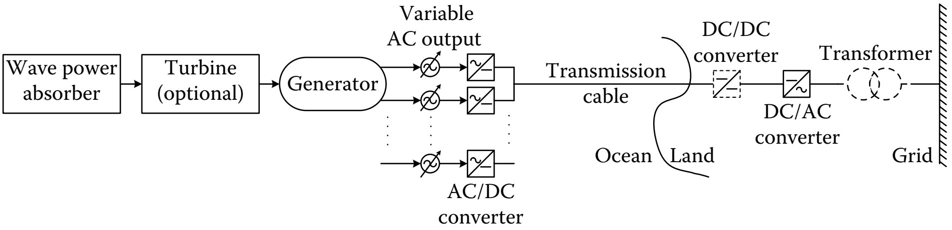

FIGURE 4.1 System-level diagram of ocean wave energy harvesting.

power is transmitted from ocean to land, a DC/DC converter or a tap-changing transformer is used for voltage regulation. Depending on the utilized voltage regulation system, a DC/AC inverter is used before or after the voltage regulator. The voltage synchronization is provided by the inverter and the output terminals of the inverter can be connected to the grid.

Figure 4.1 shows a system-level diagram of the ocean wave energy harvesting. WEC devices (including the absorber, turbine, and generator) are interconnected within an in-water substation. The substation consists of the connection equipments and controllers for individual devices. The outputs of the generators are connected to a common DC bus using DC/AC converters for transforming power before transmission to the shore. A transmission line connects the cluster to the shore. An onshore inverter converts the DC voltage to a 50 or 60 Hz AC voltage for grid connection. An optional shore transformer with tap changer or a DC/DC converter compensates the voltage variations. A group of an absorber, a turbine, and generators could be used in a farm structure to increase the amount of captured energy.

Alternatively, the land converters might be moved offshore to overcome in-land space limitations. The converters can be placed on a platform or enclosed in a buoy anchored to the seabed. However, this adds a level of complexity to the system and may require more maintenance than in-land converters. Figure 4.2 shows a land DC/DC converter moved offshore.

Another option is installing an offshore transformer as seen in Figure 4.3. This would increase the power transmission capability, since the higher voltage transmission will result in less transmission losses, since, for the same power rating, the current will be lower with a higher transmission voltage level. However, this case does not allow for DC transmission.

As an alternative, boost DC/DC converters can be installed after the AC/DC converter of the generator. This allows a high-voltage DC transmission link as illustrated in Figure 4.4. In this case, both transmission losses will be kept at a minimum and only the single-line DC transmission through the ocean water will be needed. The disadvantage of this configuration is that more power components will be used with some additional losses and additional cost will be required to install the boost converter.

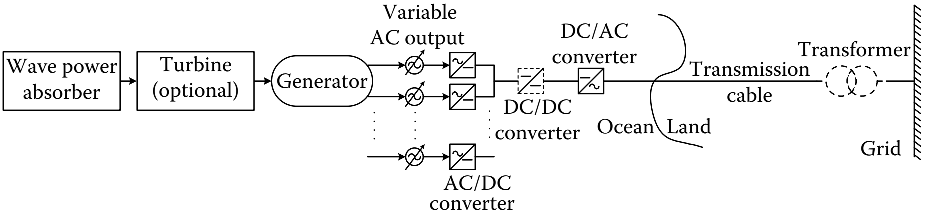

FIGURE 4.2 System-level diagram; the land DC/DC converter is moved offshore.

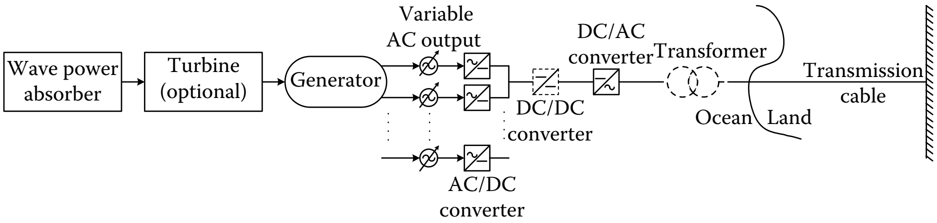

FIGURE 4.3 System-level diagram with the offshore transformer.

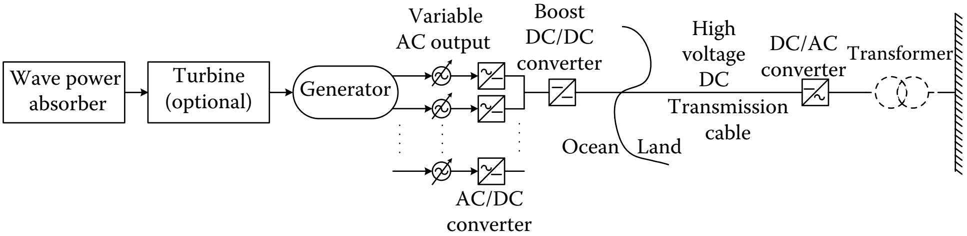

FIGURE 4.4 System-level diagram with the high voltage DC transmission link.

4.2 The Power of Ocean Waves

The physics of ocean waves and wave spectra are explained by Van Dorn in [3]. In Figure 4.5, the characteristics of two types of waves with different periods are presented. These two types of waves represent the main categories of ocean waves.

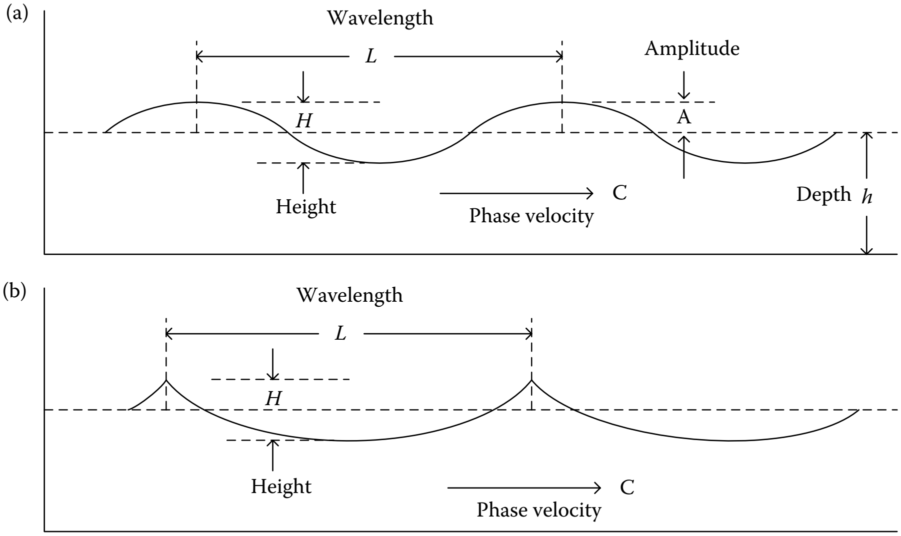

FIGURE 4.5 Characteristics of a wave. (Modified from W.J. Jones and M. Ruane, "Alternative electrical energy sources for Maine, Appendix I, Wave Energy Conversion by J. Mays," Report No. MIT-E1 77-010, MIT Energy Laboratory, July 1977.)

Figure 4.5a shows periodic, progressive surface waves resembling a sinusoidal curve, which is symmetrical around the equilibrium water level. In Figure 4.5b, the waves have higher periods and no longer are sinusoidal or symmetric. Their crests are peaked, and extend higher above the equilibrium level than the long and smooth troughs, which fall below it.

The total energy in an ocean wave can be calculated in joules per unit of width of wave front by summing up the potential and kinetic energy together. The potential energy in a wave of length L is generated by the displacement of the water away from the mean sea level. The kinetic energy of a wave is a result of both horizontal and vertical water particle motions [4].

The total potential and kinetic energy of an ocean wave can be expressed as

$$E = \frac{1}{2}\rho g A^2, \tag{4.1}$$

where g is the acceleration of gravity (9.8 $\mathrm{m/s^2}$), ρ is the density of water (1000 $\mathrm{kg/m^3}$), and A is the wave amplitude (m). To obtain the average energy flux or power of a wave period, energy E is multiplied by the speed of wave propagation, v_g.

$$v_g = \frac{L}{2T}, \tag{4.2}$$

where T is the wave period (s) and L is the wavelength (m) [4].

$$P_{\mathrm{w}} = \frac{1}{2}\rho g A^2 \frac{L}{2T}. \tag{4.3}$$

The dispersion relationship describes the connection between the wave period T and the wavelength L as

$$L = \frac{gT^2}{2\pi}. \tag{4.4}$$

If Equation 4.4 is substituted into Equation 4.3, the power or energy flux of an ocean wave can be calculated as

$$P_{\mathrm{w}} = \frac{\rho g^2 T A^2}{8\pi}. \tag{4.5}$$

Instead of using the wave amplitude, wave power can also be rewritten as a function of wave height, H. Considering that the wave amplitude is half of the wave height, the wave power becomes

$$P_{\mathrm{w}} = \frac{\rho g^2 T H^2}{32\pi}. \tag{4.6}$$

See Refs. [3] and [5] for additional calculations.

4.3 Wave Energy Harvesting Technologies

Various methods have been proposed for converting wave energy into practically usable electrical energy. Some of the early examples of the wave power systems are the Salter Cam developed in England [6,7], a hinged floating system developed in England [8], a pressure-activated submerged generator developed by Kayser [9,10] in Germany, the wave-powered pump developed at Scripp's Institution of Oceanography [10,11], and a pneumatic wave converter originally developed by Masuda [12,13] in Japan. The first four systems are large-scale energy generation systems and the last one is used as a low-level power supply for navigation buoys.

Current experimental and theoretical researches indicate that up to 90% of the wave's power can be extracted given certain conditions. Thus, the ocean wave power can be efficiently converted into electrical energy [4]. The total conversion efficiency of wave energy is around 35% when considering all the ancillary conversion processes throughout the year [4]. The major issue with wave energy production is integrating this unsteady and unpredictable energy source into the grid. Although the wave energy has zero fuel cost, it has a relatively high capital cost and an output that is ever-changing and mostly unpredictable.

Generally, there are two types of wave energy generation sites with respect to their distance from the shore, which are discussed in detail in the following subsections.

4.3.1 Offshore Energy Harvesting Topologies

Offshore applications are located away from the shore and they generally use a floating body as wave power absorber and another body that is fixed to the ocean bottom. Salter Cam and buoys with air-driven turbines are the only applications involving rotational generators in offshore applications. Generally, linear generators with buoys are used in offshore applications. Linear generators are directly driven by the movement of a floating body on the ocean. Before classifying the offshore applications, dynamics of fixed and floating bodies are discussed in this section.

4.3.1.1 Dynamics of Fixed Bodies in Water

When waves hit a body fixed to the ocean bottom, such as a pier or an offshore platform, the waves will dispatch around the body relative to the geometrical shape of the wave and body, which dictate the reflection of the incident waves from the body [4].

If the body does not extend continuously to the bottom below the free surface, some of the wave energy may leak underneath the structure. The energy of a wave is distributed from the surface down to the bottom exponentially and is not localized only at the surface. At a depth of approximately one-half wavelength, the wave effect can be considered to be negligible [4].

A two-dimensional (2D) case of a fixed cylinder is shown in Figure 4.6. The incident wave of the height H_I is partially reflected by the cylinder, while the rest of the energy in the wave is transmitted through the cylinder to the other side, where it can behave as a wave again and continue on its way. In an ideal case with no power loss, the amount of energy in the incident wave must be equal to the sum of the energies of the transmitted wave and the reflected wave:

$$\frac{1}{2}\rho g\left(\frac{H_\mathrm{I}}{2}\right)^2 = \frac{1}{2}\rho g\left(\frac{H_\mathrm{T}}{2}\right)^2 + \frac{1}{2}\rho g\left(\frac{H_\mathrm{R}}{2}\right)^2. \tag{4.7}$$

Here, H_T is the height of the transmitted wave, H_R is the height of the reflected wave, and H_I is the height of the incident wave.

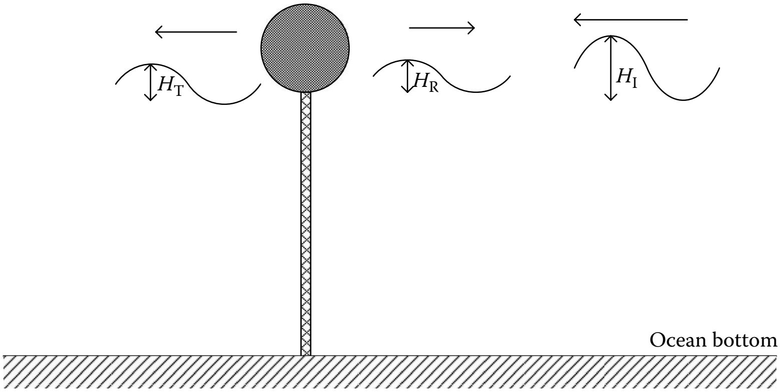

FIGURE 4.6 Side view of a fixed body in waves showing incident, reflected and transmitted waves. (Modified from W.J. Jones and M. Ruane, "Alternative electrical energy sources for Maine, Appendix I, Wave Energy Conversion by J. Mays," Report No. MIT-E1 77-010, MIT Energy Laboratory, July 1977.)

This wave interaction can cause considerable forces on the body, although it is assumed that the waves are not of the braking kind. During the breaking of the waves on shore, a significant amount of energy is lost in the resulting turbulence [4]. If we replace the cylinder with a sphere, the behavior is similar, with some differences in the reflection of the waves around the sides. The diffracted waves appear as a complicated pattern of the interfering waves. Also, in this case, more wave energy leaks under the sphere compared to the cylinder case [4].

4.3.1.2 Dynamics of Floating Bodies in Water

In the floating body case, the same cylinder is assumed to be freely floating on the ocean. The motions of a floating body can be defined as: heave, sway, and roll corresponding to vertical, horizontal, and rotational motions as shown in Figure 4.7 according to the terminology of naval architecture.

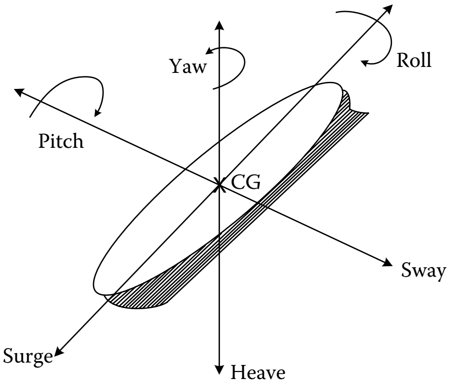

FIGURE 4.7 Directions of motion of a floating body. (Modified from W.J. Jones and M. Ruane, "Alternative electrical energy sources for Maine, Appendix I, Wave Energy Conversion by J. Mays," Report No. MIT-E1 77-010, MIT Energy Laboratory, July 1977.)

If the cylinder is pushed up and down, waves are created, which will spread out from either side. Similar behavior is expected if we cause it to sway by pushing it from side to side. No disturbance to the water would be caused by rolling the object, if it is a perfect circular cylinder without roughness. If the shape is generalized to a box, it is expected to create waves when disturbed [4].

Thus, a combination of waves is expected as a result of causing the body to move in different manners. Three additional types of motion are the surge, yaw, and pitch [4] as shown in Figure 4.7.

Floating devices can generate electricity from the bobbing action of a floating object. The object can be mounted to a floating raft or to a device fixed on the ocean floor. These types of devices can be used to power lights and whistles on buoys.

4.3.1.3 Air-Driven Turbines

WEC is generally composed of several stages. In air-driven turbine systems for nearshore and offshore applications, the primary conversion is from wave to the pressurized air. The secondary stage is extracting the mechanical energy of the pressurized air to the rotation of the shaft of the turbine. The last stage is converting the mechanical rotation into electric power through electric generators.

Figure 4.8 shows the operating principle of an offshore application, which consists of a floating buoy with an air chamber and an air-driven generator. In this system, when the waves hit the body, the water level inside the channel of the buoy increases. This increase in water level applies a pressure to the air in the air chamber. When the air is pressurized, it applies a force to the ventilator turbine and rotates it. This turbine drives the electric generator, creating electricity at its output terminals. When the waves are pulled back to the ocean, the air in the air chamber is also pulled back as the water level in the buoy channel decreases. Due to the syringe effect, the turbine shaft rotates into the contrary direction, still producing electricity.

In order to achieve maximum efficiency during the syringe effect, the air chamber and the ventilating generator should be carefully mechanically insulated. However, this adds design complexity and further cost to the system.

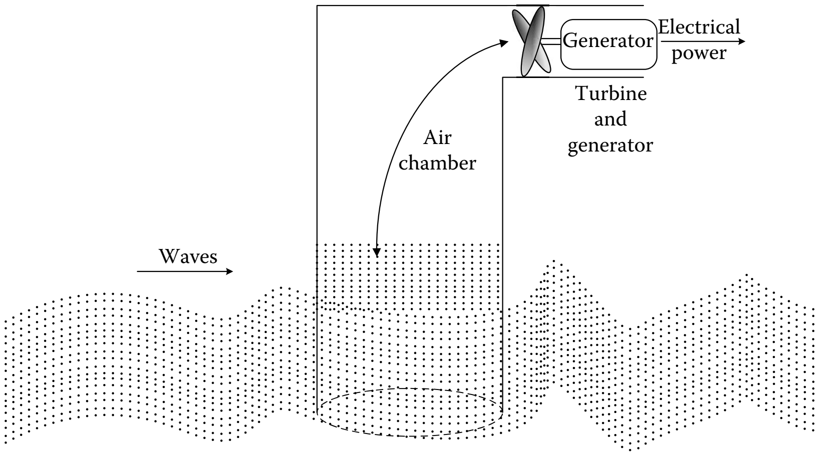

FIGURE 4.8 Spinning the air-driven turbines using wave power. (Modified from "Ocean Energy," Report of the U.S. Department of Interior Minerals Management Service.)

4.3.1.4 Fixed Stator and Directly Driven PM Linear Generator–Based Buoy Applications

The idea is based on the height difference of the wave from top and bottom. The buoy follows the motion of the wave when it is floating on the ocean surface. The buoy can move vertically on a pillar, which is connected to a hull. PMs are mounted on the surface of the hull, and coil windings on the outside of the hull. The pillar and stator are connected on a foundation standing on the seabed of the ocean. The hull with the mounted magnets is called the rotor or the piston of the generator, and they are the moving parts of the generator. Since the motion is linear, this generator is called a linear generator.

The illustration of linear generator in use with the floating buoy and fixed pillar is shown in Figure 4.9.

Due to the varying amplitude and period of the ocean waves, the amplitude and frequency of the output voltage of the generator varies. Thus, an AC/DC rectifier followed by a DC/AC converter is required to make the grid connection possible.

One drawback of linear generators might be the fact that the associated large and expensive electromagnetic converters may generate flux changes that are too slow due to the low velocities. However, the latest developments in linear generators have increased the interest in using linear generators for wave energy applications.

The preferable geometry of a buoy is a cylindrical shape since it can act as a point absorber and intercept waves coming from different directions. When the wave rises, the buoy pulls the generator piston by the rope. When the wave subsides, the generator will be drawn back by the spring that stores the mechanical energy in the first case. Thus, the electric generation is provided during both up and down motion.

The generator AC voltage starts at zero when the buoy is in its lowest position, increases until the buoy reaches its highest position at the top of the wave and descends back to zero as the buoy stops.

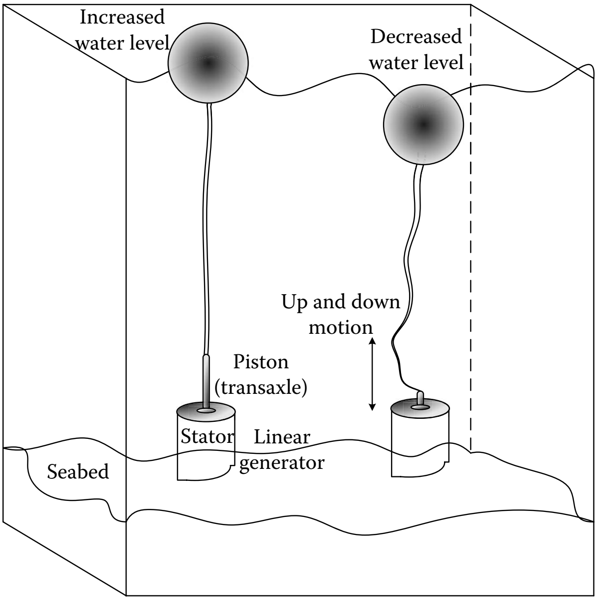

FIGURE 4.9 Linear generator–based buoy-type wave energy harvesting method.

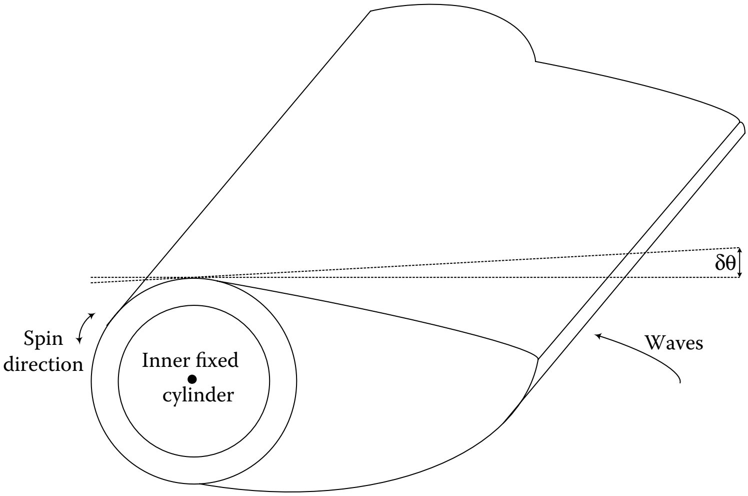

FIGURE 4.10 Side view of Salter Cam.

4.3.1.5 Salter Cam Method

Salter Cam is shown in Figures 4.10 and 4.11. Salter Cam, also known as "the nodding duck," features an outer shell that rolls around a fixed inner cylinder that is activated by the incoming waves. The power can be captured through the differential rotation between the cylinder and the cam. In this application, the motion of the cam is converted from wave into a hydraulic fluid, and then the hydraulic motor is used to convert the pressurized hydraulic fluid into rotational mechanical energy. Consequently, the rotational mechanical energy is converted to electricity by utilizing electric generators. As an intermediate step,

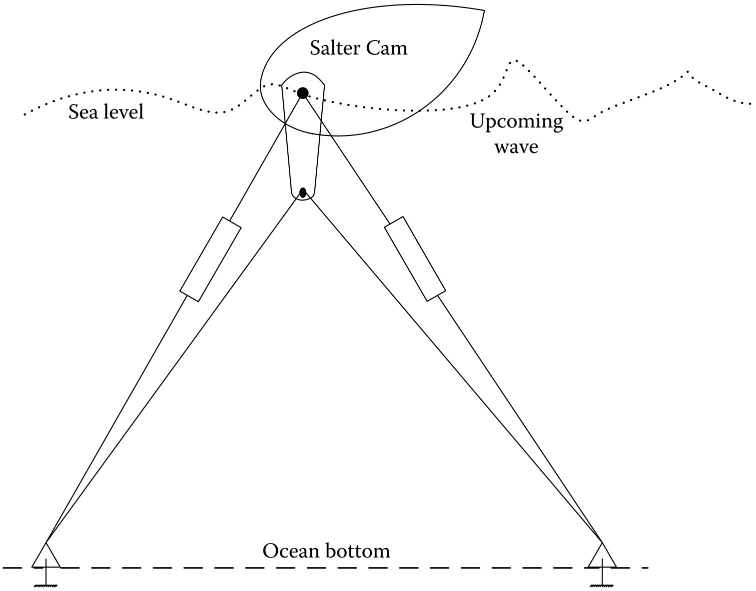

FIGURE 4.11 A schematic illustrating the fixing of the Salter Cam WEC device.

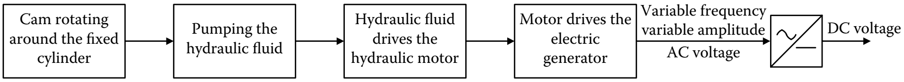

FIGURE 4.12 Operating principle of the Salter Cam.

flywheels or pressurized liquids can be used in order to reduce the intermittencies of the wave power in conversion to electric power.

The inner cylinder is fixed to the ocean bottom through hawser lines as shown in Figure 4.11.

The shape of the Salter Cam allows a large interaction with the incident wave. The shape should not generate a wave on its backside during the roll over due to its cylindrical backside [4].

The Salter Cam WEC generates electric power through the harmonic motion of the free part of the device around the fixed inner cylinder. The outer part rises and falls with respect to the motion caused by the ocean waves. This motion pumps a hydraulic fluid that drives a hydraulic motor. This motor is coupled to the shaft of an electric generator that generates electricity. The block diagram explaining the operation principle of the Salter Cam is shown in Figure 4.12. The Salter Cam is extremely efficient in energy production and its applications have gained a lot of interest recently.

The cam acts as a damped harmonic oscillator in that it exhibits a resonant behavior at certain wavelengths. This damped pendulum consists of a mass located either at the end or distributed along the length of a rod (body of the cam), a restoring force due to gravity (hydrostatic force on the cam), and a damping force in the opposite direction of the motion caused by the viscosity of the medium (internal energy absorber of the cam) as shown in Figure 4.13.

When displaced away from the current stall position, it is expected that the pendulum (cam) oscillates for a few cycles until its motion has been thoroughly damped. If, however, a force is applied in a periodic manner, then the pendulum (cam) is expected to oscillate at its driven period. The amplitude of the motion not only depends on how hard it is pushed, but also on the natural period of the device, which is determined by gravity, cam geometry, and wave force. This period may be in the order of seconds [4].

In Salter Cam [6,15,16], there is a "string" or common spine, which provides a stable frame of reference along the roll. The cams run on rollers, which are the bodies of rotary pumps.

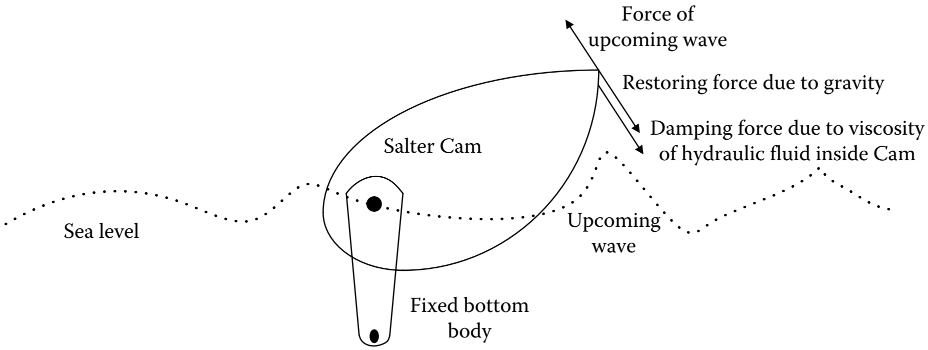

FIGURE 4.13 Forces affecting a Salter Cam.

High-pressure oil drives hydraulic swash-plate motors coupled to electric generators. Electrical transmission is provided by undersea cables.

In deepwater, the wave power spatial flux (in kW/m of wave front crest) is given by the wave height (H_S in m) and the peak wave period (T_p in s). Based on these two parameters, the incident wave power (J in kilowatts per meter of wave crest length, or kW/m) associated with each sea state record, assuming 84% efficient wave power turbine, is estimated by the following equation:

$$J = 0.42 \times (H_S)^2 \times T_p. \tag{4.8}$$

It should be noted that wave power varies with the square of wave height—in other words, if the height of the wave doubles, the generated power will be increased four times [2].

4.3.2 Nearshore Energy Harvesting Topologies

Nearshore topologies are applied to the shore or within the surfing zone of the ocean. Nearshore applications have some advantages and disadvantages in comparison to the offshore applications with respect to the selected method. The different nearshore applications are described in the following section.

4.3.2.1 Nearshore Wave Energy Harvesting by the Channel/Reservoir/Turbine Method

In order to harness the wave energy, wave currents can be funneled into a narrow channel to increase their power and size. The waves can be channeled into a catch basin and used directly to rotate the turbine as shown in Figure 4.14. This method is more expensive in comparison to the other offshore applications, since it requires building a reservoir to collect the water carried by the waves to drive the turbine. However, all the components of the WEC system are located inland, and this results in easier and less maintenance in comparison to the offshore applications. Additionally, since a reservoir collects the ocean water, the intermittencies can be eliminated with respect to the size of the reservoir. This will create a convenient platform for voltage and frequency regulation. However, it will be more advantageous to build this type of plants in the locations where they have regular and sustaining wave regimes.

4.3.2.2 Air-Driven Turbines Based on the Nearshore Wave Energy Harvesting Method

Another way to harness wave energy is with an oscillating water column (OWC) that generates electricity from the wave-driven rise and fall of water in a cylindrical shaft or pipe. The rising and falling water drives air into and out of the top of the shaft, powering an air-driven turbine as shown in Figure 4.15.

Figure 4.15a shows the general structure of the nearshore air-driven turbine. When the wave fills in the wave chamber, it pushes the air through the ventilator, which drives the electrical machine as shown in Figure 4.15b. In Figure 4.15c, the wave retreats from the wave chamber causing the pressure of the air inside the channel to decrease.

This method is advantageous because it is able to use not only wave power but also the power from the tidal motions. However, mechanical isolation should be provided within wave and air chambers in order to obtain better efficiencies. This will also add some more cost and design complexity to the system.

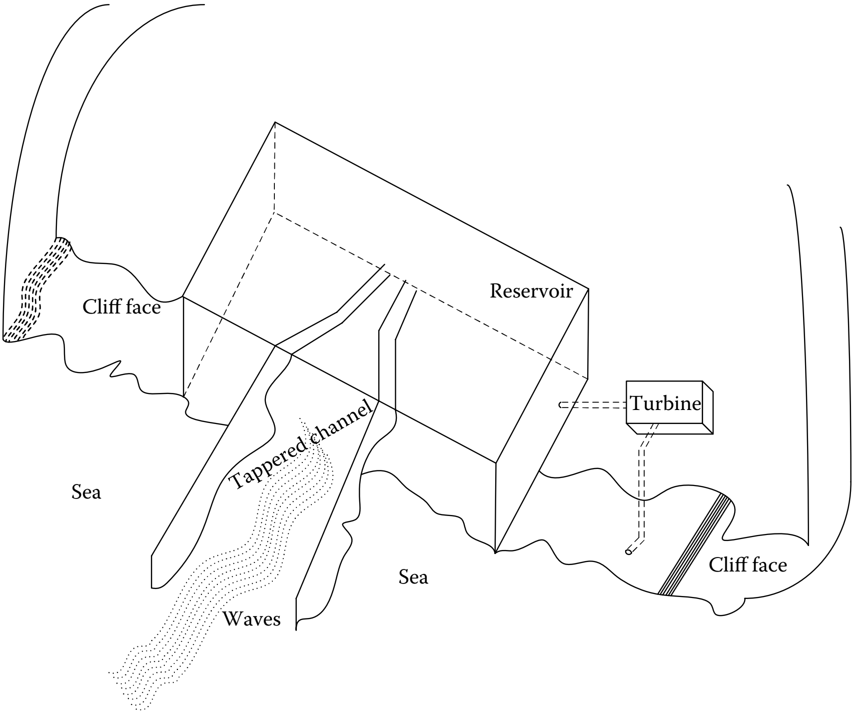

FIGURE 4.14 Channeled ocean wave to a reservoir to spin the turbines.

4.3.3 Wave Power Absorbers

A wave power absorber absorbs the energy of a wave and converts it into mechanical energy that drives the turbines coupled to generators or directly moves the pistons of linear generators. Consequently, the mechanical power is converted to electrical power

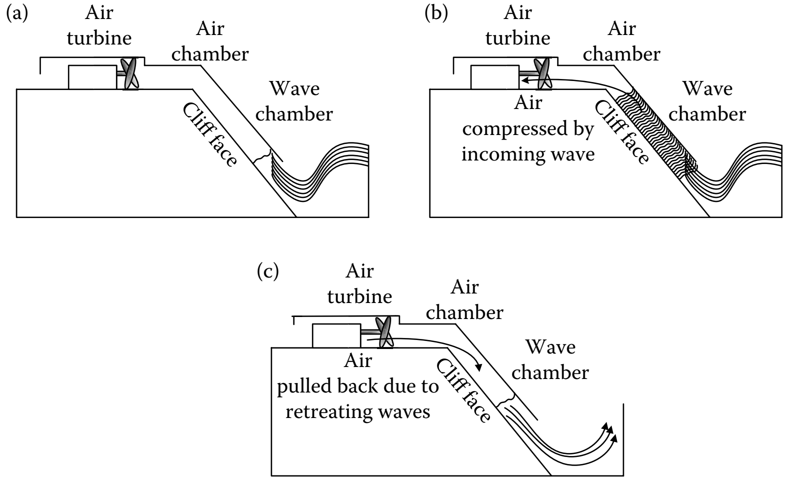

FIGURE 4.15 Air-driven turbines using the wave power [14]. (a) Upcoming wave starts filling the chamber, (b) air is compressed by rising water, and (c) air is pulled back by retreating waves.

by generators. Wave power absorbers used in different applications are discussed in this subsection.

When a floating body is displaced above or below the water position, a restoring force tends to bring the floating body to its original equilibrium position. The force that brings the body back to its equilibrium position results in potential energy. The kinetic energy is associated with the motion of the body [4].

In order to efficiently extract the wave system energy, the mechanical energy given in Equation 4.1 should be considered. The basic principle of wave power absorbers is to take the mechanical energy of the waves, which can be then converted into electrical energy. Pumps, flywheels, compressors, turbines, and linear or rotational generators are the devices that could be used for wave energy extraction as mechanical energy converters [4].

There are several studies reported in the literature to harness the power of ocean waves [17–19]. Isaacs [13] outlines some of the proposed modes of operation for those devices including the Scripps wave pump. In [20], Richards reviews the buoy-shaped wave-activated turbine generators. The designs of Masuda, McCormic, Isaacs, Kayser (Figures 4.16 and 4.17), and Falnes are one of those designs.

In these devices, the heave motion of a cylindrical buoy is used to provide a pressure head, which then drives a turbine generator by hydraulic or pneumatic methods. In Figure 4.16, Masuda units of 70 and 120 W are shown, which is used by the Japanese Maritime Safety Agency. Masuda has also proposed a floating, octahedral shaped buoy (Figure 4.17) with an outside diameter of 120 m, which is expected to produce 3–6 MW in the high seas in Japan.

A wave contouring raft whose joints are formed by hydraulic pumps operating on the differential motions of the linked rafts as shown in Figure 4.18 was proposed by Wooley and Platts. The details of this method were discussed in Ref. [4]. This method has been experimented by Wavepower Ltd of Southampton, England. The individual rafts are built at a length of one-quarter of the wavelength of the waves that, on the average, contribute the greatest amount of energy. The rafts would be somewhat wider than their length in the direction of the advancing wave.

Cylindrical buoys are preferable due to their ability to extract energy from the wave system that is in excess of their diameters and they are not sensitive to the wave direction.

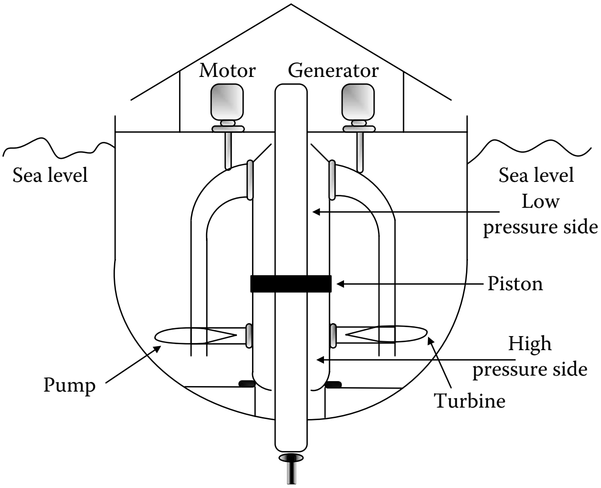

FIGURE 4.16 Falnes buoy-shaped wave-activated turbine.

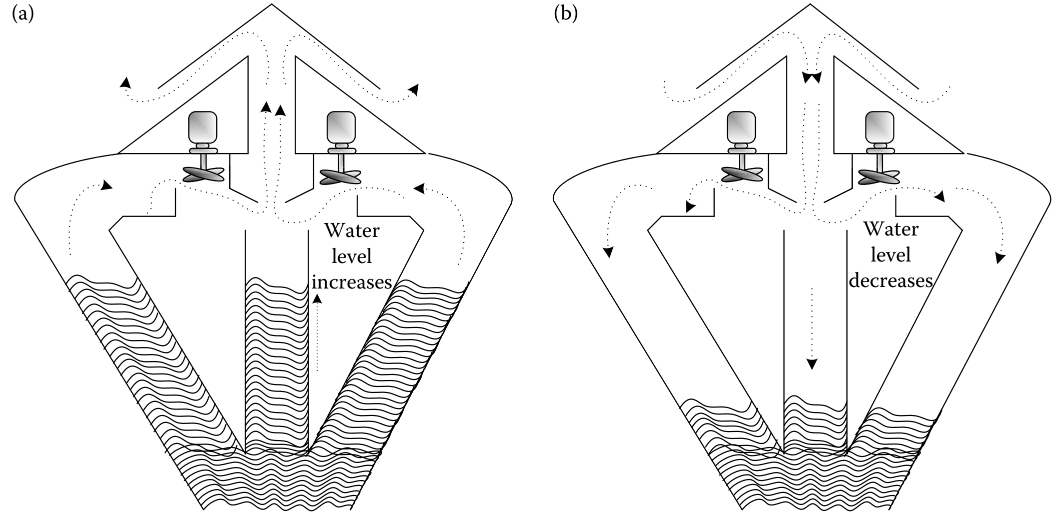

FIGURE 4.17 Air pressure ring buoy. (a) Water level increases and air is taken out from the upper outlets. (b) Water level decreases and air is pulled back from the upper inlets.

The power or energy flux in a wave is about H^2T of the wave front. The floating body can extract an amount of power greater than that of intercepted waves by the diameter of the body because of the diffracted and radiated waves [4].

An array of these devices can capture more of the wave energy with the proper devices to control their motions with respect to one another and the incident waves. In [21], it is reported that an array of floating bodies spaced a wavelength apart are capable of coordinating operation in two modes such as heave and roll and they may extract 100% of the incident wave energy.

4.3.4 Wave Power Turbine Types

In this subsection, some of the most common wave power turbines that are coupled to the rotational generators for wave energy applications are discussed. These devices are generally installed within fixed structures to the shoreline. Since they are fixed, they provide an appropriate frame for wave forces that come against them so that they can have high conversion efficiencies.

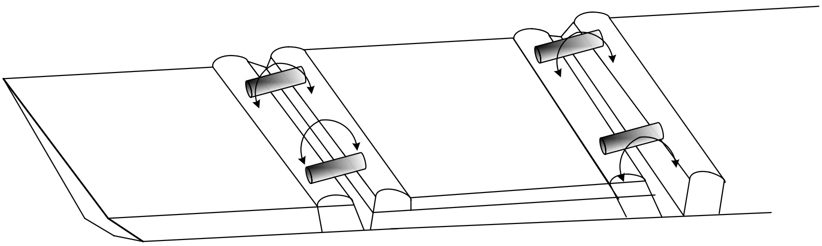

FIGURE 4.18 Wave contouring raft.

4.3.4.1 The "Wells" Air Turbines

The Wells turbines, which are low-pressure air turbines, are commonly used in OWC applications. Using Wells turbines eliminates the need for expensive and delicate valve systems to rectify the direction of the airflow.

OWCs are used as shore-mounted structures and they have fixed frames of references to meet the wave forces. The OWCs are essentially resonant devices and they operate in response to the incoming wave activity [22]. The pressure of the water inside the column increases due to the incident wave crest. The internal water level rises and in turn it pushes air out from the top of the column [22]. This airflow rotates the air turbine. Then the airflow reverses and flows into the column again when the waves are dragged back to the ocean.

OWCs use Wells turbines, which are self-rectifying air turbine as shown in Figure 4.19 [22], and do not need additional rectifying valves. Wells can extract energy from incoming or outgoing airflows to/from the air column. The Wells turbine has a low drag and can be driven at high rotational speeds of several hundred rpm without the need for a gearbox. The efficiency of Wells rotor is the highest when the air pressure is corresponding to 2–3 m of water rise in the column, which is the typical ocean wave height.

The airflow in both directions produces a forward thrust on the blades. Even though the airflow is bidirectional, the turbine spins unidirectionally.

The block diagram of the Wells turbine, which drives the generator of the wave power system, is given in Figure 4.20. The input of the turbine model is air velocity, which is caused by the pressure increase in the column and the output of the model is the mechanical torque that drives the generator [23,24].

The output mechanical torque is

$$T_\mathrm{m} = \frac{P_\mathrm{shaft}}{\omega_\mathrm{m}}, \tag{4.9}$$

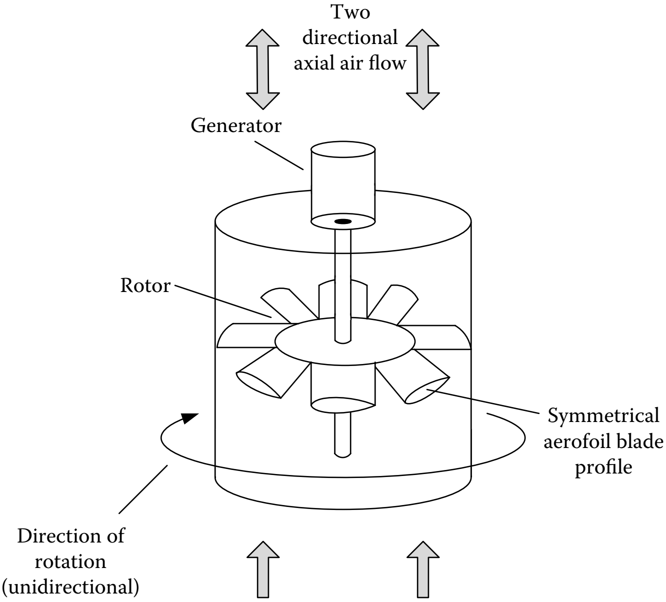

FIGURE 4.19 The Wells turbine.

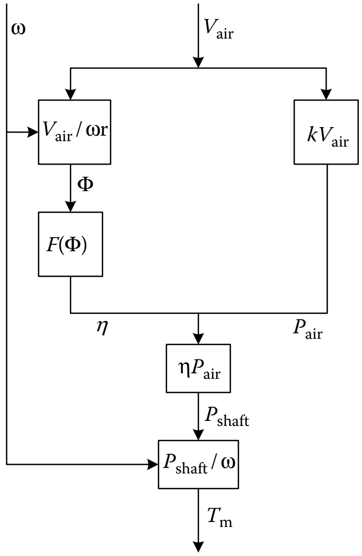

FIGURE 4.20 Block diagram of the Wells turbine.

where P_{shaft} is the power of the turbine shaft and ω_m is the angular speed of the turbine shaft. The shaft power P_{shaft} can be calculated by

$$P_{shaft} = \eta P_{air}, \tag{4.10}$$

where η and P_{air} are the efficiency of the turbine and air power, respectively. The turbine efficiency is a function of flow coefficient, Φ. Turbine efficiency versus flow coefficient is shown in Figure 4.21.

The air power is proportional to the air velocity as

$$P_{air} = kV_{air}, \tag{4.11}$$

where k is the proportion constant.

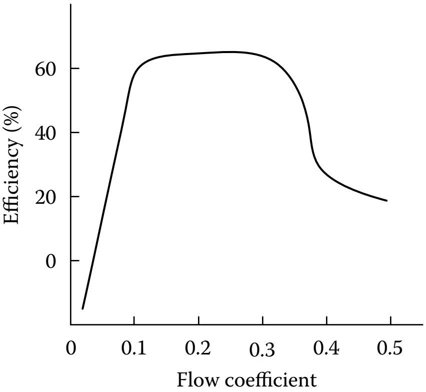

FIGURE 4.21 Turbine efficiency as a function of flow coefficient.

The flow coefficient Φ can be determined as

$$\Phi = \frac{V_{\mathrm{air}}}{\omega_{\mathrm{m}} r}, \tag{4.12}$$

where r is the turbine radius.

The turbine output torque has a pulsating form. In other words, the output waveform of the torque has oscillations with respect to the airflow. Since the air velocity at the turbine input is related to the wavelength and wave height, coupling a flywheel with high inertia can make the turbine output torque smoother. The flywheel location is along the shaft between the turbine and the induction generator [23,24].

The block diagram of a Wells turbine given in Figure 4.20 can be realized using MATLAB and Simulink. An example of a pulsating waveform of a Wells turbine is given in Figure 4.22 for the inertia $J = 0.02\,\mathrm{kg\,m^2}$, power conversion proportion constant $k = 0.5$, and radius of the turbine $r = 1\,\mathrm{m}$, for a small-scale Wells turbine.

4.3.4.2 Self-Pitch-Controlled Blades Turbine for WEC

The working principle, characteristics, and behavior of the self-pitch-controlled blades turbine is explained in this subsection [25]. The operating principle of the turbine using self-pitch-controlled blades is explained through Figure 4.23. This turbine is suitable for WEC and it can be used as an alternative for Wells turbines.

The turbine blade can oscillate between two predefined angles of $\pm\gamma$, which are set on the hub by a pivot near the leading edge [25]. The turbine blades can flip by themselves when an airfoil experiences a pitching moment, M, at a certain angle of incidence about the pivot. They can flip $+\gamma$ or $-\gamma$ depending on the flow direction. Therefore, the turbine's higher torque and higher operating efficiency is obtained with a lower rotating speed.

The torque coefficient C_{T} and the input power coefficient C_{A} versus the flow coefficient Φ are used for evaluating the turbine's characteristics under steady-state flow conditions.

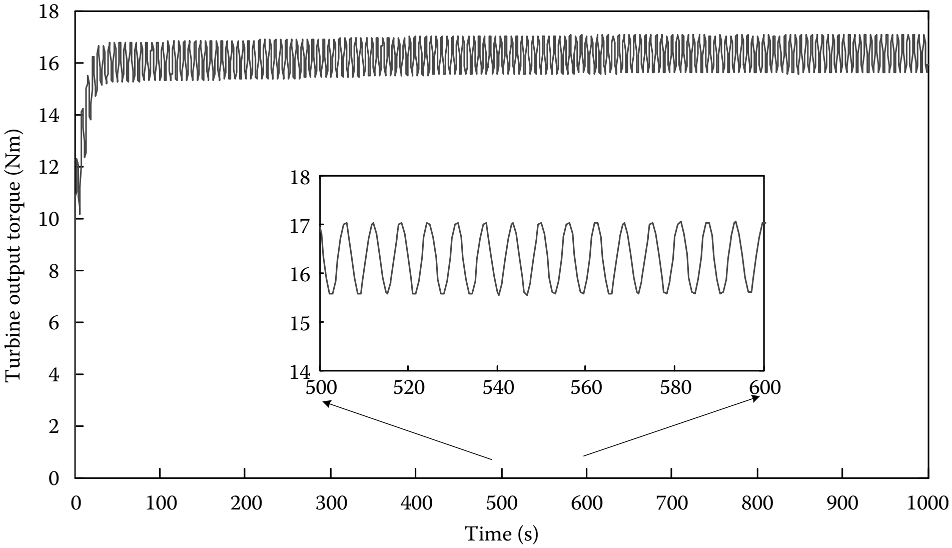

FIGURE 4.22 Output torque waveform of the Wells turbine with sinusoidal input airflow.

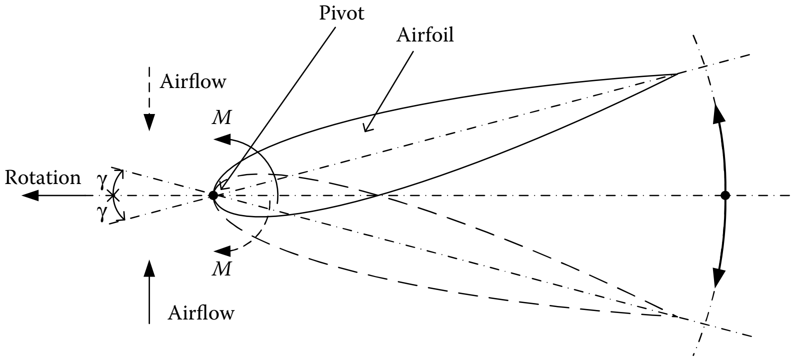

FIGURE 4.23 Turbine using self-pitch-controlled blades for WEC.

These coefficients are defined as

$$C_T = \frac{T_0}{\left[\rho(v^2 + U_R^2)blzr_R/2\right]}, \tag{4.13}$$

$$C_A = \frac{\Delta pQ}{\left[\rho(v^2 + U_R^2)blzv/2\right]}, \tag{4.14}$$

$$\phi = v_a/U_R, \tag{4.15}$$

where ρ is the air density, v is the mean axial flow velocity, U_R is the circumferential velocity at mean radius (r_R), b is the rotor blade height, l is the chord length, Δp is the total pressure drop between before and after the turbine, T_0 is the output torque, and z is the number of rotor blades [25].

The C_T–Φ characteristics vary with respect to the different blade angles. The C_T value decreases if γ increases in the stall-free region. This shows that the larger γ results in better starting conditions. Besides, the stall point increases with γ as well as the flow coefficient at no-load condition. The input coefficient C_A is higher at $\gamma = 0$ than nonzero γ values. This is caused by the rotor geometry. If γ is different from zero, the C_A value is negative at small flow coefficients. This means that the rotor acts as a fan at smaller inlet angles.

Thus, the averaged performance of the rotor goes down under an oscillating flow condition if the setting angle is fixed. It is possible to overcome this problem using the self-pitch-controlled blades because the torque at a small relative inlet angle becomes zero [25]. The overall view of a wave energy turbine with self–pitch-controlled blades is shown in Figure 4.24.

According to the previously constructed wave power plants, the axial flow velocity during exhalation such as from the air chamber to the outside is higher than that during inhalation [26–29].

Thus, the optimum setting pitch angle will be different, according to the direction of the airflow. For instance, authors investigated the effect of setting angles on the turbine performances under real sea conditions [25]. The analytical procedure for this performance is explained in [30].

The behavior of rotating systems can be described as

$$I\frac{d\omega}{dt} + T_L = T_0. \tag{4.16}$$

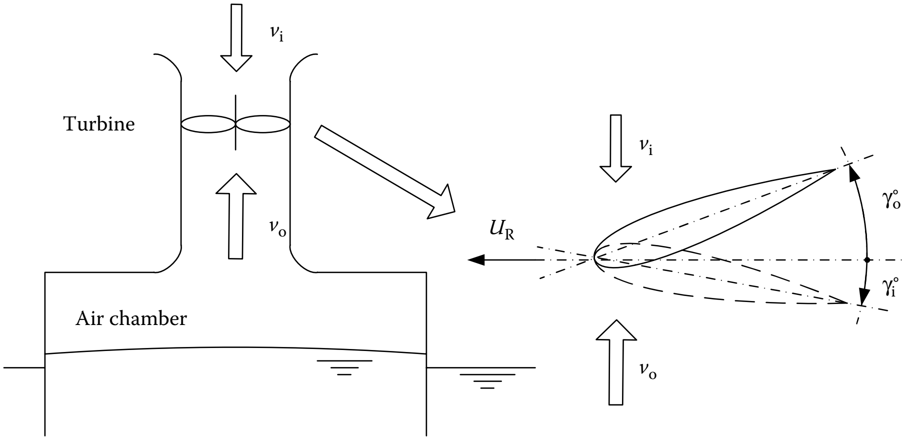

FIGURE 4.24 Overall view of wave energy turbine with self-pitch-controlled blades.

Here, I is the inertia moment of the rotor, t is the time, and T_L is the loading torque. For given values of I, T_L, and T_0, Equation 4.16 can be numerically solved. At the beginning, this gives the starting characteristics of the turbine and provides the running characteristics at the asymptotic condition. The turbine performance can be calculated as a mean efficiency when the solution is in the asymptotic condition:

$$\bar{\eta} = \frac{\left((1/T)\int_0^T T_0\omega\,\mathrm{d}t\right)}{\left((1/T)\int_0^T \Delta pQ\,\mathrm{d}t\right)}. \tag{4.17}$$

$\bar{\eta}$ is evaluated over one wave period, when the rotor is rotating at constant speed. In Equation 4.17 T is the wave period, T_0 is the output torque, ω is the angular rotor speed, and Q is the flow rate (m^3/s). In [25], the effect of different pitch angle variations on the turbine performance (mean efficiency) is presented.

4.3.4.3 Kaplan Turbines for WEC

In this subsection, Kaplan-type hydraulic turbines are described with their structure and operating principles. Kaplan turbines are suitable for both tidal and wave energy applications as well as tapered channel and other hydroelectric applications. These turbines are propeller-type water turbines with adjustable blade angles for speed regulation and torque control.

The fluid changes pressure as it moves through the turbine and transfers its energy to mechanical energy, which makes the turbine an inward flow reaction turbine. The efficiency of the Kaplan turbine is around 90%; however, it might decrease for very low head conditions. The inlet is a tube located around the wicket gate of the turbine. Water is directed tangentially through the wicket gate, which spins the turbine due to the spirals on to a propeller-shaped runner. The outlet is a draft tube used to decelerate the water and recover its kinetic energy.

The turbine does not need any minimum water flow rate since the draft tube remains full of water. A higher turbine location may increase the suction; however, this may result in faster cavitations of the turbine.

Double-regulated turbines have adjustable runner blades, because double regulation involves both wicket gate opening and angle controlling of the runner blades. The most efficient operation can be obtained under varying head, flow, or load conditions by controlling the blade angles and the wicket gate opening. Actual head values and wicket gate opening are used for the determination of the runner blade angle. Combinational dependence of $y_R(y_W, H_b)$ is specified in order to run the turbine at maximum efficiency, regardless of the operating conditions [31]. y_R is the runner blades' servomotor piston position corresponding to runner blades angle, y_W is the guide vanes' servomotor piston position corresponding to wicket gate opening, and H_b is the gross head diameter in meters. This relation is provided by the combinator (cam), called special device, in the turbine control system.

A hydroelectric power conversion system consists of a hydraulic turbine, a governor and a generator, which are shown in Figure 4.25 with double-regulated turbine [31].

Double-regulated hydraulic turbines are used in low-head hydraulic power plants such as WEC plants involving rotational turbines, which are driven by the water flow from the reservoir with short pipelines. Thus, water and cable channel can be considered as incompressible and the inelastic water column equation can be used as follows:

$$\frac{q - q_0}{h - h_0} = -\frac{1}{T_W s}, \tag{4.18}$$

where q and q_0 are the turbine discharge and its initial value (p.u.), respectively, h and h_0 are the turbine head and its initial value, respectively (p.u.), T_W is the water starting time (in seconds) and s is the Laplace operator.

The turbine that drives the electric generator has the mechanical torque at the coupling point, which can be calculated as

$$m = \frac{qh\eta_t}{\omega}, \tag{4.19}$$

where m is the turbine torque (p.u.), η_t is the turbine efficiency, and ω is the speed (p.u.). Head, speed, guide vanes, and runner blades are the parameters affecting the discharge and efficiency of the turbine as

$$q = q(h, \omega, y_W, y_R), \tag{4.20}$$

$$\eta_t = \eta_t(h, \omega, y_W, y_R). \tag{4.21}$$

Hence, the turbine mechanical torque is also affected by these four variables as

$$m = m(h, \omega, y_W, y_R). \tag{4.22}$$

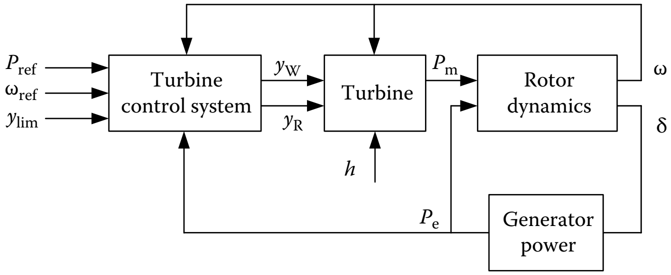

FIGURE 4.25 Double-regulated turbine model with control system and rotor dynamics.

The turbine characteristics define these complex nonlinear functions. The turbine speed is around a fixed value particularly if the power system is connected to the grid. If the speed variations are ignored, the turbine discharge and efficiency characteristics could be written independently from the speed [31] as

$$q = q(h, y_{\mathrm{W}}, y_{\mathrm{R}}), \tag{4.23}$$

$$\eta_{\mathrm{t}} = \eta_{\mathrm{t}}(h, y_{\mathrm{W}}, y_{\mathrm{R}}). \tag{4.24}$$

These characteristics are defined for h_{char}, which is the specific turbine head. For any h value, the turbine discharge determined from the $q(y_{\mathrm{W}}, y_{\mathrm{R}})$ can be recalculated as

$$q = q(y_{\mathrm{W}}, y_{\mathrm{R}})\sqrt{(h/h_{\mathrm{char}})}. \tag{4.25}$$

Additional to the head variations, the turbine efficiency may vary and the efficiency characteristics for specific head h_{char} can be calculated as

$$\eta_{\mathrm{t}} = \eta_{\mathrm{t}}(y_{\mathrm{W}}, y_{\mathrm{R}}). \tag{4.26}$$

Discharge and efficiency functions with Equations 4.23 and 4.24 are used to build the nonlinear model of double-regulated Kaplan turbine. The block diagram of a Kaplan turbine is presented in Figure 4.26 [31].

4.3.4.4 Other Types of Turbines Used for WEC

In this subsection, other turbine types used for WEC applications are reviewed. These turbines are

- Biplane wells turbine with guide vanes (BWGVs), Figure 4.27 [32].
- Impulse turbine with self-pitch-controlled guide vanes (ISGVs), Figure 4.28 [33].
- Impulse turbine with fixed guide vane (IFGV), Figure 4.29 [34].

The different wave turbines are experimentally tested in "Performance comparison of turbines for wave power conversion" [35]. The test rig in this study consists of a settling chamber, a large piston-cylinder, and a test section with 3 m diameter with a bell-mouthed entry and a diffuser exit.

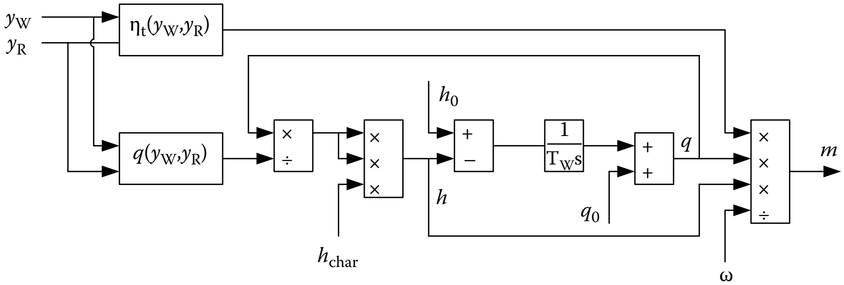

FIGURE 4.26 Nonlinear model of hydraulic turbine.

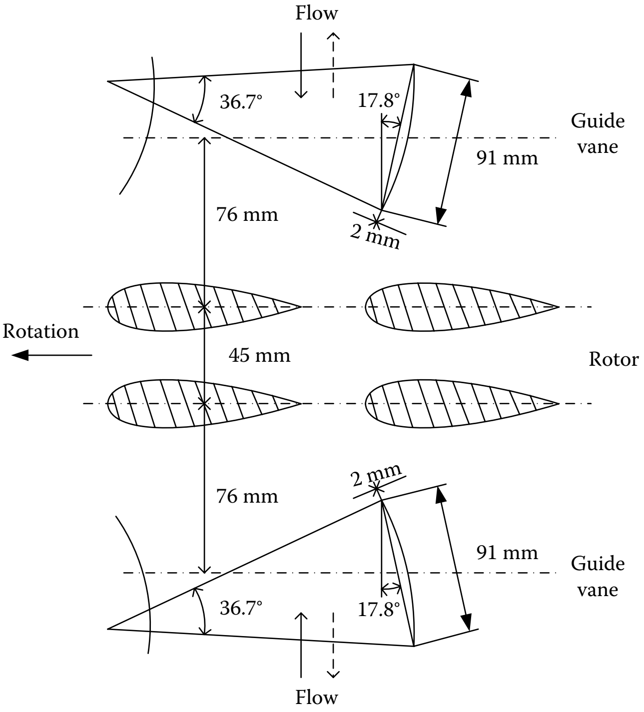

FIGURE 4.27 Biplane wells turbine with guide vanes.

The turbine rotor with $v = 0.7$ hub-to-tip ratio is placed at the center of the test section. Then the turbine rotor is tested at a constant rotational speed under steady-state conditions. The performance of the turbine is evaluated in terms of the turbine angular speed, ω, turbine output torque, T_0, flow rate, Q, and total pressure drop between the inside and outside of the air chamber, Δp. It should be noted that all of the turbines are self-starting [35].

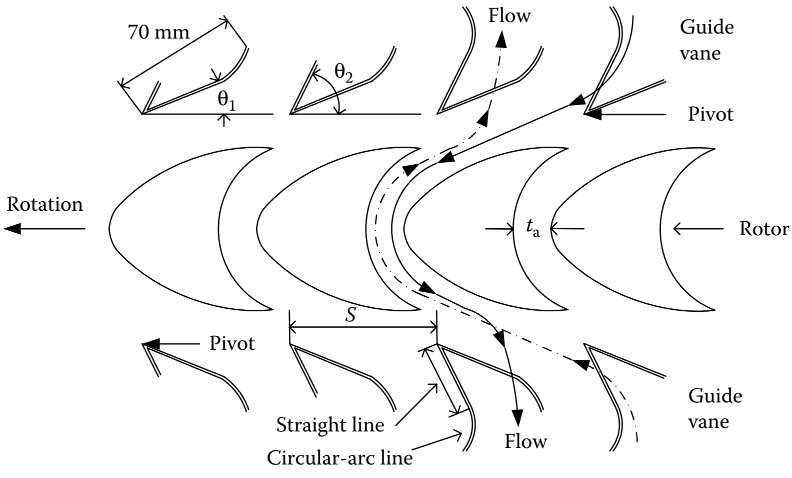

FIGURE 4.28 Impulse turbine with self-pitch-controlled guide vanes by link motion (ISGV).

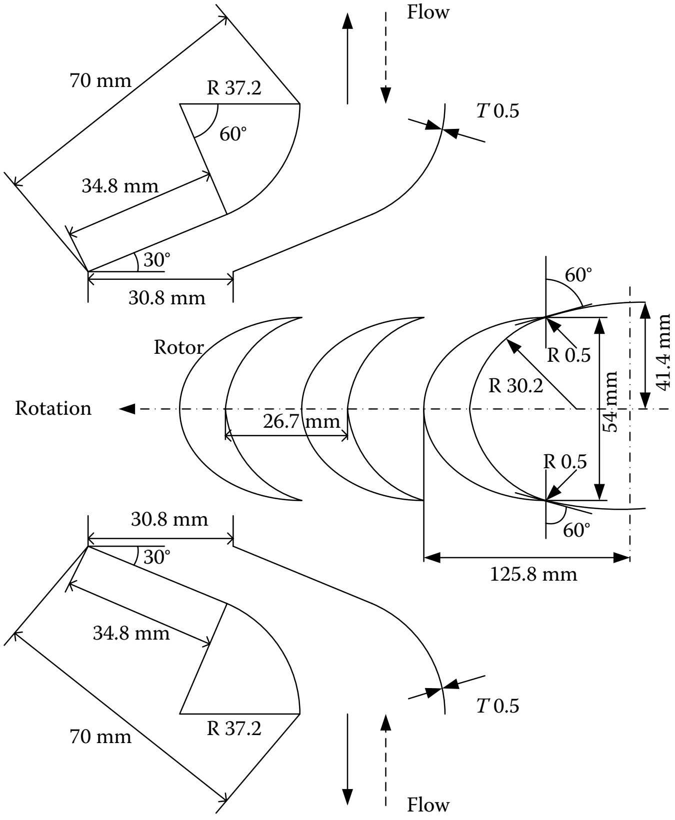

FIGURE 4.29 Impulse turbine with fixed guide vanes.

The turbines used for the experimental tests have the following specifications:

- BWGV: $\mathrm{AR} = 0.5, l_\mathrm{r} = 90$ mm, $\sigma_{\mathrm{rR}} = 0.45, \sigma_{\mathrm{gR}} = 1.25$.
- ISGV: $t_\mathrm{a}/S_\mathrm{r} = 0.4, l_\mathrm{r} = 54$ mm, $\gamma = 60°, \sigma_{\mathrm{rR}} = 2.02, \sigma_{\mathrm{gR}} = 2.27, \theta_1 = 17°, \theta_2 = 72.5°$, and $\lambda = -7.5°$.
- IFGV: $t_\mathrm{a}/S_\mathrm{r} = 0.4, l_\mathrm{r} = 54$ mm, $\gamma = 60°, \sigma_{\mathrm{rR}} = 2.02, \sigma_{\mathrm{gR}} = 2.27, \theta = 30°$, and $\lambda = -7.5°$,

where AR is the aspect ratio, l_r is the rotor chord length, σ is the solidity, t_a is the width of the flow path at r_R, S_R is the rotor blade space at r_R, γ is the blade inlet angle for impulse turbine rotor, θ is the setting angle of guide vane, and λ is the sweep angle.

Turbine characteristics were evaluated using the torque coefficient C_T, the input power coefficient C_A, and the flow coefficient ϕ [35]:

$$C_\mathrm{T} = \frac{T_0}{\left\{\rho_\mathrm{a} w^2 b l_\mathrm{r} z r_\mathrm{R}/2\right\}}, \tag{4.27}$$

$$C_\mathrm{A} = \frac{\Delta p Q}{\left\{\rho_\mathrm{a} w^2 b l_\mathrm{r} z v_\mathrm{a}/2\right\}}, \tag{4.28}$$

$$\phi = \frac{v_\mathrm{a}}{U_\mathrm{R}}, \tag{4.29}$$

where T_0 is the output torque, ρ_a is the air density, b is the rotor blade height, l_r is the rotor's chord length, w is the relative inflow velocity, z is the number of rotor blades, r_R is the mean radius, Δp is the total pressure drop between the settling chamber and atmosphere, v_a is the mean axial flow velocity, and U_R is the circumferential velocity at r_R.

According to the torque coefficient versus flow coefficient characteristics of these turbines, the rotor stall causes rapid decreases in C_T in Wells-type rotors such as BWGV. For impulse-type rotor turbines such as ISGV and IFGV, the increase in ϕ also increases the C_T value. Furthermore, the C_T value is larger at the larger ϕ region than other Wells turbines.

According to the C_A–ϕ characteristics of the turbines, the C_A value is the largest in WTGV; this means that the air chamber pressure is higher and may require more frequent bearing maintenance, due to the greater thrust force. ISGV and IFGV have smaller pressure increases in the air chamber when they are used as wave power generator devices [35].

The turbine efficiency can be obtained using C_T–ϕ and C_A–ϕ characteristics. The efficiency is defined as

$$\eta = \frac{C_T}{C_A \phi}. \tag{4.30}$$

However, it should be noted that efficiency is not the only important factor for optimal turbine selection in WEC. In addition, turbine characteristics vary with the efficiency of the air chamber, which is the ratio of the power of the OWC and the incident wave power [35]. Airflow generated by the OWC is irregular due to the irregular natural behavior of ocean waves. Thus, it is important to clarify the turbine characteristics under irregular flow conditions. The irregular test wave is based on The International Ship Structure Congress spectrum, which is specific for irregular wave behavior and is used typically in ocean applications [36].

A WEC system with an air turbine is presented in Figure 4.30, which shows the upcoming waves applying pressure to the air chamber, resulting in the rotation of the air turbine.

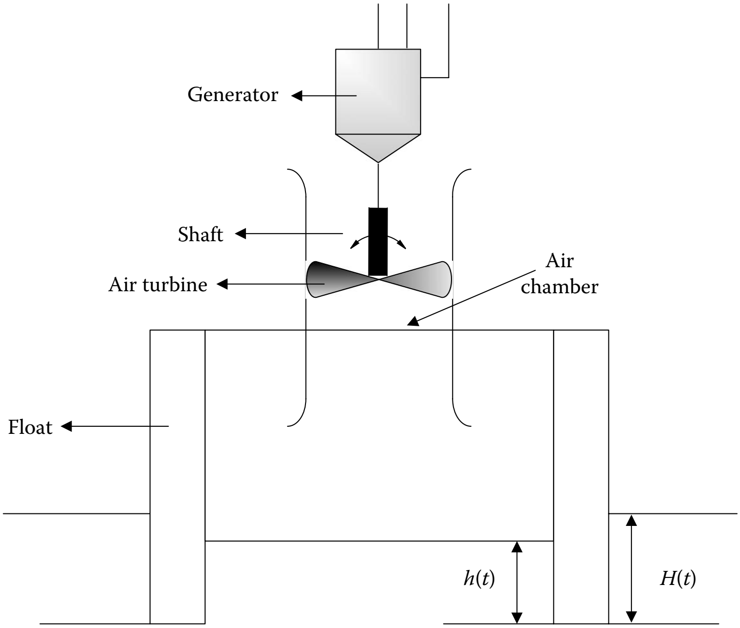

FIGURE 4.30 Schematic of the air turbine-type wave power generator system.

In this type of WEC system, the incident wave height and the wave height in the air chamber are interrelated as seen in the following equation [34]:

$$\frac{\mathrm{d}}{\mathrm{d}t}\left(\rho_{\mathrm{S}} h A_{\mathrm{C}} \frac{\mathrm{d}h}{\mathrm{d}t}\right) = \left\{\rho_{\mathrm{S}} g (H - h) - \Delta p\right\} A_{\mathrm{c}}, \tag{4.31}$$

where ρ_s is the seawater density, h is the wave height in the air chamber, H is the incident wave height, A_{c} is the cross-sectional area of the air chamber, and g is the gravity. The mean axial flow velocity is $v_{\mathrm{a}} = (1/m)(\mathrm{d}h/\mathrm{d}t)$ and Δp is a function of $(\mathrm{d}h/\mathrm{d}t)$ for a given rotational speed U_{R}. Extracting the relationship between Δp and $(\mathrm{d}h/\mathrm{d}t)$ from the C_{A}–ϕ curve, Equation 4.31) can be rewritten as [35]

$$\rho_{\mathrm{S}} A_{\mathrm{c}} \left\{\left(\frac{\mathrm{d}h}{\mathrm{d}t}\right)^2 + h \frac{\mathrm{d}^2 h}{\mathrm{d}t^2}\right\} = A_{\mathrm{c}} \left\{\rho_{\mathrm{S}} g (H - h) - \Delta p\right\}, \tag{4.32}$$

if it is assumed that $\Delta p / \rho_{\mathrm{S}} \equiv F(\mathrm{d}h/\mathrm{d}t)$.

Then,

$$h \frac{\mathrm{d}^2 h}{\mathrm{d}t^2} + \left(\frac{\mathrm{d}h}{\mathrm{d}t}\right)^2 + F\left(\frac{\mathrm{d}h}{\mathrm{d}t}\right) - g(H - h) = 0. \tag{4.33}$$

The Runge–Kutta–Gill method can be used to solve this equation to obtain the wave height in the air chamber. The power of the incident wave is W_{i} and the power of the OWC W_{o} can be defined as

$$\bar{W}_{\mathrm{i}} = \frac{\sum_{i=1}^{N} (1/32\pi) \rho_{\mathrm{S}} g^2 H_i^2 T_i^2}{\sum_{i=1}^{N} T_i}, \tag{4.34}$$

$$\bar{W}_{\mathrm{oi}} = \frac{\sum_{i=1}^{N} (1/32\pi) \rho_{\mathrm{S}} g^2 h_i^2 T_i^2}{\sum_{i=1}^{N} T_i}. \tag{4.35}$$

The efficiency of the air chamber is the ratio of the OWC power to the incident wave power as

$$\tilde{\eta}_{\mathrm{c}} = \frac{\bar{W}_{\mathrm{o}}}{W_{\mathrm{i}}}. \tag{4.36}$$

The axial velocity is directly proportional to the wave height if the flow is assumed to be incompressible. The axial flow velocity through the turbine can be expressed as

$$v_{\mathrm{a}}^* = \frac{\mathrm{d}\left(H/H_{1/3}\right)}{\mathrm{d}\left(t/\overline{T}\right)} = \frac{\mathrm{d}h^*}{\mathrm{d}\bar{t}^*}. \tag{4.37}$$

The motion of the turbine's rotating system under irregular flow can be described as

$$K^2 X_{\mathrm{I}} \frac{\mathrm{d}\bar{\omega}^*}{\mathrm{d}\bar{t}^*} + X_{\mathrm{L}} = C_{\mathrm{T}}(\phi) \frac{(K\bar{\omega}^*)^2 + v_{\mathrm{a}}^{*2}}{2} \sigma_{\mathrm{rR}} \frac{4(1 - v)}{1 + v}, \tag{4.38}$$

where

$$\phi = v_{\mathrm{a}}^{*}/(K\bar{\omega}^{*}), \tag{4.39}$$

$$K\bar{\omega}^{*} = \omega m r_{\mathrm{R}}\overline{T}/H_{1/3}, \tag{4.40}$$

$$v_{\mathrm{a}}^{*} = \frac{m\overline{T}v_{\mathrm{a}}}{H_{1/3}}. \tag{4.41}$$

Here, K is the period, X_{I} is the inertia moment, X_{L} is the loading torque, and σ_{rR} is the solidity at $r_{\mathrm{R}} = l.z/(2\pi r_{\mathrm{R}})$.

In Equation 4.38, the first and second terms on the left-hand side are the inertia and loading terms and the right-hand side is the torque produced by the turbine. Using Equation 4.38, the turbine behavior at the starting conditions can be calculated as a function of $K\bar{\omega}^{*}$ and v_{a}^{*} if the loading characteristics, torque coefficient, and geometrical specifications of the rotor are given. The operation characteristics after the start-up can be obtained assuming a constant rotor speed. The mean output and input coefficients C_{o} and C_{i} can be calculated, respectively, as

$$\bar{C}_{\mathrm{o}} = \frac{1}{t^{*}}\int_{0}^{t^{*}} C_{\mathrm{T}}(\phi)\frac{(K\bar{\omega}^{*})^{2} + v_{\mathrm{a}}^{*2}}{2} \times \sigma_{\mathrm{rR}}\frac{4(1-v)}{1+v}\bar{\omega}^{*}\,\mathrm{d}\bar{t}^{*}, \tag{4.42}$$

$$\bar{C}_{\mathrm{i}} = \frac{1}{t^{*}}\int_{0}^{t^{*}} C_{\mathrm{A}}(\phi)\frac{(K\bar{\omega}^{*})^{2} + v_{\mathrm{a}}^{*2}}{2K} \times \sigma_{\mathrm{rR}}\frac{4(1-v)}{1+v}v_{a}^{*}\,\mathrm{d}\bar{t}^{*}. \tag{4.43}$$

The mean turbine efficiency can be calculated as

$$\tilde{n}_{\mathrm{t}} = \frac{\bar{C}_{\mathrm{o}}}{C_{\mathrm{i}}}\bar{C}_{\mathrm{o}}/\bar{C}_{\mathrm{i}}. \tag{4.44}$$

Using the turbine and air chamber efficiencies, the overall conversion efficiency of the wave energy device is

$$\tilde{n} = \tilde{n}_{\mathrm{c}} \cdot \tilde{n}_{\mathrm{t}}. \tag{4.45}$$

The conversion efficiencies of different turbine types are shown in Figure 4.31. For impulse-type turbines, the efficiency is higher at the large $1/(K\bar{\omega}^{*})$ region in comparison to the Wells-type turbines. The rotor stall does not occur for the impulse-type turbines so the torque can be obtained in a comprehensive region of flow coefficient. The disadvantage of ISGV is the maintenance of pivots; however, it has the largest maximum efficiency, even larger than the IFGV in which the guide vanes are fixed [35]. Therefore, the running characteristics of the impulse turbine are better than the Wells turbine.

According to the starting characteristics of the turbines, very short time is required for the start of the impulse-type turbine. This means that impulse turbines can start more quickly than Wells turbines and can generate more power at the same start-up duration. In addition, the operational speed is lower than the Wells-type turbines. These are due to the higher torque coefficient of the impulse turbines than the torque coefficient of the Wells turbines. Moreover, flow coefficient is lower for the impulse turbines in no-load conditions. Thus, in terms of mechanical advantages and noise reduction, impulse turbines seem to be more suitable to design better applications for WEC systems.

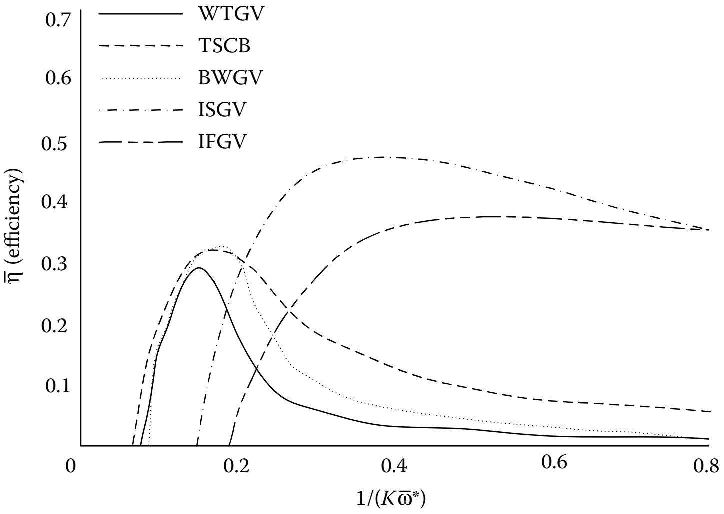

FIGURE 4.31 Comparison efficiency of wave energy converters with different turbines.

4.3.5 Wave Power Generators

There are several types of generators used to convert the wave energy into electrical energy. Generally, rotating machines such as synchronous generators or induction generators are used within the system employing a turbine to provide the mechanical driving for the generator shaft. These systems are very common for nearshore applications. Rarely rotating generators are found in buoy-shaped air turbine–driven generator systems. In other offshore applications including buoys, linear PM generators are common. Cam-shaped cylindrical ocean wave energy converters are exceptional, although they are offshore applications, rotating machines are employed with these devices.

4.3.5.1 A Wave-Activated Linear Generator Model

A wave-activated electric generator, which operates on the same principles as alternating current generators, is presented in [37]. The device forms a two degree of freedom mechanical system producing power by electromagnetic induction.

The proposed generator consists of an electric power generator enclosed in a buoy. The generator has a rectangular wire loop of N turns, directly supported by the buoy frame and a system with two PMs that are connected by helical springs to the buoy as shown in Figure 4.32. The wire loop moves between the magnets and magnets exhibit a two degree of freedom system excited by the wave-induced motion of the buoy. Since the system has no rotating parts, there will not be any fouling.

The electric power is generated as the reason of induced current in the conductor due to the moving conductor relative to a magnetic force.

The electric power generated in this type of linear generator can be expressed as

$$P = \frac{N^2B^2L^2V_r^2}{R}. \tag{4.46}$$

Here, V_r is the relative motion (distance) of the wire loop with respect to the magnet, B is the magnetic induction, R is the load resistance in the wire loop, and L is the wire length

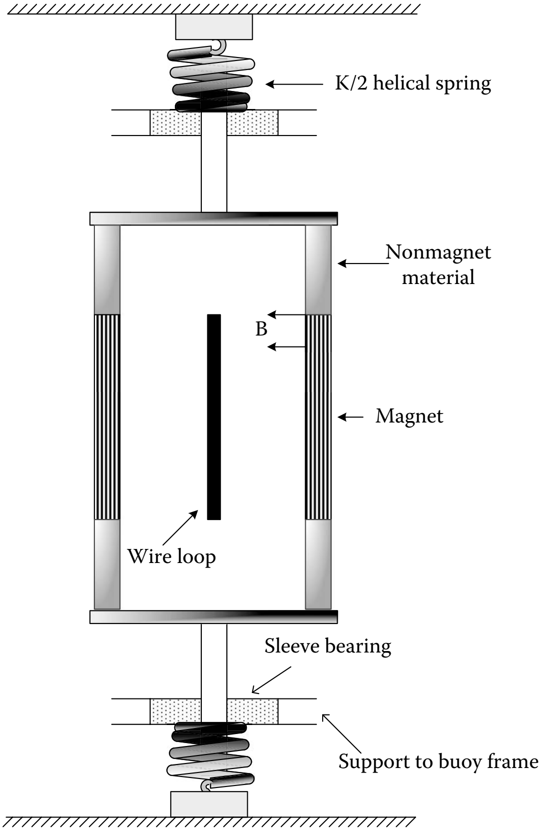

FIGURE 4.32 A linear wave activated generator system. (Modified from T. Omholt, *Oceans*, 10, 585–589, 1978.)

within the magnetic field in the plane perpendicular to the plane surface [37]. As a result of the current flow, a force will be applied on the loop opposing its motion, which can be written as in Equation 4.47. An equal but opposite force also applies on the magnets:

$$F = \frac{N^2B^2L^2V_r}{R}. \tag{4.47}$$

A simple schematic diagram of a buoy-generator system is shown in Figure 4.33 [37].

The sum of inertia, damping, and restoring forces for a buoy in this type of generator equals the excitation forces.

$$\text{Inertia forces} + \text{Damping forces} + \text{Restoring forces} = \text{Excitation forces}. \tag{4.48}$$

The following second-order equations describe the motion of the system by considering only vertical motion of a buoy-generator with infinitesimal waves:

$$(M + M_a)\ddot{Z} = \rho g K_p a_a \cos(\omega t) - \frac{B^2N^2L^2}{R}(\dot{Z} - \dot{X}) - K(Z - X) - b\dot{Z} - \rho g A Z, \tag{4.49}$$

$$M_m\ddot{X} = -\frac{B^2N^2L^2}{R}(\dot{X} - \dot{Z}) - K(X - Z), \tag{4.50}$$

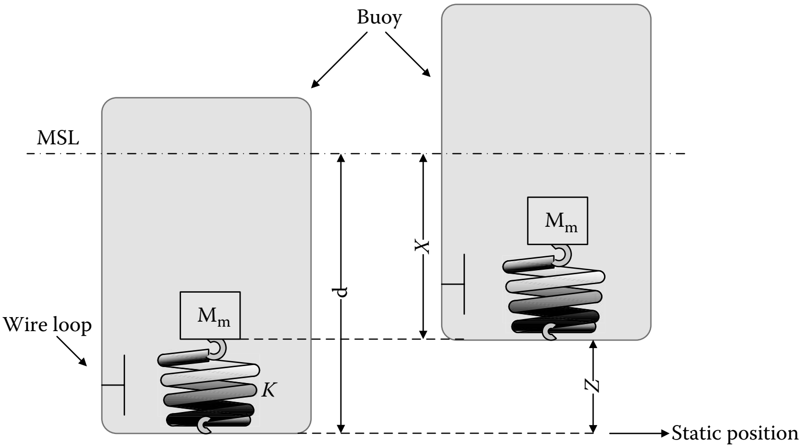

FIGURE 4.33 Schematic diagram of buoy generator system.

where $(m + m_\mathrm{a})\ddot{Z}$ represents the inertia forces, $b\dot{Z}$ stands for damping forces, and ρgAZ is the restoring force. The right-hand side of Equation 4.50 shows the sum of the excitation forces. Here, m is the mass of the buoy (mass of the spring-supported magnetic system is not included), m_a is the added mass, b is the damping coefficient, ρ is the water density, K_p is the pressure response factor ($K_\mathrm{p} = \mathrm{e}^{-kd}$), a is the wave amplitude, K is the total spring constant, ω is the wave frequency, and Z and X are the displacements shown in Figure 4.33, respectively. The derivations of these displacements give the corresponding velocity and acceleration. It is assumed that the buoy diameter is small in comparison to the wavelength [37].

Equation 4.50 is based on the assumption that the mass of the PMs is m_m and the system with PMs is excited by the induced force (F) and this force is transmitted through two helical springs [37].

From Equations 4.49 and 4.50, it can be seen that the $X = Z$ or $\dot{X} = \dot{Z}$ cases are not energy-generating motions. So, displacement of X and Z should not be synchronized or, in other words, the phase angle between two motions must be greater than 0° but less than 180°.

The system with PMs is excited by the force that is transmitted through two helical springs. The electric power generation can be expressed as

$$P = \frac{N^2B^2L^2}{R}(\dot{Z} - \dot{X})^2. \tag{4.51}$$

The average power over one wave period T can be obtained by integrating the power Equation given in Equation 4.51.

$$\overline{P} = \frac{1}{T}\int_0^T P\,\mathrm{d}t. \tag{4.52}$$

Recalling that the power that is carried by an ocean wave is expressed by $P_\mathrm{W} = \rho g^2a^2TD/8\pi$, the conversion rate of the system can be expressed as the ratio of the electric power generation over the total wave power, which is also the system efficiency:

$$\eta = \frac{\overline{P}}{P_{\text{wave}}} = 8\pi N^2B^2L^2 \int (\dot{Z} - \dot{X})^2 \frac{\mathrm{d}t}{\rho g^2 a^2 T^2 DR}. \tag{4.53}$$

From this efficiency equation, it can be observed that the system efficiency is a function of both relative speed of buoy and wired loop and the load resistance. In practice, both fluid viscosity and spring constant are small. They exert dumping force way less than that of the induction to the heavy buoy. However, for a lighter wired loop, these effects are almost not negligible. Taking these facts into account, motion equations can be simplified to the following state-space description:

$$\begin{bmatrix} \dot{x}_1 \\ \dot{x}_2 \\ \dot{x}_3 \\ \dot{x}_4 \end{bmatrix} = \begin{bmatrix} 0 & 1 & 0 & 0 \\ \dfrac{-\rho g A}{M+M_\mathrm{a}} & \dfrac{-(B^2N^2L^2/R)}{M+M_\mathrm{a}} & 0 & \dfrac{B^2N^2L^2/R}{M+M_\mathrm{a}} \\ 0 & 0 & 0 & 1 \\ \dfrac{K}{M_\mathrm{m}} & \dfrac{B^2N^2L^2/R}{M_\mathrm{m}} & \dfrac{-K}{M_\mathrm{m}} & \dfrac{-B^2N^2L^2/R}{M_\mathrm{m}} \end{bmatrix} \begin{bmatrix} x_1 \\ x_2 \\ x_3 \\ x_4 \end{bmatrix} + \begin{bmatrix} 0 \\ 1 \\ 0 \\ 0 \end{bmatrix} \frac{\rho g K_p a_\mathrm{a}}{M+M_\mathrm{a}} \cos(\omega t), \tag{4.54}$$

where the following substitution can be applied:

$$x_1 = z, \quad x_2 = \dot{z}, \quad x_3 = x, \quad x_4 = \dot{x}. \tag{4.55}$$

The general solutions to these linear equations in frequency domain are given by

$$x(\mathrm{j}\omega) = (\mathrm{j}\omega - A)^{-1}x(0) + (\mathrm{j}\omega - A)^{-1}BU(\mathrm{j}\omega), \tag{4.56}$$

where A is the state matrix, B is the input, and $x(0)$ represents the initial conditions. The first term describes the transient response of the system and it is not effective in the steady-state response. The second term describes system behavior under particular perturbation. In this case, it takes the form of sinusoidal wave as the assumption that ocean wave moves in this pattern. Consequently, the solution would consist of a pure sinusoidal wave at the same frequency as the input sine wave. The amplitude and phase determined by the system's frequency response at that frequency is given by [38]

$$G(t) = \left|G_\mathrm{s}(\mathrm{j}\omega)\right| \cos(\omega t + \angle\varphi_\mathrm{s}). \tag{4.57}$$

In order to model and simulate this system, the parameters of the PM linear generator and the other respective physical parameters can be selected as follows [38]: $M = 1344\,\mathrm{kg}$, $M_\mathrm{a} = 119.5\,\mathrm{kg}$, $L = 2.64\,\mathrm{m}$, $K = 1$, $B = 1.4\,\mathrm{T}$, $A = 4.86\,\mathrm{m}^2$, $N = 30$, and $D = 2.5$, $K_\mathrm{p} = 0.9$, $a_\mathrm{a} = 1.5\,\mathrm{m}$, and $\omega = 2\pi\,\mathrm{rad/s}$.

By implementation of these parameters, the state-transition matrix can be written as

$$A = \begin{bmatrix} 0 & 1 & 0 & 0 \\ -32.5 & -8.4/R & 0 & 8.4/R \\ 0 & 0 & 0 & 1 \\ 0.005 & 61.47/R & -0.005 & -61.47/R \end{bmatrix}. \tag{4.58}$$

According to the above analysis, the roots of the motion equations can be calculated as follows:

$$x_{\mathrm{i}} = \left|G_{\mathrm{i}}(j2\pi)\right| 9\cos(2\pi t + \angle G_{\mathrm{i}}(j2\pi)), \tag{4.59}$$

$$\begin{aligned}
G_1(2\pi j) &= \left.\frac{s^2R + 61.47s + 0.005R}{s^4R + 69.87s^3 + 32.505s^2R + 1997.7s + 0.1625R}\right|_{s=2\pi j},\\
G_2(2\pi j) &= \left.\frac{s(s^2R + 61.47s + 0.005R)}{s^4R + 69.87s^3 + 32.505s^2R + 1997.7s + 0.1625R}\right|_{s=2\pi j},\\
G_3(2\pi j) &= \left.\frac{61.47s + 0.005R}{s^4R + 69.87s^3 + 32.505s^2R + 1997.7s + 0.1625R}\right|_{s=2\pi j},\\
G_4(2\pi j) &= \left.\frac{s(61.47s + 0.005R)}{s^4R + 69.87s^3 + 32.505s^2R + 1997.7s + 0.1625R}\right|_{s=2\pi j},
\end{aligned} \tag{4.60}$$

These solutions can substituted within the system efficiency equation given in Equation 4.53; then it is observed that system efficiency is a complex function of resistance *R*. By controlling the value of the equivalent load resistance of *R*, the system efficiency can be maximized.

The effect of load resistance on the efficiency and power can be observed by using variable load resistance values and using them in Equations 4.61 through 4.63. In the simulation environment, a variable resistance is used to present the effect of the load resistance on extracted power and efficiency. A sinusoidal source is used to represent the ocean waveform. The resistance–average power and resistance–efficiency curves are shown in Figure 4.34 by sharing the same *x*-axis.

According to the results shown in Figure 4.34, the maximum power and maximum efficiency values can be achieved for a particular value of the load resistance. Ideally, the system should operate at this point. In order to achieve this goal, a current regulation should be provided for the generator's output. The rectifier and a large capacitor as shown

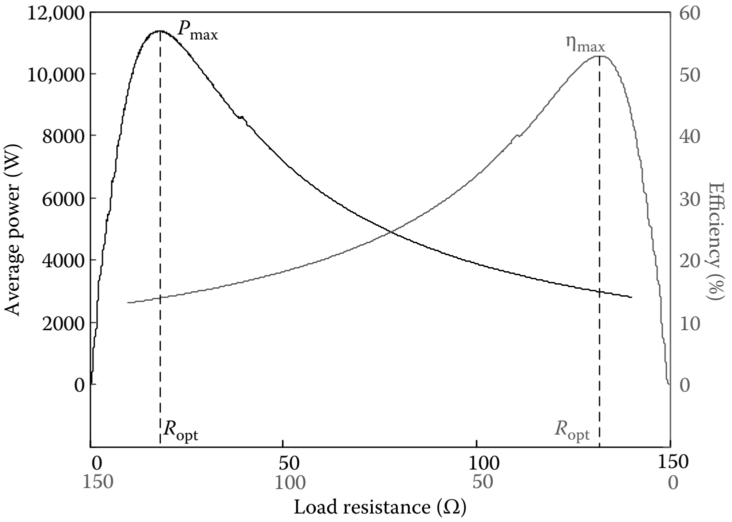

FIGURE 4.34 (**See color insert following page 80.**) Average power and efficiency variation versus load resistance.

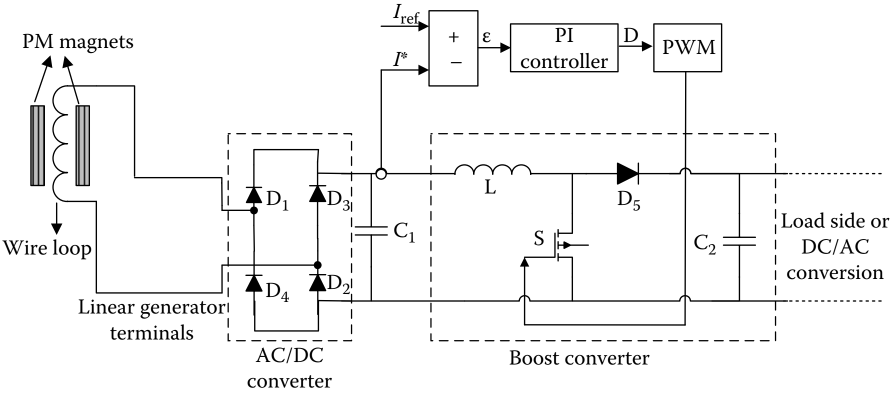

FIGURE 4.35 System-level configuration of the linear generator and power converters.

in Figure 4.35 provide a fixed DC voltage for the input of the boost converter. Assuming a lossless converter, the input current can be controlled to vary the Thevenin equivalent resistance of the system after the rectification.

The generator power and generator voltage are both in sinusoidal form as shown in Figures 4.36 and 4.37, respectively. The generator power has a biased sinusoidal waveform.

In order to regulate the generator's output power and voltage, the output of the linear generator terminals is first converted to the DC voltage and then filtered. Considering the large oscillations in the output, a large capacitor is required to achieve satisfactory voltage regulation performance. A boost DC–DC converter operating in the current control mode is employed, since the input voltage to boost the converter is the output voltage of the rectifier and that is fixed. Current control mode [38] helps optimum loading of the linear generator

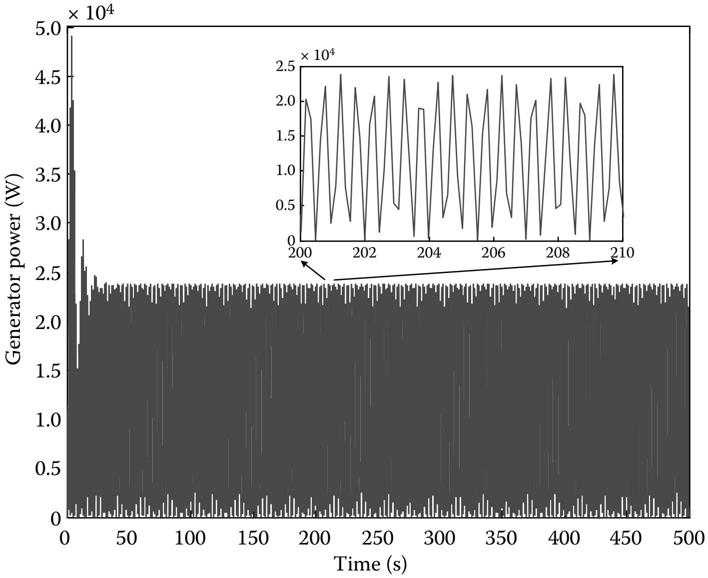

FIGURE 4.36 Generator power.

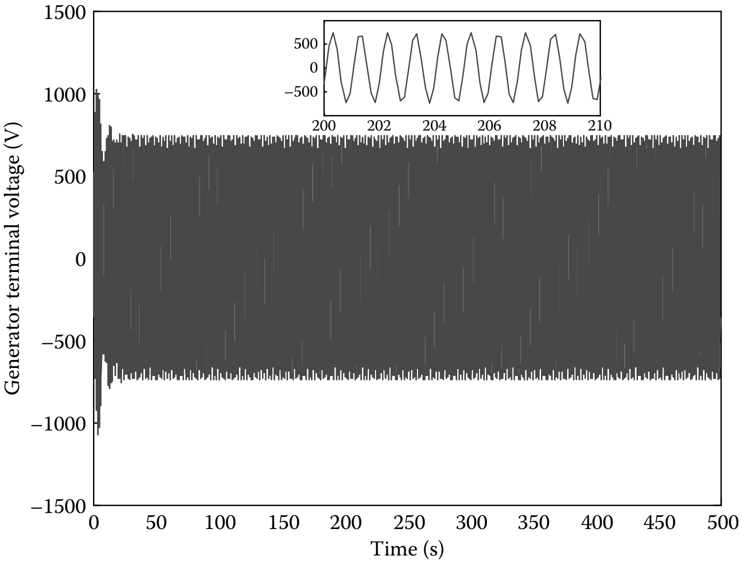

FIGURE 4.37 Generator voltage.

since the equivalent Thevenin's impedance is determined by the converter input voltage and current.

Therefore, regardless of what is connected at the output, by controlling the input current of the boost converter under fixed input voltage, one can control the equivalent resistance. The fixed input voltage for the converter is provided by the rectifier and capacitor connected at the generator terminals. Figure 4.38 shows the current tracking performance of the proposed system. As the current reaches the reference value in order to satisfy the optimal load resistance, the power also increases and reaches its maximum value.

4.3.5.2 Linear, Synchronous, Longitudinal-Flux PM Generators

Linear, synchronous, longitudinal-flux PM generators are one of the methods to convert the wave energy into electrical energy through direct drive. In [39,40], Muller presented some directly driven linear generators as wave energy converters. For WEC, the pistons of linear longitudinal-flux PM generators are generally driven by a buoy. Variable amplitude and variable frequency electromagnetic force is induced in the stator winding by the vertical motion of the piston [41]. The power fluctuation problems caused by the variable amplitude and frequency can be reduced by connecting several units as arrays [42].

A systematic approach for the design and modeling of an longitudinal-flux permanent-magnet machine (LFM) with diode rectifier where the piston is driven by a buoy is described by Wolfbrandt in [41].

The average power of an ocean wave over a wave period of T can be derived from the total energy of a wave as given in Equation 4.61. When a buoy is deployed as a wave rider, the power of that buoy can be approximated as

$$P_{\text{buoy}} = k\frac{TH^2}{2}\min\{d, \omega_{\text{a}}\}, \tag{4.61}$$

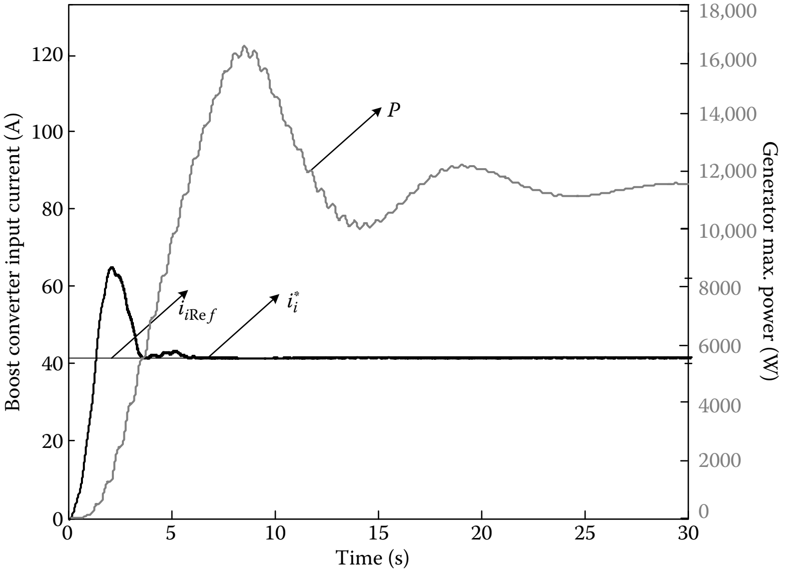

FIGURE 4.38 **(See color insert following page 80.)** Reference current tracking and power output for the linear PM generator.

where k is the absorption coefficient, d is the buoy diameter, and ω_a is the width of the buoy that can absorb maximum energy.

If the buoy is taken as a point absorber, the wave is assumed to be sinusoidal, and the displacement of the buoy is in one direction, then, for example, for $k = 0.8$, 50% power absorption is possible [43]. The width of the absorption is defined as [44–46]

$$\omega_a = \frac{L_{\text{wave}}}{2\pi}, \tag{4.62}$$

where the L_{wave} is the wavelength and is defined as

$$L_{\text{wave}} = \frac{gT^2}{2\pi}. \tag{4.63}$$

This equation is valid for deepwater, that is, the depth is greater than half the wavelength. In deepwater, the kinetic energy of a wave is equal to its potential energy. Wolfbrandt [41] considers a three-phase LFM rectified by a diode bridge rectifier with surface-mounted PMs that are directly driven. Figure 4.39 shows the x–y plane of the cross-sectional view of one pole of the generator.

In this method, the stator of the linear generator is supported by a buoy, which is fixed at the ocean bottom. Upcoming ocean waves drive the piston and this causes the up and down motion of the PM. This generates an electromagnetic field and a voltage is induced on the stator winding terminals.

The magnetic flux intensity in the stator is higher in the coils that are closer to the PM. The flux intensity gets weaker in the outer coil windings. The picture of the magnetic flux intensity created by such a PM system is shown in Figure 4.40.

There are other topologies, which also use the same principle of the linear generator system. For instance, the fixed stator windings can be mounted on a yoke that is fixed to the ocean bottom through a support unit. In this method, the PM is connected through a

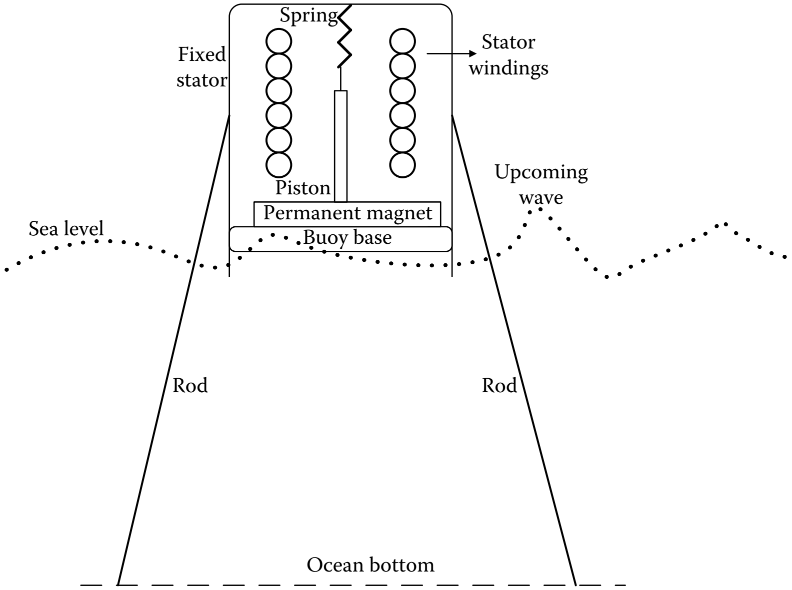

FIGURE 4.39 Schematic of an LFM used for WEC.

rope to a buoy, which is on the ocean level and moves up and down and can be dragged towards different directions. Once a wave results in the motion of the buoy, the buoy pulls the PM piston. The PM moves up and down within the fixed stator windings. This also generates an electromagnetic field generating the electricity. The schematic of this energy conversion device is illustrated in Figure 4.41.

Because of the relatively long wave periods (low frequency in piston motion) displacement current is negligible. Based on Maxwell's equations

$$\sigma\frac{\partial A_z}{\partial t} - \nabla\left(\frac{1}{\mu_0\mu_r}\nabla A_z\right) = -\sigma\nabla V. \tag{4.64}$$

Here, A_z is the z-component of the magnetic vector potential, μ_0 is the permeability of free space, μ_r is the relative permeability, σ is the conductivity, and ∇V is the applied potential.

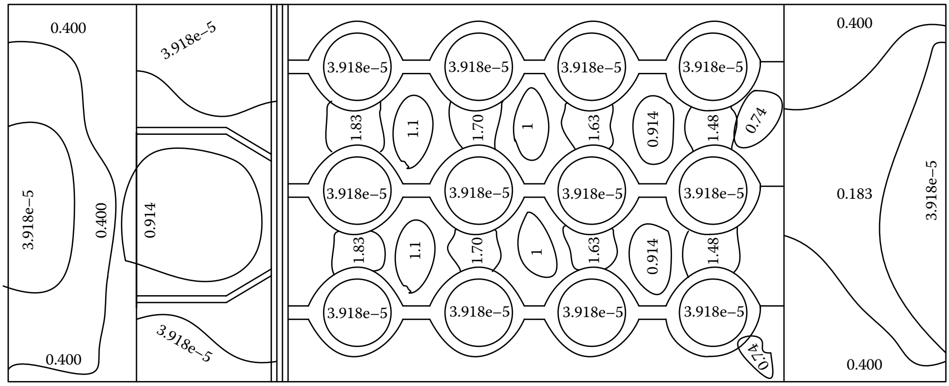

FIGURE 4.40 Approximate magnetic flux intensity (Wb/m^2) created by PMs.

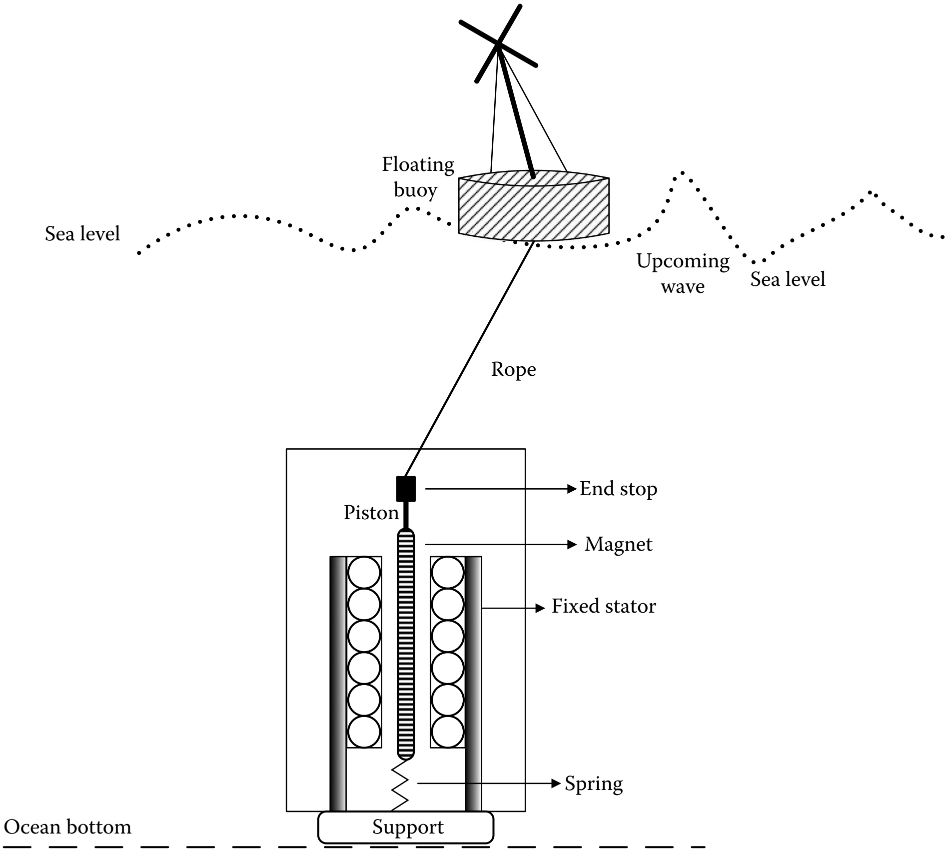

FIGURE 4.41 Another method of using LFMs for WEC.

Current sources can be used for PM modeling. The end effect of the stator windings can be modeled as impedances in the circuit. End effect is an issue that affects the power production performance of a linear generator. Stator winding equations can then be expressed as

$$I_a + I_b + I_c = 0, \tag{4.65}$$

$$U_a + R_s I_a + L_s^{\text{end}} \frac{\partial I_a}{\partial t} - U_b - R_s I_b - L_s^{\text{end}} \frac{\partial I_b}{\partial t} = V_{ab}, \tag{4.66}$$

$$U_c + R_s I_c + L_s^{\text{end}} \frac{\partial I_c}{\partial t} - U_b - R_s I_b - L_s^{\text{end}} \frac{\partial I_b}{\partial t} = V_{cb}, \tag{4.67}$$

where I_a, I_b, and I_c are the phase currents, U_a, U_b, and U_c are phase voltages, V_{ab} and V_{cb} are line voltages, R_s is the line resistance, and L_s^{end} is the coil end inductance.

The output phase voltages of the linear generator can be rectified using a three-phase diode rectifier and can be connected to a load. A full bridge six-pulse diode rectifier connected to the load is shown in Figure 4.42. In Figure 4.42, the load components include resistive (R), inductive (L), and back-EMF (E).

The losses in the linear generator can be mainly categorized as copper losses and iron losses. The power flow illustrating these losses is shown in Figure 4.43, where P_{gen} is the ideal generated power and P_{out} is the actual power output of the generator.

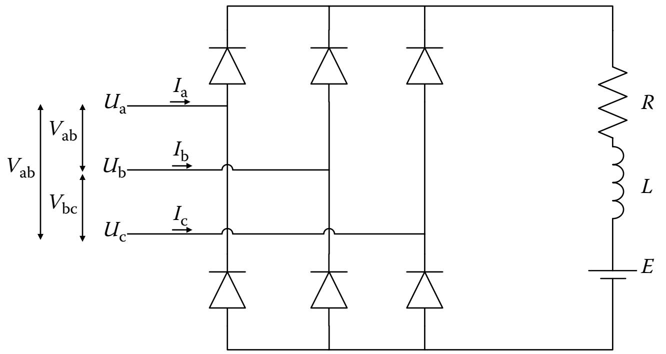

FIGURE 4.42 Three-phase diode rectifier schematic where a, b, and c are the linear generator phases.

The stranded stator winding losses are divided into ohmic losses $\left(P_{\mathrm{Cu}}^{\mathrm{ohmic}}\right)$ and eddy-current losses $(P_{\mathrm{Cu}}^{\mathrm{joule}})$. These loss equations can be expressed as [41]

$$P_{\mathrm{Cu}}^{\mathrm{ohmic}} = 3R_{\mathrm{s}}I_{\mathrm{s}}^{2}, \tag{4.68}$$

$$P_{\mathrm{Cu}}^{\mathrm{joule}} = \frac{\sigma\omega^2 d^2}{32}\int\limits_{S} B^2\,\mathrm{d}S, \tag{4.69}$$

where ω is the angular frequency, d is the strand diameter, S is the cross-sectional conductor area, and B is the magnetic field density.

A single-value magnetization curve is used to model the nonlinearity of the laminated iron core. The iron losses can be divided into hysteric losses $\left(P_{\mathrm{Fe}}^{\mathrm{hyst}}\right)$, joule losses $\left(P_{\mathrm{Fe}}^{\mathrm{joule}}\right)$, and excess losses $\left(P_{\mathrm{Fe}}^{\mathrm{excess}}\right)$ [47]. These loss equations are given by

$$P_{\mathrm{Fe}}^{\mathrm{hyst}} = k_{\mathrm{f}}k_{\mathrm{hyst}}f\int\limits_{V} B_{\max}^{\mathrm{q}}\,\mathrm{d}V, \tag{4.70}$$

$$P_{\mathrm{Fe}}^{\mathrm{joule}} = k_{\mathrm{f}}\sigma\frac{\mathrm{d}^2}{12}\int\limits_{V}\frac{1}{T}\int\limits_{0}^{T}\left(\frac{\partial B}{\partial t}\right)^2\mathrm{d}t\,\mathrm{d}V, \tag{4.71}$$

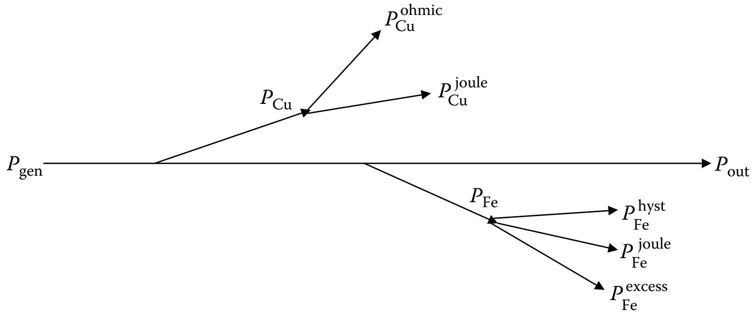

FIGURE 4.43 Power flow and losses of the linear generator.

$$P_{\mathrm{Fe}}^{\mathrm{excess}} = k_{\mathrm{f}} k_{\mathrm{excess}} \int_V \frac{1}{T} \int_0^T \left(\frac{\partial B}{\partial t} \right)^{3/2} \mathrm{d}t\,\mathrm{d}V, \tag{4.72}$$

where B_{max} is the maximum magnitude of the magnetic field density, f is the frequency, d is the sheet thickness, k_{f} is the stacking factor, T is the time period, and V is the stator core volume. The coefficients k_{hyst} (Ws/T^q/m^3), k_{excess} (W/(T/s)$^{3/2}$/m^3), and the exponent q are determined by fitting of a given loss curve.

Piston losses that are in the back iron, PM, and the aluminum wedge can be calculated using the Poynting vector. Thus, the joule losses $\left(P_{\mathrm{piston}}^{\mathrm{joule}}\right)$ and the hysteresis losses $\left(P_{\mathrm{piston}}^{\mathrm{hyst}}\right)$ can be written as

$$P_{\mathrm{piston}}^{\mathrm{joule}} = \int_V \frac{1}{T} \int_0^T \sigma \left(\frac{\mathrm{d}A_{\mathrm{z}}}{\mathrm{d}t} \right)^2 \mathrm{d}t\,\mathrm{d}V, \tag{4.73}$$

$$P_{\mathrm{piston}}^{\mathrm{hyst}} = \int_V \frac{1}{T} \int_0^T \left(H_x \frac{\mathrm{d}B_x}{\mathrm{d}t} + H_y \frac{\mathrm{d}B_y}{\mathrm{d}t} \right) \mathrm{d}t\,\mathrm{d}V, \tag{4.74}$$

where T is the time period and V is the piston volume.

The electromagnetic force F_{em} induced by the generator can be expressed as

$$F_{\mathrm{em}} = \frac{\mathrm{d}W_{\mathrm{c}}}{\mathrm{d}x}, \tag{4.75}$$

where W_{c} is the coenergy in the volume of the air gap and x is the piston position. Stator current ripple causes the electromagnetic force ripple. These ripples caused by the phase-belt magnetomotive space harmonics can be eliminated by fractional slot pitch winding.

LFM with different voltage loads results in different current densities. The current density should be limited to i_{max} due to the physical constraints of the linear generator. Because of this limitation, the output generator power will be limited by

$$P_{\mathrm{out}}(i) < P_{\mathrm{buoy}} - P_{\mathrm{losses}}(i), \tag{4.76}$$

$$i < i_{\mathrm{max}}. \tag{4.77}$$

P_{buoy} is defined in Equation 4.61, and P_{losses} is defined as the sum of losses given in Equations 4.68 through 4.74.

Figure 4.44 illustrates these powers with respect to the maximum current. The solid line is the input power (buoy power), the dotted line is the output power, and the dashed-dotted line is the sum of the output power and losses, which represent the total power.

4.3.5.3 A Three-Phase Synchronous Generator for Ocean Wave Applications

The synchronous generators are generally used in power plants with constant speeds. For wave energy applications, the design and model of a wound rotor brushless synchronous generator is presented in [48].

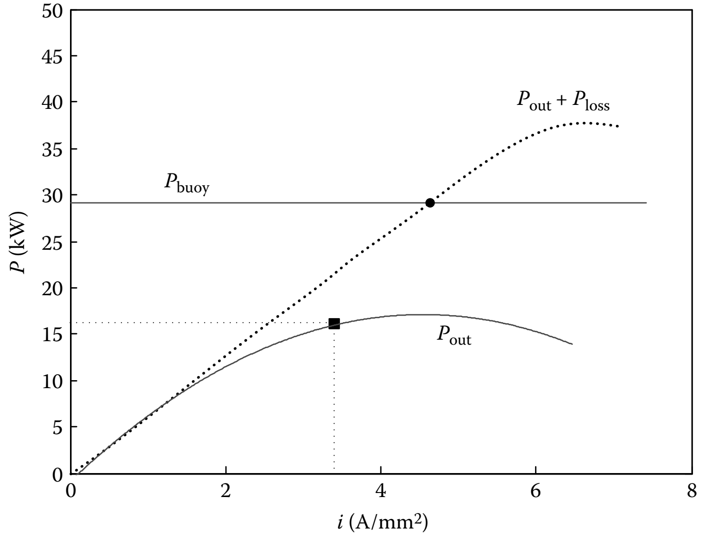

FIGURE 4.44 Buoy power and output power versus current density.

In a synchronous machine, the relation of rotor speed and output power frequency is

$$f = \frac{pn}{120}, \tag{4.78}$$

where f is the output frequency, p is the number of salient poles, and n is the rotation speed of the rotor shaft in rpm. Therefore, for a two salient pole machine, the synchronous speed would be 3600 rpm [48], since the output frequency of the system should be 60 Hz for grid connection. The armature excitation generates AC and this current is converted to DC so that armature exciter acts as a DC supply for field winding. The armature exciter has three phase windings in order to get the improved efficiency of three-phase rectification in comparison to single-phase rectification.

In this generator, the salient pole face is taped so that the air gap width reaches its minimum value at the pole center. The magnetic flux is maximum at the minimum air gap. Magnetic flux decreases to zero at the midpoint between the poles and reaches to its negative maximum in the center of the adjacent pole. The flux density in the air gap is sinusoidal as

$$B = B_{\text{max}} \cos \beta y \ (T), \tag{4.79}$$

$$\beta y = \frac{p}{2} 2\pi, \tag{4.80}$$

$$y = \pi D, \tag{4.81}$$

where y is the fixed coordinate of the vertical axis with respect to the rotor, β is the rotor flux angle, and D is the air gap diameter.

Therefore, flux density equation can be rewritten as

$$B = B_{\text{max}} \cos \frac{py}{D}. \tag{4.82}$$

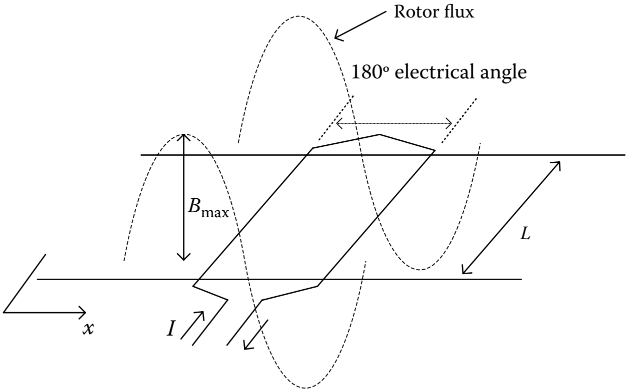

FIGURE 4.45 The traveling flux wave of stator winding.

Figure 4.45 shows the induced EMF in the stator winding to achieve a sinusoidal flux distribution along its periphery. Therefore, the flux in terms of the coordinate x is fixed with respect to the stator [48].

Coordinates and rotor position for stator winding are shown in Figure 4.46.

From Figure 4.46,

$$x = y + st \text{ (m)}, \tag{4.83}$$

where the tangential speed of the rotor, s, is given by

$$s = \frac{n\pi D}{60} \text{ (m/s)}. \tag{4.84}$$

Thus,

$$B = B_{\max} \cos\left(\frac{px}{D} - \frac{pn\pi}{60}t\right) \text{ (T)} \tag{4.85}$$

or

$$B = B_{\max} \cos(\beta x - \omega t) \ (T), \tag{4.86}$$

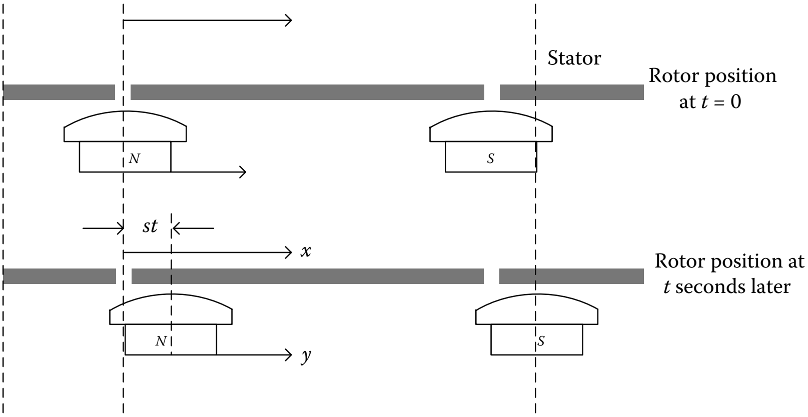

FIGURE 4.46 Coordinates and rotor position for stator winding.

where

$$\omega = \frac{pn\pi}{60} = 2\pi f\,(\text{rad/s}). \tag{4.87}$$

This is the mathematical expression for a traveling wave in the induced EMF stator winding.

The differential flux penetrating the differential space window of the width dx is given by

$$\mathrm{d}\phi = BL\,\mathrm{d}x\,(\text{Wb}), \tag{4.88}$$

where L is the axial rotor length.

Total flux passing through the coil is given by

$$\phi = \frac{2B_{\max}LD\sin\,\omega t}{p}\,(\text{Wb}). \tag{4.89}$$

Total EMF induced in the equidistant slots can be derived from Equation 4.88 as

$$E = \omega LDNB\cos\,\omega t\,(\text{V}), \tag{4.90}$$

where N is the number of turns in the stator winding. Generated EMF's effective value can be written as

$$E = \frac{\pi}{60\sqrt{2}}pnNLDB\,(\text{V}). \tag{4.91}$$

A practical design utilizing the total stator surface by placing the stator winding in many slots distributed around the periphery is shown in Figure 4.47.

The slots are placed by α electrical degree phase angels and totally there are q slots per pole. The total EMF is obtained by connecting the coils in series. The induced EMF depends on the slot α degrees. Thus, the total E is obtained by the summation of complex phasors E_1, E_2, and so on.

$$E = E_1 + E_2 + \cdots + E_q\ (\text{V}). \tag{4.92}$$

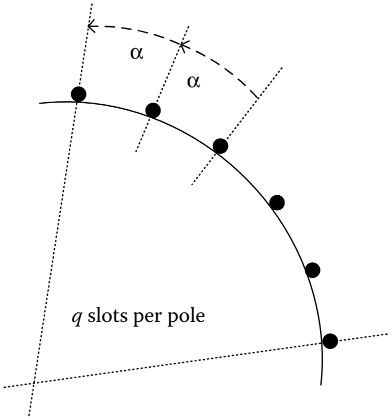

FIGURE 4.47 Total stator surface and q slots around the periphery.

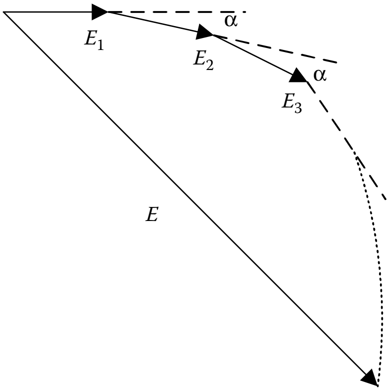

FIGURE 4.48 Induced total EMF phasor.

The distribution effect and the EMF phasor E is shown in Figure 4.48.

Thus, distribution effect can be derived using all induced EMFs for phasor E. Phasor E can be calculated from

$$E = E_1 \frac{1 - e^{-jq\alpha}}{1 - e^{-j\alpha}}. \tag{4.93}$$

The effective value of the complex phasor E is

$$\begin{aligned} |E| &= |E_1| \left| \frac{1 - e^{-jq\alpha}}{1 - e^{-j\alpha}} \right| \\ &= |E_1| \frac{\sqrt{(1 - \cos q\alpha)^2 + \sin^2 q\alpha}}{\sqrt{(1 - \cos \alpha)^2 + \sin^2 \alpha}} \\ &= |E_1| \frac{\sin(q\alpha/2)}{\sin(\alpha/2)}. \end{aligned} \tag{4.94}$$

Single-phase stator core and winding arrangement is shown in Figure 4.49.

In Figure 4.49, each different couple of poles is associated with the winding inducing EMF components of E_q. The total EMF, E, is the vector summation of all sets of EMF E_q. Figure 4.49 shows that there are two sets of coils and each set of coils contains six coils per pole per phase.

Output power is shared by three phases. When the load is connected to the generator terminals, the voltage drop is given by

$$V = E - IZ, \tag{4.95}$$

where V is the terminal voltage, E is the induced EMF, I is the stator current, and Z is the impedance.

The armature excitation and field excitation are necessary for brushless synchronous generator. To produce more output power and to reduce output frequency more poles can be used for the exciter. Magnetic flux may lose its stability if the frequency ripple is higher.

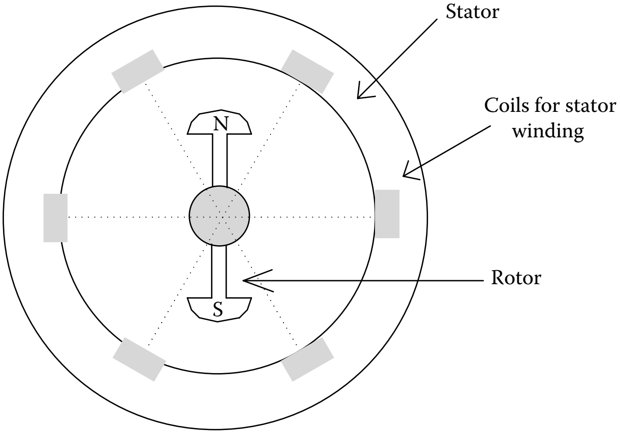

FIGURE 4.49 Stator core design and stator winding arrangement per phase.

In this generator design, six poles for armature exciter and field exciter coil were used for less frequency ripple. The excitation circuit is shown in Figure 4.50.

The resistance and inductance of the generator winding affect the power losses, I^2R, which in turn affects the generator efficiency. Therefore, the number of turns (N) in the stator winding and thickness of the copper wire affect the equivalent resistance and inductance.

The resistance and copper losses can be estimated as

$$R = \frac{0.022}{D_{\mathrm{w}}^2}\ (\Omega/\mathrm{m}), \tag{4.96}$$

$$P_{\mathrm{w}} = 0.02 l_{\mathrm{w}} \left(\frac{I}{D_{\mathrm{w}}}\right)^2, \tag{4.97}$$

where D_{w} is the diameter of the wire, I is the rms current in the winding, and l_{w} is the winding length. l_{w} can be calculated by

$$l_{\mathrm{w}} = N\pi D_{\mathrm{av}}, \tag{4.98}$$

where D_{av} is the average diameter of the winding.

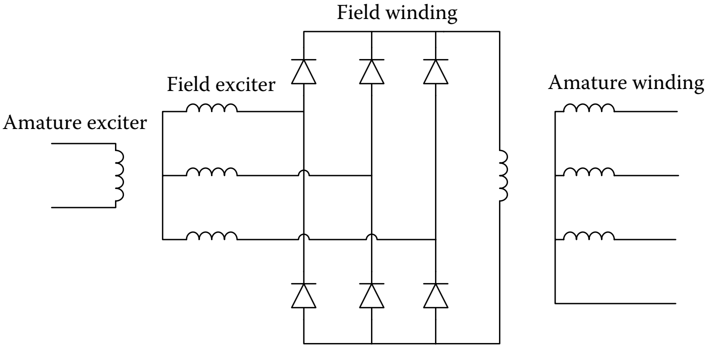

FIGURE 4.50 The schematic of brushless generator wound rotor with armature and field exciter systems.

Another effect that should be considered in the machine design is skin effect. Skin effect is the tendency of the current flow to be closer to the outer surfaces of the conductor. At low frequencies, the current distribution can be assumed as uniform. The copper wire thickness should be determined based on the output frequency.

Eddy current losses and hysteresis losses are the other criteria, which should be considered in machine-laminated core design. Iron-laminated core with higher permeability is preferable to increase the flux density and reduce the size of the generator.

Figure 4.51 shows the flux density, B, versus field strength, H for soft metal. Total output power is increased because high-speed generators (3600 rpm) have less losses in comparison to low-speed generators.

Thinner laminated and soft magnetic materials can be used to develop more efficient machine core design. This can also reduce the mechanical stress and heat losses in the laminated core.

4.3.5.4 Radial Flux PM Synchronous Generator for WEC

A radial magnetic flux electrical generator with a horizontal-axis water current turbine is presented in this subsection. The sketch of a ducted turbine surrounded by an electric generator, presented in Figure 4.52a and 4.52b [49].

Some older technologies are based on the coupling of an axial flow turbine with an electric generator similar to wind turbines. A gearbox is required to shift up the typical rotor speed (10–20 rpm) to the speed of a conventional generator (above 500–1000 rpm). However, direct drive is an attractive solution to eliminate the complexity, failure rate, efficiency, and maintenance cost [49].

In the directly driven turbine topology, the active parts of the machine are surrounded by the periphery of the blades instead of placing them on the axis of the turbine as in the classical methods. This idea is studied in [50–52], which have presented successful results for marine propulsion. Some of those rim-driven propellers are used for autonomous underwater vehicles or vessel propulsion. A similar machine has been tested with a 50-W rating turbine in [49].

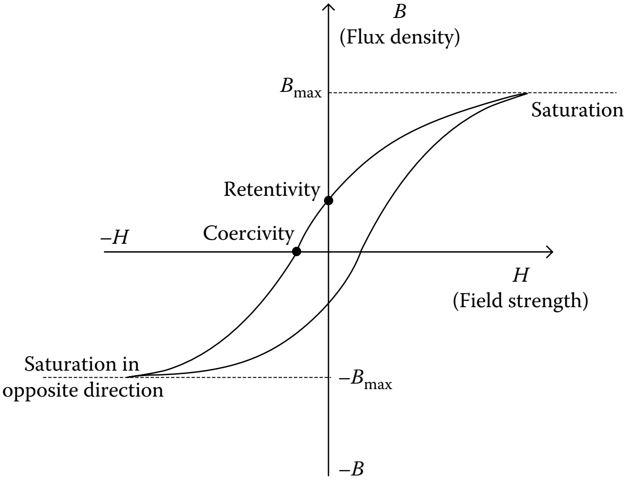

FIGURE 4.51 Flux density B versus field strength H.

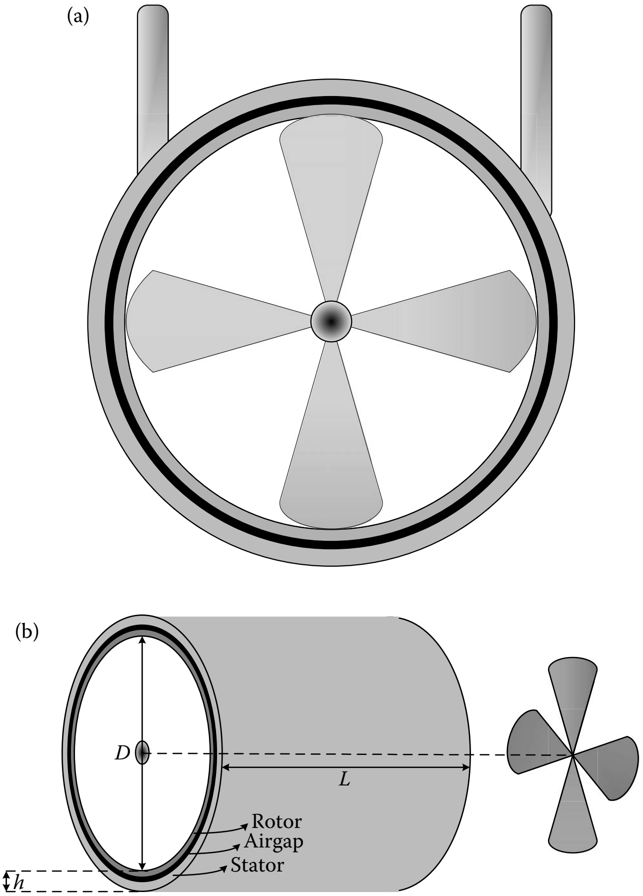

FIGURE 4.52 Radial magnetic flux electric generator that is placed on the periphery of the horizontal axis turbine blades, (a) frontal view and (b) lateral view.

Elimination of the gearbox is one of the benefits of the structure presented in [49]. The gearbox can consist of up to three stages, which brings complexity and is a heavy and expensive component. Directly driven application to a low-speed generator with the blades around results in high rated torque when compared to classical direct drive machines that are usually heavier and less efficient [53]. Also by keeping the generator in a protective duct, the hydrodynamic efficiency of the blades may increase and vibration and cavitation performance may increase [52]. Placing the active part of the generator around the blades results in increased gap diameter of the machine and the machine can have a higher torque. The torque of a machine coupled to a turbine generating the power of P with a rotor speed of Ω would be

$$T = \frac{P}{\omega}. \tag{4.99}$$

The rotor and the stator are separated with a gap in which the electromagnetic interaction occurs. The tangential force density σ_t in the gap depends on the machine technology and cooling system. Using the tangential force density, the electromagnetic torque can be expressed as

$$T = \frac{\sigma_t SD}{2}, \tag{4.100}$$

where D is the gap diameter and S is the gap surface. For a given power and speed performance, increasing the gap diameter D will decrease the required surface S and the size of the machine as well. If the thickness h is independent of a chosen diameter D (this assumption is realistic for a given rotation speed), the required active volume (the surface times thickness, $S \cdot h$) shall decrease by increasing D [49].

Since the generator is a synchronous PM radial flux machine, it has less copper losses within the rotor in comparison to wound rotors. In induction machines a very thin air gap is required in order to limit the magnetizing currents and leakages, so the air gap in these dimensions is not comparable for the propeller diameter several meters long.

The synchronous machine designed in [49] is connected to a pulse width modulation (PWM) voltage converter to control the current wave of the stator and the rotation speed. It can be connected to the electrical grid or load bus through a power electronic interface.

The challenge on design is to achieve the minimum gap. This is due to the fact that the radial induction of the magnets that reaches the stator surface is inversely proportional to the magnetic gap thickness. The other challenge is the immersion of the gap. Letting the water flow through the gap minimizes the sealing problems in comparison to the other hub systems requiring a rotating seal [50–52]. This improves the thermal performance of the machine. On the other hand, active elements need to be covered with corrosion-resistant paint or fiber glass plus epoxy coating, since active elements are corrosive.

The electromagnetic model determines the main physical characteristics of the machine such as size, power rating, and diameters. The most effective parameter is the electromagnetic torque T, which is calculated as given in Equation 4.101 neglecting the mechanical losses. T can also be calculated as

$$T = k_{\mathrm{bl}}\sqrt{2}A_{\mathrm{L}}B_1\frac{\pi D^2 L}{4}\cos\psi, \tag{4.101}$$

assuming a purely sinusoidal current in the stator. In Equation 4.101, A_{L} (A/m) is the rms value of the stator current, $B_1(T)$ is the peak value of the stator surface flux density, k_{b1} is the winding factor, and ψ is the angle between the vectors of induced electromagnetic force and stator current. Equation 4.101 is useful to determine the size of the generator active part if $A_{\mathrm{L}}, B_1, k_{b1}$, and ψ are fixed at classical values for low-speed, high-torque machines [49]. If the angle is set to zero, the size can be minimized. This might increase the size and cost of the converter [54] but for the subwater application, it will be advantageous to reduce the machine size.

The flux density B is affected by the magnet type, gap thickness, and dimensional as well as financial constraints. The magnets have uniform radial magnetization and are surface mounted on the rotor as shown in Figure 4.53.

A simple analytical expression for B_1 as a function of dimensions and magnet characteristics is not easy because of the specific features of the machine. Irregular proportion of leakage flux occurs from one magnet to the next in the case of a large air gap in comparison to short pole pitch. Assuming a purely radial flux density may also give inaccurate results. Using a 2D model developed by Zhu et al. [55] solves the governing equations in the y-axis by separating the polar variables and considering the leakages. It predicts the open-circuit field distribution in the air gap of the surface-mounted PM machine without

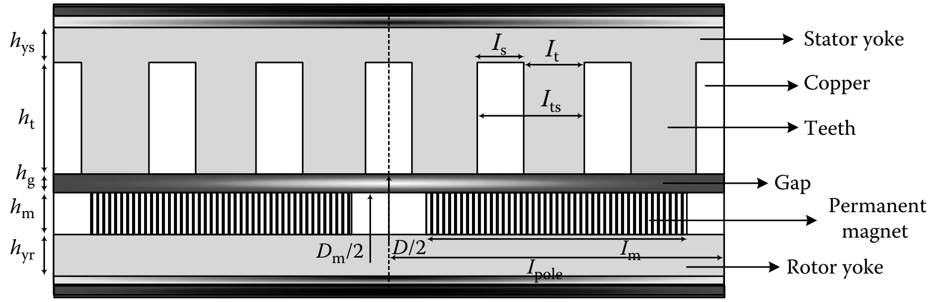

FIGURE 4.53 (**See color insert following page 80.**) Cross-sectional view of two poles of the generator.

slots. An expression of B_1 can be derived as follows and simplified assuming a large rotor diameter in comparison to the thickness and a high number of poles:

$$B_1 = \frac{2B_r k_\beta R_{sm}^{p}(1 - x^2 + 2x/p)}{(\mu_r + 1)(R_{sm}^{2p} - x^2) - (\mu_r - 1)(1 - x^2 R_{sm}^{2p})}, \tag{4.102}$$

$$x = \left(1 - \frac{h_m}{0.5D_R - h_g}\right)^p, \tag{4.103}$$

$$k_\beta = \frac{4}{\pi}\sin\frac{\beta\pi}{2}, \tag{4.104}$$

where B_r is the flux density remnant of the magnets, β is the ratio of magnet width to pole width (l_m/l_{pole}), R_{sm} is the ratio of air gap diameter to magnet outer diameter (D/D_m), p is the number of pair poles, μ_r is the magnets relative recoil permeability, h_m and h_g are the magnet and air gap heights, respectively. The slotless machine equivalent can be obtained by Carter factor [55]. Carter factor is a parameter to include the slotting effect on the air gap flux. If B_1, p, and R_{sm} are known h_m can be solved to calculate the required magnet height.

The slot height, h_s, can be calculated as follows for a given loading current A_L [54]:

$$h_s = A_L(Jk_f k_s)^{-1}. \tag{4.105}$$

Here, J (A/m) is the density of the rms current, k_f is the slot fill factor, and k_s is the ratio of l_s to l_{t+s} (shown in Figure 4.53). Current density, J, depends on the thermal factors, which are improved by the water surrounding the generator parts in this application. Hence, the overall thickness of the machine can be reduced.

The rotor and stator yoke heights should be chosen to avoid the iron saturation since these heights affect the air gap size. Electric steels generally have a saturation flux density (B_{sat}) around 1.7 T. In order to limit the iron losses, B_{sat} is limited to 1.7 T in [49]. The flux densities produced by magnets and coils can be estimated by classical methods described in [53]. However, due to the large air gap to short pole pitch ratios, 2D finite difference simulations show that these equations miscalculate the dimensions. The mean value of the flux density into yokes is increased by the large proportion of leakage flux between magnets and coils. The yoke heights h_{yr} and h_{ys} can be readjusted by an iterative process [49]. However, the yokes remain thin and mechanical constraints for the integrity of the structure are the main factor for rating. The ratio of tooth width to slot pitch (l_t/l_{t+s}) can also be estimated such that the teeth do not saturate and their shape is also kept realistic. The air gap diameter, D, and the active length, L, can be obtained once the heights of the magnet and rotor yoke are calculated fixing the rotor diameter, D_R, and the gap, h_g.

In order to limit the iron losses the electrical frequency should be limited to a maximum of f_{max}. Thus, the maximum number of poles can be determined. The magnets have to be protected from demagnetization, particularly if low B_1 values are specified. It shows that the magnetic field cannot exceed its coercive field in any point of the magnet [49]. Therefore, the minimum number of poles can be determined.

The electrical part of the analytical model includes the desired voltage and current levels of the generator. Then design parameters such as machine dimensions and coil characteristics are determined. The back EMF in each phase can be derived using $(\mathrm{d}\phi/\mathrm{d}t)$, where ϕ is the magnetic flux of one phase winding and the current can be calculated from the EM torque.

$$T = EI\Omega^{-1}\cos\psi. \tag{4.106}$$

The phase resistance, R, is also calculated by considering the endwindings geometry, taking each endwinding as a half circle with a diameter equal to the pole pitch [56]. The resistance is calculated using the copper conductivity with respect to the nominal temperature [49].

Then the output voltage and the power factor can be calculated as shown in Figure 4.54. The current and voltage levels affect the electronic drive circuit and the electrical network. Moreover, the machine time constant should be determined, which is a function of the converter switching frequency.

The losses and efficiency part of the analytical model can be roughly estimated, using the copper and iron losses of the machine as well as the copper losses. The copper losses are proportional to the coil resistance as

$$P_{Cu} = 3RI^2. \tag{4.107}$$

This equation includes the losses in the active part and endwindings. For a small axial length and large diameter, the endwinding losses may increase and dominantly affect the copper losses [49]. Iron losses can be estimated using loss per unit mass for the stator magnetic circuit as

$$P_{Fe} = P_{Fe_0}\left(f\cdot f_0^{-1}\right)^b\left(B_{max}B_{max_0}^{-1}\right)^c, \tag{4.108}$$

where f is the frequency of the field iron, P_{Fe_0} is the iron losses per mass unit at the given frequency of f_0, B_{max_0} is the flux density, and b and c are 1.5 and 2.2, respectively, for a typical high-quality Fe–Si-laminated steel. The mechanical losses are neglected in this model. Mechanical losses are affected by the choice of the bearing technology to compensate for the axial drag of the turbine and to keep the gap between the stator and rotor fixed.

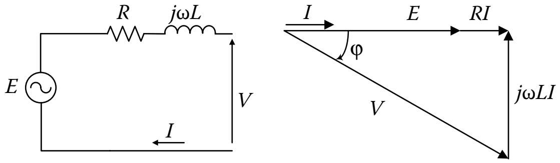

FIGURE 4.54 Electrical phasor diagram for $\psi = 0$.

The thermal model estimates the temperature in different parts of the machine. The thermal model is based on the heat transfer equations under steady-state conditions to derive the thermal resistances. Radial heat transfer represents the overestimation of the temperatures; however, it simplifies the model. In addition, heat transfer in the rotor is negligible due to the fact that water flowing through the gap is a better platform for heat transfer. There are two modes of heat transfer in the system: one is the conductional heat transfer in the solid parts of the machine and the other is the convectional heat transfer, which happens between stator internal and external surfaces and the ocean water.

A unity volume is considered as shown in Figure 4.55 for the conduction heat transfer calculations. The angular width, inner and outer radius, and axial length are $\alpha, R_\text{i}, R_\text{o}$, and l, respectively. The temperature difference between inner and outer surfaces can be explained as

$$T_\text{i} - T_\text{e} = R_1\phi_\text{i} + R_2 P, \tag{4.109}$$

where T_i is the inner surface temperature, T_e is the outer surface temperature, ϕ_i is the inner flux, P is the volume losses, and R_1, R_2 are the thermal resistances.

R_1 and R_2 can be expressed as

$$R_1 = (R_0 - R_\text{i})(\lambda R_\text{i}\alpha l)^{-1}, \tag{4.110}$$

$$R_1 = (R_0 - R_\text{i})(2\lambda(R_0 + R_\text{i})\alpha l)^{-1}, \tag{4.111}$$

with a large diameter.

Equation 4.109 corresponds to the electrical representation of the thermal network as shown in Figure 4.55.

The surface resistance is used within the model of the convective heat exchanges as

$$R_\text{cv} = (hS)^{-1}, \tag{4.112}$$

where S is the heat exchange surface and h is the convective transfer coefficient.

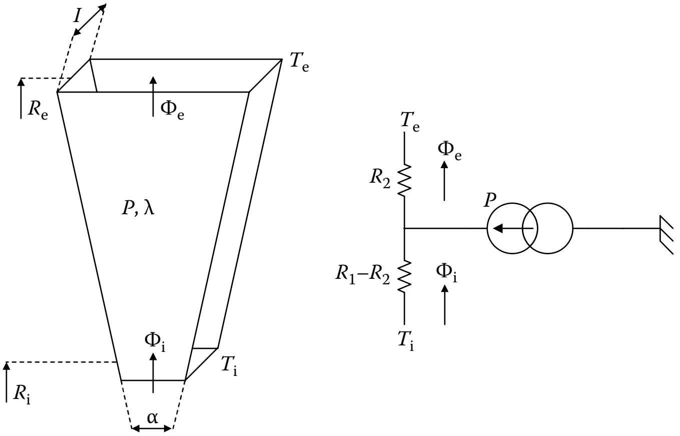

FIGURE 4.55 Unity volume and thermal equivalent circuit.

4.3.5.5 Induction Machines for Ocean WEC

In WEC systems, the last conversion is made by generators that convert mechanical into electrical energy. Generally, variable speed turbines are used in WEC systems. The variable speed causes a variable frequency output and the system will require a frequency converter, that is, a rectifier cascaded by an inverter for grid connection, if synchronous machines are used [57]. The drawback of using synchronous machines might be the requirement of a variable speed, constant frequency inverter system to be placed as an interface between the generator and the grid. An automatic synchronizer system is also needed to synchronize the generator output with the grid, during energy supply. In addition, to provide the field current, a variable DC source is necessary. If PMs are not used, brushes are needed. Brushes feeding the slip rings require regular maintenance.

On the other hand, induction generators running at an oversynchronous speed can supply the energy to the grid [57]. Frequency converters, DC field supply, and synchronization mechanisms might be eliminated by using induction generators. In addition, induction machines do not have brushes and they have squirrel cage rotor, which is capable of operating at higher speeds. Furthermore, induction generators require a simple control mechanism and they are more convenient for grid connection. However, they need reactive power from the grid to provide the excitation and magnetizing the generator. In stand-alone applications, large capacitor banks should be connected in parallel to the stator windings in order to provide reactive power to the induction generator.

There are some considerations to ensure the use of induction generators for WEC systems [57].

During a grid fault, the electrical output power will fall to zero but the mechanical power still will be applied to the generator with an accelerating torque. Thus, the turbine's speed will increase and mechanical protection is required. The generator should be protected from the corrosive effects of the seawater and atmosphere. The generator is subjected to be splashed by sea waves; therefore, the internal windings and other parts need to be protected from enclosure. The induction generator has to be designed for higher range of speed variations for coupling to air turbines.

Induction generators are very suitable to be coupled to the Wells-type turbines. Wells turbines can be categorized into two types: self-starting Wells turbines and non-self-starting Wells turbines. Depending on the turbine type, the induction generator coupling and requirements may vary [58]. In self-starting turbine applications, the induction generator does not need to be excited for initial motion start, while non-self-starting turbines need to be cranked by externally energized induction machines or other machines.

The induction machines are one of the most commonly used electric machines in the industry. Prior to advancements in active power electronic devices, fixed capacitors were used to provide reactive power for excitation of induction generators. This is not a flexible solution since orientation is constant all the time regardless of the load or speed deviations [59]. Excitation might be provided from the grid if induction generators are used within a large power system, in which infinite bus is available. Induction generators should be operated with adjustable excitation and isolation with appropriate control of power electronic switching devices.

The structure of an induction generator consists of two electromagnetic components. The first component is the rotating magnetic field constructed using bars with high conductivity and high strength, which are placed in a slotted iron cage. The second component is the stator winding and stator core. Figure 4.56 shows the cross-sectional view of a typical induction generator [59].

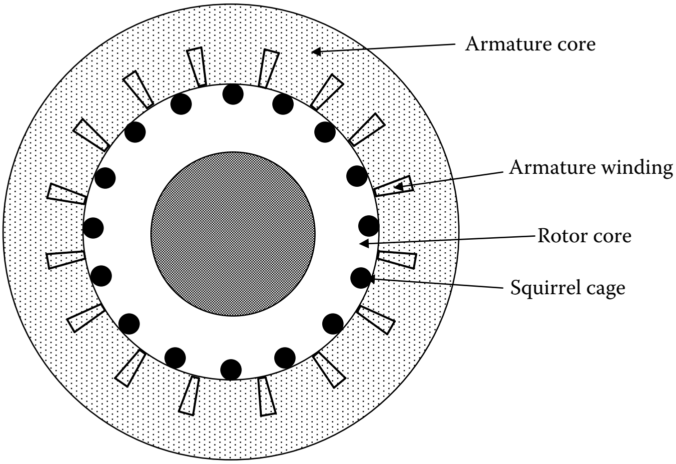

FIGURE 4.56 Cross-sectional view of induction machine structure.

The output of the induction generator is in the form of three-phase AC. The voltage can be controlled to maintain constant output voltage by adjusting the excitation current [59,60]. Thus, the output voltage can be fixed regardless of the load current and speed variations. A controller can be employed to determine the magnitude and frequency of the excitation current. The excitation current should be supplied to the stationary windings from which it is induced into the short circuited rotor windings.

In an induction machine, the synchronous speed and the angular velocity of the rotor can be expressed as

$$n_s = \frac{60}{p} f_n, \tag{4.113}$$

$$\omega_m = \frac{2\pi}{60} n_s, \tag{4.114}$$

where n_s is the synchronous rotations per minute, f_n is the nominal frequency, p is the number of pole pairs, and ω_m is the angular velocity of the rotor.

The mechanical torque produced by the turbines drives the rotor shaft, and this mechanical torque yields the mechanical input to the generator as

$$P_m = T_m \omega_m, \tag{4.115}$$

where P_m is input mechanical power and T_m is the mechanical torque.

The derivative of the angular velocity is

$$\frac{d}{dt}\omega_m = \frac{1}{2H}\left(T_e - F\omega_m - T_m\right), \tag{4.116}$$

where H is the combined rotor and inertia constant, T_e is the electromagnetic torque, and F is the combined rotor and turbine friction constant.

It should be noted that this equation is valid for both motor and generator operations of the induction machine. T_m is negative in the generator operating mode.

The angular rotor position is

$$\frac{\mathrm{d}}{\mathrm{d}t}\theta_\mathrm{m} = \omega_\mathrm{m}. \tag{4.117}$$

The relationship between the induced and terminal voltage of the stator winding is given by

$$V_\mathrm{S} = E_\mathrm{S} - \left(R'_\mathrm{S} + j2\pi f L'_\mathrm{S}\right) I_\mathrm{S}, \tag{4.118}$$

where E_S is the stator voltage induced per phase, R'_S and L'_S are the combined rotor and stator resistance and inductance, respectively, and I_S is the stator current.

The apparent power output of the induction generator can be written as

$$S_\mathrm{n} = 3V_\mathrm{S}I^*_\mathrm{S}. \tag{4.119}$$

The active electrical power output of the machine can be calculated by

$$P_\mathrm{e} = 3\frac{E_\mathrm{S}V_\mathrm{S}}{\sqrt{R'^2_\mathrm{S} + (2\pi f L'_\mathrm{S})}}\sin\delta, \tag{4.120}$$

where δ is the power angle between V_S and E_S.

4.3.5.6 Switched Reluctance Machines for Ocean WEC

Both linear and rotational switched reluctance (SR) machines are suitable for ocean wave applications, since they are brushless and do not have rotor windings. Therefore, they require less and easier maintenance. PM machines are also very suitable for ocean WEC; however, they are more expensive and have relatively bigger size.

The concept of the SR generator is based on the attraction of opposite poles that are magnetically charged [61]. The numbers of salient poles on the stator and rotor are generally unequal. Laminated electrical grade steel is used in their construction.

Cross-sectional view of a switched reluctance generator (SRG) is shown in Figure 4.57 [59], where there are eight stator poles and six rotor poles. 10/8 and 12/10 stator and rotor poles combinations are also possible.

The rotor does not have a winding in an SR generator. Armature coils are isolated from each other; they are concentric and located on stator poles [59]. The corresponding stator poles are magnetized, when the coils on opposite poles are excited such as rotor poles A–A and stator poles 1–1. Voltage is generated in the stator coil, resulting in power production, if the prime mover drives the rotor in the opposite direction.

The output voltage of the SR generator is a DC voltage with high ripples, which should be filtered and regulated by controlling the duration of excitation current.

Linear SR machines can also be suitable for ocean WEC applications.

Figure 4.58 shows a linear SRG cross-section [62], where the translator (moving part) is placed between two stator sides (fixed parts). The generator is a 4/6 machine, which means there are four stator teeth per six translator teeth. Instead of using 4/6 machine, 6/4 design could also be used but 4/6 configuration allows more space for copper in the stator.

In aligned position, the stator teeth face the translator teeth and in aligned position they do not face each other. The current increases to the desired level in the aligned position and steps down to zero in the unaligned position [62]. The flux density is limited by saturation in the

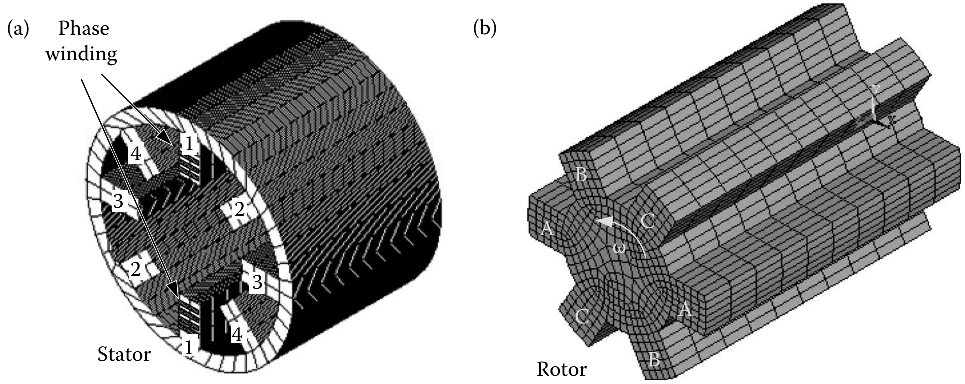

FIGURE 4.57 (**See color insert following page 80.**) 8/6 pole SRG cross-sectional view, (a) stator of the SRG and (b) rotor of the SRG.

aligned position. Flux in unaligned position is lower than the flux of aligned position. The average force can be calculated using the energy conversion area of the flux linkage–current diagram [63] as

$$F = \frac{W_{\text{cycle}}}{x_{\text{cycle}}} = \frac{1}{x_{\text{cycle}}} \int_{\text{cycle}} i\, \mathrm{d}\lambda. \tag{4.121}$$

Here, W_{cycle} is the energy converted in a cycle, calculated as the flux linkage–current loop area, x_{cycle} is the displacement in one cycle, and λ is the flux linkage.

4.3.5.7 Ocean Energy Conversion Using Piezoelectric/Electrostictive Materials

Instead of using linear generators or conventional rotating generators, piezoelectric/electrostrictive materials can also be used for WEC applications. A new device named Energy Harvesting Eel (Eel) is developed by Taylor et al. [64] to convert mechanical energy of ocean waves into electricity for powering remotely located sensors or devices used for

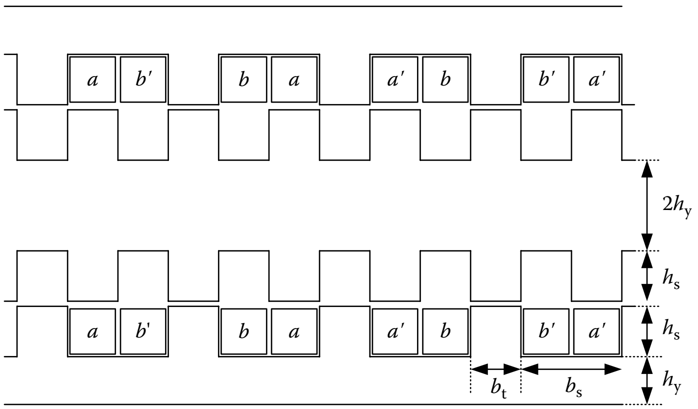

FIGURE 4.58 Linear switched reluctance machine cross-sectional view.

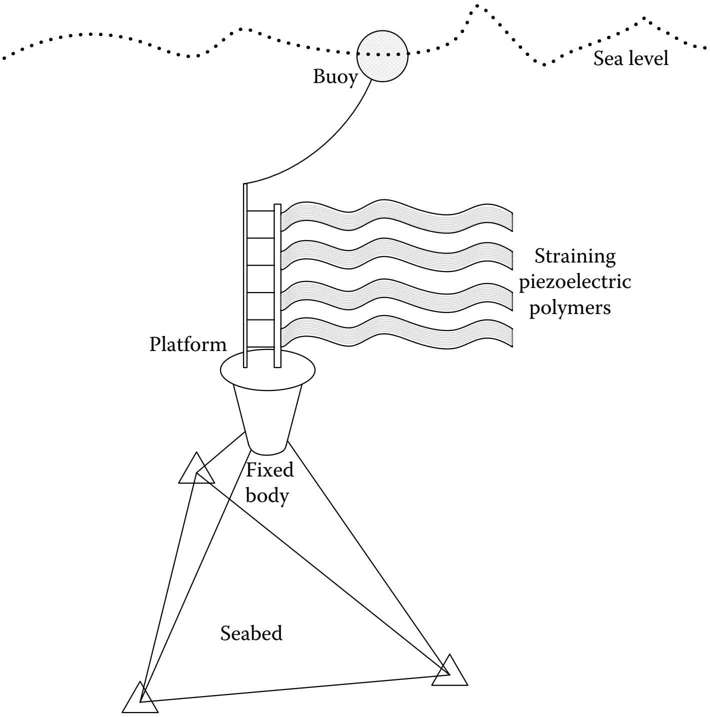

FIGURE 4.59 Eel system structure fixed to the sea bottom.

oceanographic measurements and sampling networks. Long strips of piezoelectric polymer undulates in the water flow are used in this energy harvesting method.

Figure 4.59 illustrates how the piezoelectric polymers are placed at the ocean bottom, using a platform and a fixed body [64].

Figure 4.60 is a schematic showing the forces affecting the Eel.

According to the flow speed and width of the bluff body, bluff body sheds alternating vortices on its either side with different frequencies. The resulting differential pressure caused by the vortices results in the oscillating motion of the Eel. Piezoelectric polymer generates a low-frequency AC voltage along the electrode segment due to the resulting strain on the

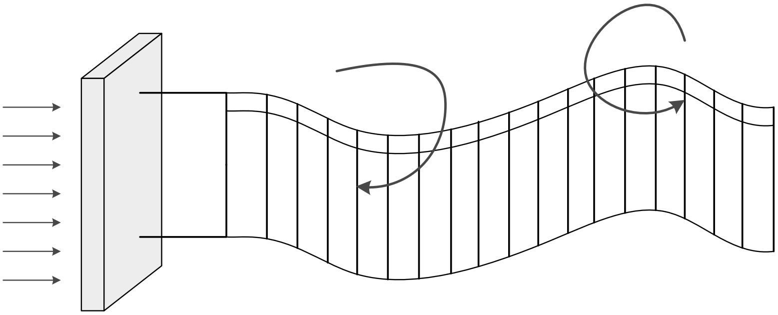

FIGURE 4.60 Eel movement behind the bluff body.

piezoelectric polymer [64]. This voltage can be converted to DC for nearshore transmission or battery charging or supplying power to the oceanographic devices or sensors.

There are multiple layers within the Eel. A central non-native layer (core) and an active layer of the piezoelectric material bonded to each side of the central layer are the three typical layers. The core is a thick and flexible polymer. This flexible structure increases the bending moment around which other layers move. Piezoelectric or electrostrictive materials are used in the generating layer construction. The strain in the active layers should be maximized in order to obtain more power [64].

The Eel undulating in water flow produces the electrical power, P, which is given by

$$P = \frac{\eta_1 \eta_2 \eta_3 A \rho V^3}{2}. \tag{4.122}$$

In this equation,η_1 is the hydrodynamic efficiency and depends on the oscillating frequency of the Eel and the frequency of the vortex shedding behind the bluff body. If these two frequencies match each other, hydrodynamic efficiency increases. In Equation 4.122, η_2 is the conversion efficiency of the strain into electrical energy in the piezoelectric polymer, η_3 is the efficiency of the electrical extraction out of the piezoelectric polymer, which is provided by the resonant circuit, A is the cross-sectional area, ρ is the water density, and V is the water flow velocity.

The flow-driven oscillation of the Eel is similar to a flag behind a pole on a windy day [65]. Strain can be calculated by visually recording the curvature of an Eel in a flow tank and electrically measuring the open-circuit voltage of the segment electrodes [64]. The Eel motion can be described either as a sum of natural frequency modes or as a traveling wave. Changing the Eel system parameters by changing bluff buoy width or Reynolds number in the flow affects the operation of Eel.

To convert the mechanical energy of the water flow into electrical energy, piezoelectric polymers are used. The power obtained from a piezoelectric material per unit volume, P_o, [66] is

$$P_o = \frac{\pi d_{31}^2 s^2 Y^2 f}{2\varepsilon\varepsilon_0}, \tag{4.123}$$

where d_{31} is the mechanical-to-electrical coupling parameter of the piezoelectric material, s is the mechanically strain percentage of the material, Y is the Young's modulus of the material, ε is the material's dielectric constant, and f is the straining frequency of the material. The electromechanical coupling efficiency is given by

$$k_{31}^2 = \frac{d_{31}^2 Y}{\varepsilon\varepsilon_0}. \tag{4.124}$$

Piezoelectric polymer PVDF has been utilized within the Eels. This polymer has advantages such as the following: it is resistant to a wide variety of chemicals and is mechanically strong. In addition, they can be manufactured as continuous reel, which allows them to be fabricated at low costs and different ranges of widths and lengths. The only drawback of the PVDF polymer for the Eel application is the relatively lower piezoelectric constant, d_{31}. This causes the lower conversion efficiency (k_{31}) and, as a result, a lower output power (P_o) produced by Eel [64].

Electrostrictive polymers are an alternative for conventional piezoelectric polymers in Eel for better performance. It is possible to induce a large piezoelectric field by keeping a high DC electrical bias field E_B. The induced piezoelectric effect is a result of Maxwell stress in the dielectric. AC mechanical stress applied to the electrically DC biased polymer causes dimensional differences in the electrostrictive dielectric. Thus, through the electrodes attached to the polymer surface, an alternating electrical charge flows. For an electrostrictive polymer, the effective d_{31} can be defined as

$$d_{31} = \frac{\varepsilon\varepsilon_0}{Y}\frac{V}{\text{th}}. \tag{4.125}$$

So the k_{31} efficiency becomes

$$k_{31}^2 = \frac{\varepsilon\varepsilon_0}{Y}\left(\frac{V}{\text{th}}\right)^2, \tag{4.126}$$

where V is the generated AC voltage and th is the electrostrictive polymer thickness.

Electrostrictive polymers have much higher values of d_{31} and k_{31} and hence output power (P_o) than piezoelectric polymer, PVDF. The electrostrictive polymers can harness more power when they have higher k_{31}^2 values [64].

However, there are some drawbacks of electrostrictive polymers such as weaker mechanical strength, low electrical breakdown strength, high dielectric losses, and lack of commercial sources with desired features. These drawbacks make electrostrictive polymers impractical for use in Eel.

The switched resonant-power conversion technique is used for electrical power extraction from the polymers. Using electrical and mechanical resonant systems, we can overcome the low coupling factor $k_{31}^2 = d_2^{31}(Y/\varepsilon)$ when piezoelectric devices are used as power generators. Eel motion has a very low frequency such as 1–2 Hz, so direct electrical resonance is not practical, since it requires very large inductor values. Therefore, switched resonant power conversion may overcome this limitation. Using this conversion, this technique is capable of high-efficiency operation at the 1–2 Hz range using reasonable inductor values [64].

Figure 4.61 shows the circuit schematic of the switched resonant power converter used for Eel energy harvesting [64].

In this circuit, R_P represents the dielectric loss resistance of the piezoelectric (PVDF), C_P is the Eel capacitance, and V_{OC} shows the open circuit voltage of the Eel with respect to

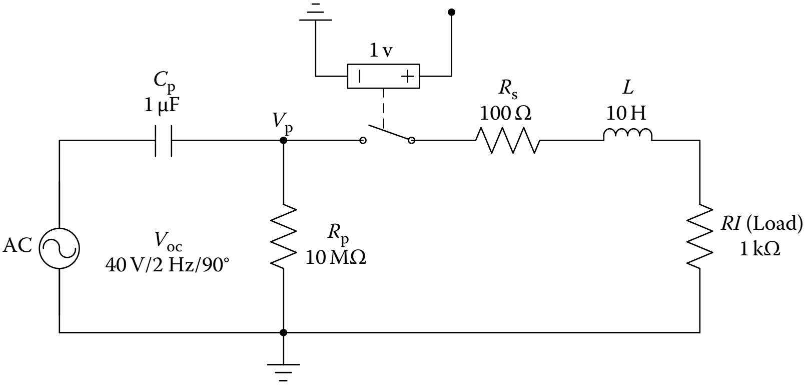

FIGURE 4.61 Switched resonant power converter.

an applied strain [64]. Eel can be modeled using these three fundamental elements. The other circuit components belong to the external power conversion circuit. These are the switch (S), inductor (L), with the series winding resistance (R_S) and R_L represents the load resistance.

It is assumed that the input to the piezoelectric element is a sinusoidal source. The switch S is turned on at the positive and negative peaks of input for exactly one-half cycle of the resonant period of the L–C_P network. The closure time for the switch is

$$T_C \approx \pi\sqrt{LC_P}. \tag{4.127}$$

T_C equals 7.18 ms for the given typical values. The voltage during the closure interval can be calculated as

$$V_C(t) = V_N \exp\left(-\frac{\omega_0 t}{2Q_L}\right)\cos(\omega_0 t), \tag{4.128}$$

with initial voltage, V_N, across the capacitor C_P. Here,

$$\omega_0 = \frac{1}{\sqrt{LC_P}} \tag{4.129}$$

and

$$Q_L = \frac{\omega_0 L}{R_L + R_S} = \frac{\sqrt{L/C_P}}{R_L + R_S} = \frac{R_0}{R_L + R_S}. \tag{4.130}$$

The current of the inductor (L) during this closure period can be calculated as

$$i_L(t) \approx \frac{V_N}{R_0}\sin(\omega_0 t). \tag{4.131}$$

At $t = T_C$ switch S opens and the voltage becomes

$$v_C(T_C) = -V_i \exp\left(-\frac{\pi}{2Q_L}\right) = -aV_i \quad (a \approx 1) \tag{4.132}$$

and

$$i_L(T_C) = 0 \tag{4.133}$$

when the switch opens. The "a" is defined as

$$a \equiv \exp\left(-\frac{\pi}{2Q_L}\right). \tag{4.134}$$

The switch remains open till the next peak (negative) occurs and then recloses. During this open period, V_C keeps charging more negatively because the strained piezo element produces a charge [64]. The variation of $V_C(t)$ during this period is

$$V_C(t) = V_P\cos(\omega_{IN} t) - (aV_N + V_P)\exp\left(\frac{t}{\tau}\right), \tag{4.135}$$

where the time constant of the dielectric loss network of the piezo is

$$\tau = R_P C_P, \tag{4.136}$$

and V_P is the peak value of the open-circuit voltage. S closes for the same period T_C at the next peak and behaves similarly except that $(V_i)+$ is now a higher value. Prior to the next closure period at

$$t = \frac{1}{2f_{IN}} \omega_{IN} t = \pi, \tag{4.137}$$

the voltage V_C reaches a value V_{N+1}, which can be expressed as

$$V_{N+1} = -\left(V_P(1+b) + abV_N\right). \tag{4.138}$$

In Equation 4.138,

$$b \equiv \exp\left(\frac{-1}{2f_{IN}\tau}\right) = \exp\left(\frac{-\pi}{Q_C}\right), \tag{4.139}$$

where

$$Q_C = 2\pi f_{IN}\tau = \frac{1}{\tan\delta}. \tag{4.140}$$

This process repeats every half cycle till the steady-state condition is reached. It should be noted that the polarity of waveform changes in every half cycle. The steady-state condition occurs when the energy transferred to the load R_L plus losses in the inductor, electrodes, and PVDF dielectric is offset by the energy added by the piezoelectric device.

Equation 4.138 allows us to recursively predict the build-up voltage as a number of half cycles of the input. The build-up of the voltage requires approximately Q_L cycles. The steady-state power conveyed to the load can be determined by the steady-state voltage. The steady-state voltage can be obtained by setting V_{N+1} to V_N in Equation 4.138, which yields

$$(V_C)_{SS} = V_P \frac{1+b}{1-ab}. \tag{4.141}$$

A half sine current wave is applied to the load, which is produced by the peak voltage. The width of the current pulse is T_C and peak amplitude can be written as

$$(I_L)_{MAX} = \frac{(V_C)_{SS}}{R_0}. \tag{4.142}$$

Consequently, the average power output can be expressed as

$$P_{OUT} = \left((I_L)_{MAX}\right)^2 R_L T_C f_{IN}. \tag{4.143}$$

High-voltage build-up across the reactive elements depends on Q in a switched resonant power converter. The resonant frequency and the input frequency can be different in this switching technique. This is the most important advantage of this circuit. This results in the possibility of reduced component ratings.

If the loss elements can be minimized, the output power can be maximized. The losses are caused by the winding resistance of the inductor, the resistance of the electrode, and the dielectric. As in other resonant systems, the optimum value of the R_L will maximize the power output. Using Equations 4.131 through 4.133, the optimum value of the R_L can be obtained. If we assume that parameters a and b are both 1 for large values of Q_L and $Q_C(>5)$. Therefore, the steady-state value of $(V_C)_{SS}$ can be rewritten as

$$(V_C)_{SS} \approx \frac{2V_P}{\pi\,(1/2Q_L + 1/Q_C)} = \frac{4V_P Q_L Q_C}{\pi(2Q_L + Q_C)}. \tag{4.144}$$

Therefore, the power output becomes

$$P_{OUT} = (V_C)_{SS}^2 T_C f_{IN} \frac{R_L}{R_0^2} \approx \frac{16 C_P V_P^2 Q_L^2 Q_C^2 f_{IN} R_L}{\pi R_0 (2Q_L + Q_C)^2}. \tag{4.145}$$

The mechanical input power is

$$P_{IN} = \frac{C_P V_P^2 f_{IN}}{2k_{31}^2}, \tag{4.146}$$

where the mechanical coupling factor could be recalled as

$$k_{31}^2 = d_{31}^2 \frac{Y}{\varepsilon}. \tag{4.147}$$

Accordingly, the power conversion efficiency can be described as the ratio of P_{OUT}/P_{IN}

$$\eta = \frac{32k_{31}^2}{\pi R_0} \times \frac{Q_L^2 Q_C^2}{(2Q_L + Q_C)^2} R_L. \tag{4.148}$$

Q_L can be substituted with $R_0/(R_L + R_S)$ and maximizing with respect to R_L, the optimum value of R_L can be found as

$$(R_L)_{OPT} = R_S + \frac{2R_0}{Q_C}, \tag{4.149}$$

$$(Q_L)_{OPT} = \frac{R_0}{2\,(R_S + R_0/Q_C)}. \tag{4.150}$$

Integrating Equations 4.149 and 4.150 yields the maximized conversion efficiency as

$$\eta_{MAX} = \frac{8k_{31}^2 R_0}{\pi\,(R_S + 2R_0/Q_C)}. \tag{4.151}$$

Using the typical parameter values given in Figure 4.61, the maximum efficiency can be calculated as 37% for the piezoelectric polymer-based ocean energy harvesting.

4.3.6 Grid Connection Topologies for Different Generators Used in Wave Energy Harvesting Applications

The outputs of the generators generally have fluctuating characteristics due to the variable wave profiles. Thus, the generator outputs need further conditioning prior to grid connection or supply energy to the stand-alone loads. In this subsection, the different grid connection topologies with various generators and power electronic interfaces are discussed.

In this subsection, the grid interfaces for wave energy applications with linear and synchronous generators are described. As given in the general system-level diagram in Figure 4.1, grid or load interface topologies should be used with WEC applications. Figure 4.62 illustrates the system with several wave energy converter devices and an equivalent power electronic interface.

Instead of having a common interface technology for grid connection, individual power electronic interfaces can be employed for each WEC device. Placing several wave energy converters may reduce the output power fluctuations of the generators (represented by *G*). This may also reduce the need for energy storage devices; however, other methods should be implemented within grid interface technologies for better power smoothing and grid connection issues.

4.3.6.1 Grid Connection Interface for Linear and Synchronous Generator Applications

The wave energy harvesting applications involving generators are generally built in farms structure. Using several power generation units helps reduce the power fluctuations due to different periods and heights of waves [67].

A typical grid connection interface for use with generator applications is presented in Figure 4.63. Although using several units has an effect on obtaining better overall waveforms, further conditioning is necessary for grid connection. Several WEC units have output voltages with different amplitudes, frequencies, and phases. DC bus voltage variations can be lowered if many units are connected together. After the rectification stage, capacitor tanks should be placed for better suppression of the DC bus voltage variations. The capacitor bank acts as a short time energy buffer for the sustainability of energy transfer to the grid, if any of the units does not meet any incident wave for a short time. These capacitors are also used for the determination of the neutral point and the output filter of the inverter. The third stage consists of a six-pulse insulated gate bipolar transistor (IGBT) inverter. This inverter should be controlled to synchronize the inverter output voltage with grid quantities such as voltage amplitude and frequency. The synchronization is generally provided

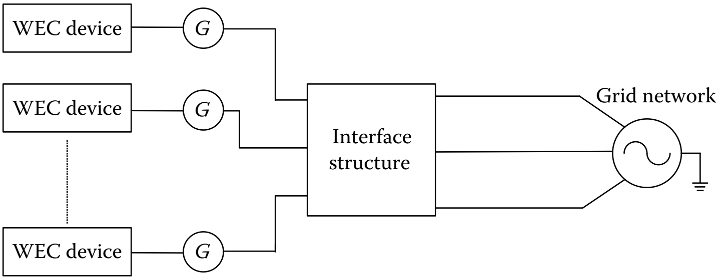

FIGURE 4.62 The interface structure for induction generator-based wave energy converters.

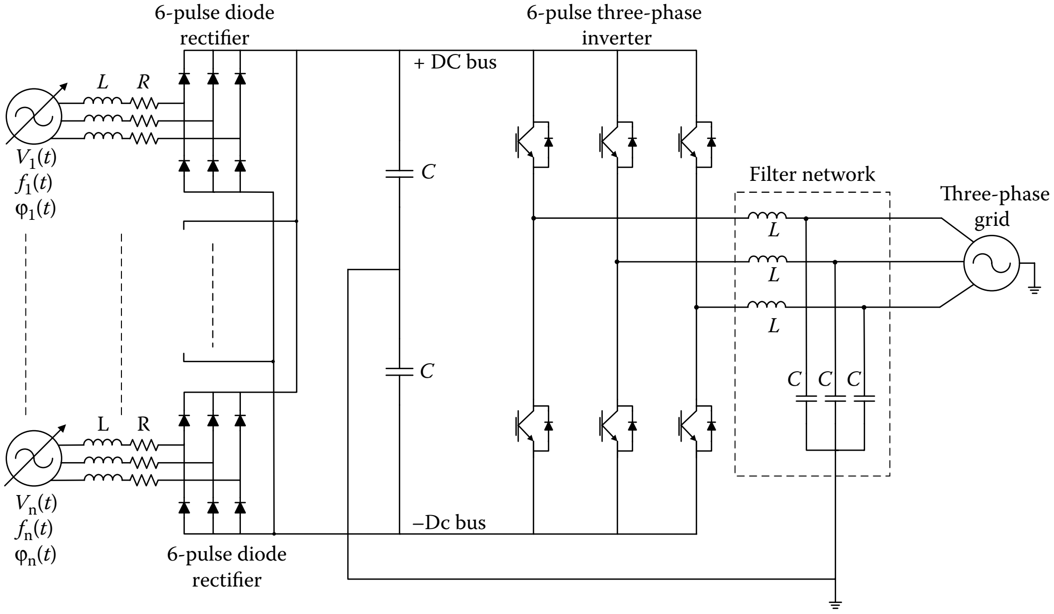

FIGURE 4.63 Grid connection interface for applications using different generators.

using the generator voltage, grid voltage, and the voltage difference between these two. After each phase–phase voltage comparison, the difference is processed for space vector computation for use in the inverter switching controller.

A low-pass LC filtering network is used in the fourth stage. The inductance and the capacitance values for this filter network should be determined to suppress the higher frequency components of the inverter output voltage. Thus, the cut-off frequency of the filter should be a little bit higher than the grid frequency to avoid filtering the fundamental frequency component. After the filtering stage, the output of the network is synchronized, filtered, and qualified for grid connection. This topology is suitable for applications with linear generators and three-phase synchronous generators and squirrel cage induction generators.

4.3.6.2 Grid Connection Interface for Induction Generator Applications

There might be several grid connection interfaces for the systems with induction generators such as an induction generator with a shunt connected static synchronous compensator (STATCOM), an induction generator in series with full converter, and a DFIG [68].

4.3.6.2.1 Induction Generator with Shunt-Connected STATCOM

An induction generator with a shunt-connected STATCOM is shown in Figure 4.64.

STATCOM is capable of injecting and absorbing reactive power to the network to overcome voltage fluctuations. STATCOM is a device with a bidirectional converter and a capacitor connected to the DC side [69]. The AC side of the STATCOM is used to compensate for the voltage fluctuations and low-voltage ride through (LVRT) [70]. A larger energy storage device can be employed at the DC side of the STATCOM for compensation of active power fluctuations originated by the natural behavior of wave power. The magnitude and duration of the voltage drop or swell, generator, and grid parameters are used to determine the rating of the STATCOM.

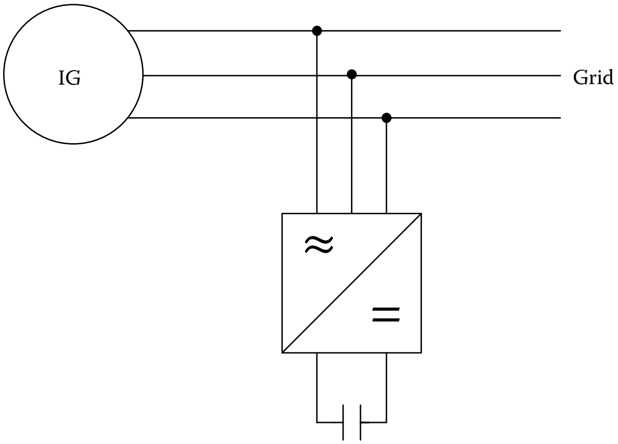

FIGURE 4.64 Induction generator with a shunt connected STATCOM.

The voltage fluctuations magnitude also depends on the strength of the grid and the impedance angle of the connection line. The greater impedance angle and weak grid cause large variations [68].

Direct torque control is not possible on the generator if the STATCOM is used as the interface topology. Hence, this topology can be enhanced with a hydraulic power take-off (PTO) system with an active control and energy buffering system such as a high-pressure accumulator. This is also a similar approach to the Salter Cam method in which a pressurized hydraulic fluid is used to drive the hydraulic motor, which in turn drives the electric generator [4]. This also acts as a mechanical energy buffer [68].

The schematic configuration of the hydraulic PTO system is shown in Figure 4.65. The hydraulic PTO is composed of a hydraulic piston, a high-pressure accumulator, and a hydraulic motor. The high-pressure accumulator smoothes the mechanical power fluctuations caused by the wave power absorbers; thus power input to the induction generator will be smoother but may have more or less fluctuations. The electrical storage may help in smoothing the residual power fluctuations [68]. However, it would be better to handle the power smoothing at the same conversion stage, if the dimensions and cost of the conversion and storage would stay in a reasonable range. STATCOM could also be used as an electrical

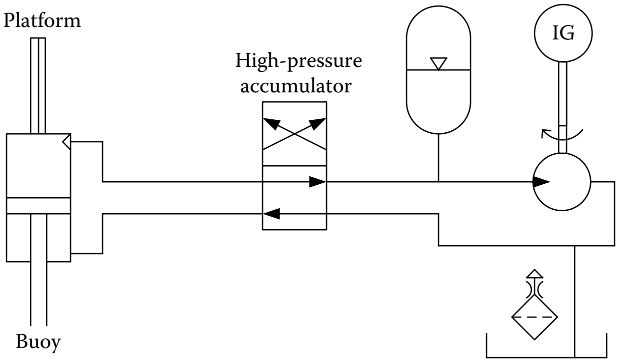

FIGURE 4.65 Energy buffer system using a hydraulic PTO system with induction generator.

power compensation device and provides some residual power smoothing effect due to the energy storage in the DC link [71].

4.3.6.2.2 Induction Generator in Series with Full Converter

Figure 4.66 shows the induction generator connected to a full converter as grid interface technology [68].

There are two cascaded voltage source converters, one of them is an AC/DC converter and the other one is a DC/AC converter. The coupling point of these two converters is associated by a DC link. The generator side converter provides magnetizing current required for generator excitation and to control the electromagnetic torque. The grid side converter compensates for the voltage, power factor, and power flow.

This full converter approach allows the variable speed operation of the generator and active control of the electromagnetic torque. Thus, voltage sags and power unbalance problems can be solved with increased capability of riding through the fault [68].

WEC having full converters cannot significantly contribute to the fault currents if a short circuit occurs in the network, because during transients, they cannot deliver more than a few times of rated current. In terms of LVRT, the optimum technology is a full converter, which has greater margin than the STATCOM [72]. However, the rating of the full converter depends on the flowing current, since they are in series and therefore the components are bigger in size and more expensive than that of the STATCOM.

The electromagnetic torque can be actively controlled by the vector control technique. The generator side converter can provide a latching force in the case of latching. A mechanical brake system could reduce the converter duty in a combined solution.

4.3.6.2.3 Doubly Fed Induction Generator

In the DFIG topology, the rotor windings are not short circuited. Hence, the generator should be wound instead of squirrel caged as seen from Figure 4.67. The outputs of the rotor windings are associated with an AC/DC converter, a DC-link capacitor, and another DC/AC converter for grid and generator stator windings connection points [73].

This converter connection is called back-to-back converter, which is in series with rotor windings and shunt on the grid wires. With the aid of the hydraulic smoothing stage, the generator speed does not change too much, so the converters have lower ratings in comparison to the full converter in series [73]. However, doubly fed topology is not suitable for direct drive. The rotor side converter is used to control the power output of the system and the voltage (or reactive power) measured at grid connection terminals. The grid side converter generates or absorbs the reactive power by regulating the voltage of the DC bus

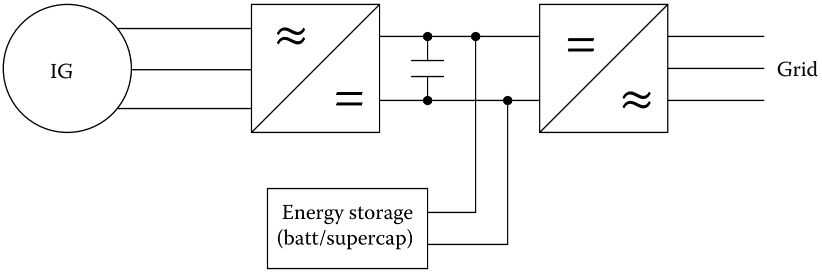

FIGURE 4.66 Induction generator in series with a full converter as grid interface technology.

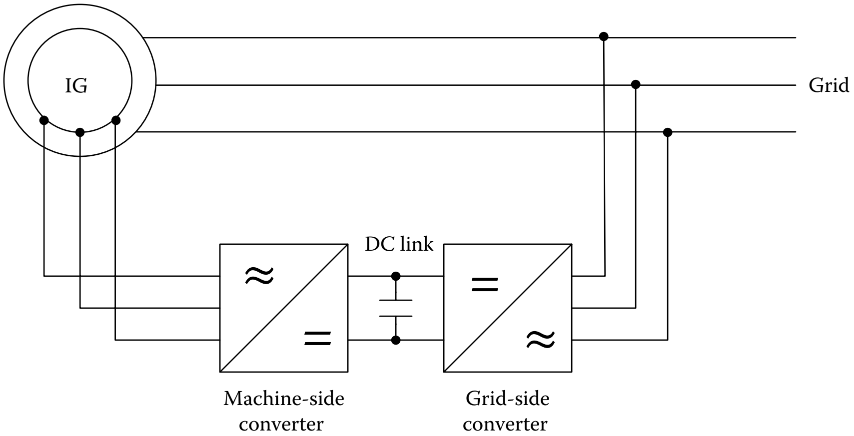

FIGURE 4.67 DFIG topology with back-to-back converters.

capacitor [74]. In other words, the rotor side converter controls magnetizing current and electromagnetic torque, while the grid side converter is controlled similar to STATCOM control [72]. In this topology, the rating of the converter limits the range of the variable speed operation. So it does not have as much capability as the full converter in the active control. The larger control margins can be reached by increasing the converter ratings, which in turn increase the cost. Thus, the full converter provides more flexibility of control.

The system performance can be the same as a fixed speed generator in a STATCOM [73]. This structure is very common in wind farms, and the same technology can be implemented in WEC systems with a hydraulic PTO system.

4.3.6.3 *Grid Connection Interface for SRG Applications*

An overall diagram of the grid connection interface for a SRG is given in Figure 4.68 [75].

The torque is a function of the angular position of the rotor due to the variable reluctance of SRGs. The phase currents of the SR generator should be controlled by the power electronic controller according to the certain positions of the rotor. In order to control the torque and transfer the available power to the grid, the magnitude and the waveform of the phase currents should be regulated by the power electronic interface. The safe operation of the

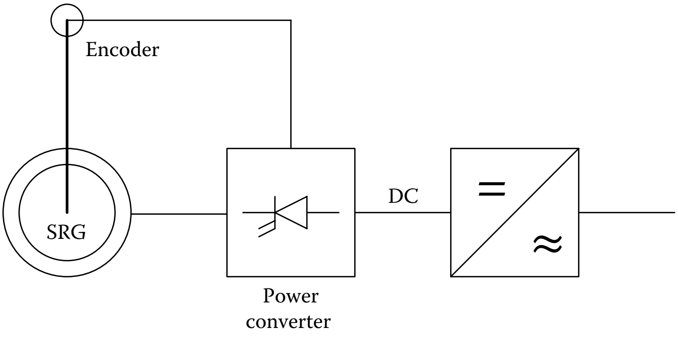

FIGURE 4.68 Overall grid connection diagram of an SRG.

generator is also provided by the power electronic converter. The converter is used to invert the voltages generated by the phases according to the certain positions of the rotor. The converter also provides the phase commutations of the voltages generated by multiphase SRG. The DC-link capacitor connected to the DC bus is used to reduce the oscillations of the output voltage.

The output power over each pulse exceeds the excitation by supplied mechanical power if the losses are omitted [76]. In this condition, the output power of the SRG can be calculated as

$$p(\theta, i_1, i_2, \ldots, i_n) = \left(\frac{1}{2} \sum_{j=1}^{n} \frac{\mathrm{d}L_j(\theta)}{\mathrm{d}\theta} i_j^2 \right) \omega, \tag{4.152}$$

where p is the instantaneous extracted power, n is the number of phases, j is the phase number, θ is the rotor position, ω is the rotor speed, i_j is the current of the phase j, and $L_j(\theta)$ is the inductance of phase j as a function of the rotor position. This equation is valid if the saturation is neglected and each phase is magnetically independent. The average output power equals the mechanical power without losses. Thus, the average power and the torque of the generator are

$$P = T_\mathrm{m}\omega, \tag{4.153}$$

$$T_\mathrm{m} = \frac{N_\mathrm{r}}{2\pi} \int_0^{2\pi/N_\mathrm{r}} \left(\sum_{j=1}^{n} \frac{1}{2} \frac{\mathrm{d}L_j}{\mathrm{d}\theta} i_j^2 \right) \mathrm{d}\theta, \tag{4.154}$$

where P is the average power, T_m is the torque, and N_r is the number of rotor poles.

The grid connection interface of an SRG consisting of power electronic converters and the control circuitry are shown in Figure 4.69 [77]. There are two MOSFET transistors and two diodes per phase in the power circuit, which provide the maximum efficiency and control flexibility with minimum passive elements. The integrated diodes within the MOSFET switches additionally build a full bridge diode rectifier resulting in the shorter charge time of the DC-link capacitor.

The control system of the SRG power electronic interface consists of position sensing elements, synchronization circuitry, commutation logic, and PWM generators [77]. The components of the power electronic interface are shown in Figure 4.69. A magnetic encoder consists of a magnet ring commutator mounted on the rotor and two Hall-sensor ICs used for position detection. The PWM generators are current-mode controllers that are synchronized with digital circuitry and generator voltage and torque references [75]. The block diagram shown in Figure 4.70 presents a current control with torque reference applied to the SRG. The waveforms of the reference currents ($i_1^*, i_2^*, i_3^*, i_4^*$) are obtained using the trapezoidal model torque ($T_1^*, T_2^*, T_3^*, T_4^*$) corresponding to each phase.

The converter operates in three different modes, which are charging mode, voltage build-up mode, and generating mode. The DC-link capacitor is charged by the alternating EMF of the PM flux through the diode rectifier in the charging mode. In this mode of operation, the converter operates in a passive mode. The DC-link capacitor is charged up to the peak value of induced EMF of the phase, where the PMs are placed. This voltage varies according to the machine speed and PM flux power.

The capacitor voltage is increased up to the rated voltage during the voltage build-up mode. The MOSFETs are switched actively during this mode. Generally, the excitation

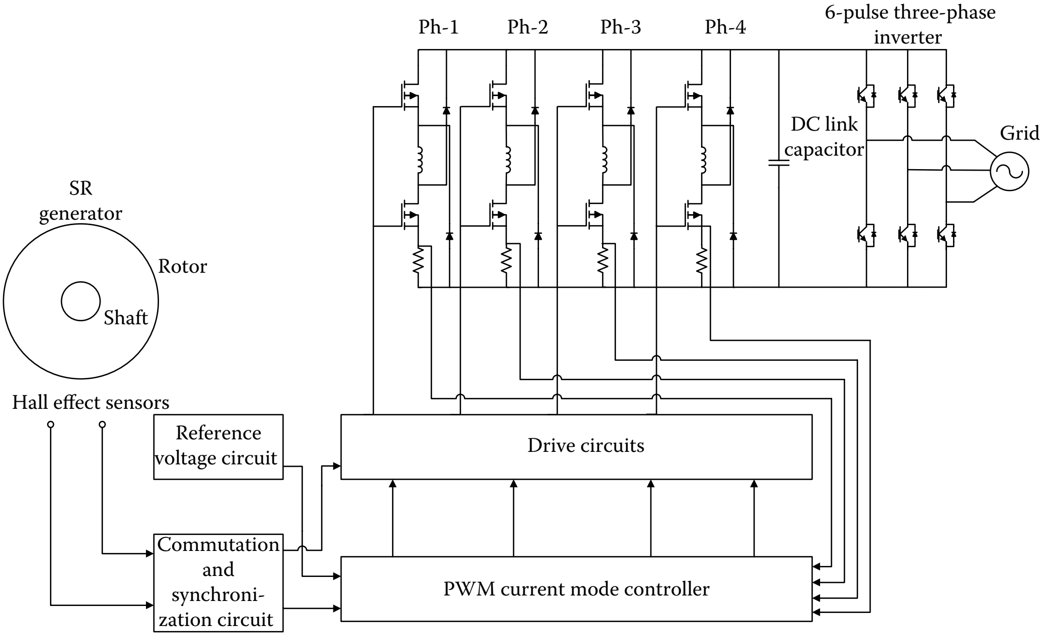

FIGURE 4.69 Power electronic converter and controller for SRG grid connection.

power is first supplied from the capacitor, while transistors are conducting. The capacitor voltage turns at a point slightly before and after the aligned position. So, the bulk of the winding conduction period comes after the alignment. Current begins to rise while the rotor poles approach the stator poles of the next phase, which is going to be excited [77]. The phase current increases with extracting energy from the DC-link capacitor till the switches are turned off. The turn off event happens at the commutation angle, which is determined by the control circuit.

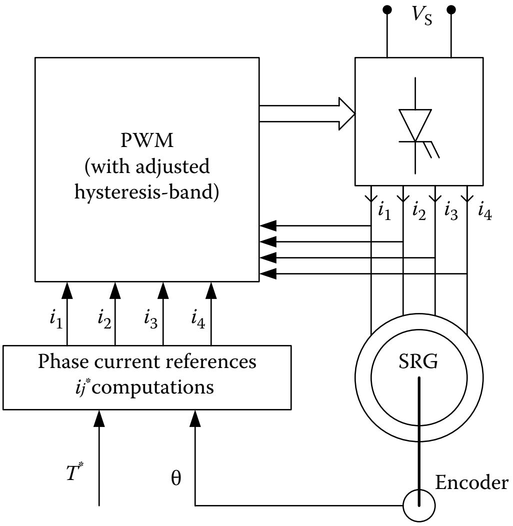

FIGURE 4.70 Block diagram of the operating principle of grid-connected SRG.

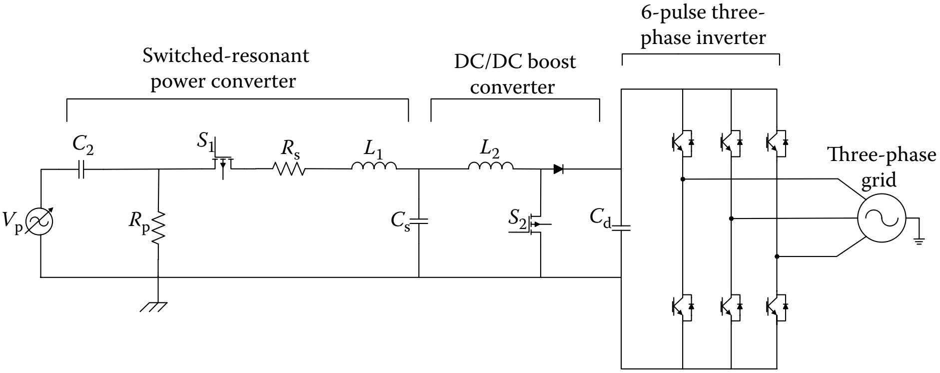

FIGURE 4.71 Power electronic interface schematic for piezoelectric/electrostrictive generators.

The current in the switches is commuted to the diodes, when the switches are turned off till the current reaches zero. The terminal voltage then reverses by the freewheeling diodes. During this defluxing period, the DC-link capacitor receives the returned generated power. The direction of energy flow switches from the machine to the capacitor resulting in the increase of capacitor voltage.

The energy returned during the defluxing period should be greater than the excitation energy supplied when the switches are on for sustainable generating action and to produce a voltage increase during the build-up mode [77]. The prime mover produces the difference between the electrical input energy and the electrical output energy. The energy flow can be regulated by the turning-on times of the switches.

4.3.6.4 Grid Connection Interface for Piezoelectric/Electrostrictive Power Generators

Although the power generated by piezoelectric/electrostrictive generators is relatively low, a power electronic interface can be used for grid connection for the applications composed of a large number of units. The power electronic interface consists of a switched resonant power converter, a DC/DC boost converter, and a DC/AC inverter.

The circuit schematic of this power electronic interface is illustrated in Figure 4.71.

The switched-resonant power converter is used for extraction of maximum energy from the straining materials. The operation principle of this circuit is described in detail in Subsection 4.3.4.5.7. The boost converter is connected to the output of the switched-resonant power converter. This DC/DC boost converter is used to step-up the output voltage of the piezoelectric units, which will be then inverted to the AC voltage. The duty ratio of the boost converter is determined according to the output voltage of the resonant power converter and the grid voltage effective value. The PWM control should be used for the inverter control in order to synchronize the output voltage in terms of modulation index, output voltage magnitude, phase angle, and frequency.

4.4 Wave Energy Applications

There are several types of technologies to convert ocean wave power into electricity. All technologies have advantages and drawbacks in terms of efficiency, maintenance, operation costs, establishment difficulties, and power rating. Some of the mainly used wave energy harvesting technologies are as follows: OWC, Overtopping devices, Pelamis, Wave Dragon, Archimedes wave swing (AWS) device, Wave Star Energy (WSE), and magnetohydrodynamics (MHD) generator.

OWC systems consist of a partially submerged structure, which forms an air chamber, with an underwater opening that allows the seawater to flow into the chamber. The volume of air inside the chamber is compressed as the water rises inside the chamber, driving air through a turbine. As the water level in the chamber subsides, the air is drawn back through the turbine. Bidirectional and self-rectifying air turbines have been developed. The axial-flow Wells turbine is the best-known turbine for this kind of application and has the advantage of not requiring rectifying air valves [78].

Overtopping devices: Overtopping devices guide incoming waves into a reservoir raised slightly above sea level, through a ramp. The water trapped in the reservoir flows back to the sea through a conventional low-head hydroelectric generator.

Float systems: Their common feature is a buoy that sits on the ocean's surface. The motion of this buoy is converted into electricity typically by a hydraulic PTO such as a hydraulic ram. These float systems have various shapes and forms.

Hinged contour devices: Hinged contour devices contain different floating sections, which are hinged together. As the wave passes, the sections move relative to each other and the hinges produce power. The power conversion uses hydraulic elements.

4.4.1 Oscillating Water Column

The OWC is one of the most common and most maturated WEC devices [79]. The conceptual studies on OWC started in the 1970s. Up to date, a number of plants were built in different countries such as Osprey, Scotland, and in Japan, which is called Mighty Whale.

The upcoming waves enter the water column, which is placed in the lower part of the chamber. This wave action on the water column occurs through the submerged entrance located on the device's front side [80].

As the water level increases, the air pressure in the upper part of the chamber increases. In other words, the oscillatory motion of the water causes a difference in air pressure within the chamber. The turbine is located in a channel, which links the air chamber to the outside. The axial airflow direction reverses when the wave level and the air pressure decrease [81]. The turbine should be specially designed in order to rotate in the same direction as air, since the airflow direction is bidirectional. Wells turbines are employed within the most full size OWC applications. These turbines are generally ranging from 500 kW up to 1 MW depending on the diameter sizes of 2 and 3.5 m. When employed together with flywheels, a reasonable kinetic energy can be stored in order to smooth the power fluctuations.

In a typical OWC application, the peak pressures vary in the range of 1.1–1.3 bars. Using relief and throttle valves, the pressure and airflow rate can be controlled and limited not to exceed critical values.

The greatest disadvantage of the OWCs is the large base structure, where its cross-sectional area varies around 100–400 m^2 with the chamber height of 10–20 m. As a result, the cost of a single device is rather high. Integrating several devices in a breakwater structure may increase the overall cost of the power plant. The most important advantage of the OWC is that the moving mechanical parts, that is, the turbine and the generator, are not in direct contact with water. Two large-scale OWCs are in service in Portugal (1999) and in the U.K. (2000), which are called Pico and Limpet power plants, respectively. Other OWCs were built in Japan, Australia, India, and Norway [80,82–85].

4.4.2 Pelamis

Pelamis is designed and applied by an Ocean Power Delivery Company, which is located in Scotland, U.K. The photograph of Pelamis is shown in Figure 4.72. Pelamis is a floating offshore hinged contour device [75].

The Pelamis consists of a long articulated structure with four cylindrical bodies [86,87]. These bodies are linked by hinged joints in series. These joints move under wave action, as the cylinders make the motions of pitch and yaw. The inner hydraulic rams pump high-pressure oil to activate hydraulic motors via smoothing accumulators. The electric generator is driven by these motors [88]. The stiffness of the joints can be adjusted to provide the tuning of the device according to the sea conditions. The reduced cross-sectional area helps the survivability of the device by limiting the drag forces. The longitudinal axis should be fixed parallel to the wave direction by moorings.

The side and plan view of the Pelamis is shown in Figure 4.73 for better understanding of its operation.

In Orkney, U.K., a full scale prototype was built and deployed for testing. In 2004, Pelamis delivered electrical power to the grid for the first time. This prototype is 150 m long and the rated power is 750 kW. The outer diameter of the cylinders is 3.5 m and three of four cylinders hosted inside can independently generate rated power of 250 kW.

The Pelamis wave energy converter is derived from earlier trials such as the Nodding Duck [6] developed by S. Salter in 1974 and Cockerell Raft designed by Sir C. Cockerell [4]. However, Pelamis offers a more cost-effective solution, which is available on market. In Portugal, a small wave power farm of three units with 2.25 MW power rating is under deployment [80].

A single floating Pelamis device can be moored at a water depth of 50–60 m. An umbilical riser cable connects the Pelamis to a junction box on the ocean floor. From this junction box,

FIGURE 4.72 (**See color insert following page 80**.) Pelamis WEC device at sea (Ocean Power Delivery Ltd). (Courtesy of R. Henderson, *Renewable Energy*, 31 (2), 271–283, 2006.)

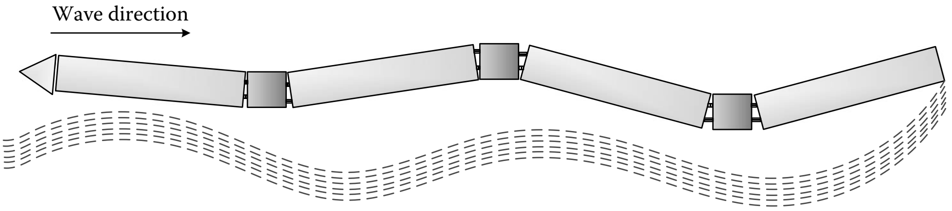

FIGURE 4.73 (**See color insert following page 80**.) General layout of the Pelamis WEC device.

a double-armored three-phase cable is buried into soft sediments along a 3 km route leading to the outfall of the effluent pipe, which is 1 km offshore. The cable is then routed through the 5 km effluent pipe to the International Paper Facility, which is about 4 km inland. An additional cable section connects to the Gardiner substation located next to the property of the International Paper facility.

As shown in Figure 4.74, the commercial system uses a total of four clusters, each one containing 45 Pelamis units (i.e., 180 total Pelamis WEC devices), connected to subsea cables. Each cluster consists of three rows with 15 devices per row. The other state designs are organized in a similar manner with four clusters. The number of devices per cluster varies such that each plant produces an annual energy output of 300,000 MWh/yr. The four subsea cables connect the clusters to shore as shown in Figure 4.75. The electrical interconnection of the devices is accomplished with flexible jumper cables, connecting the units in mid-water. The introduction of four independent subsea cables and the interconnection on the surface provide some redundancy in the wave farm arrangement [2].

Pelamis was used to establish the cost model for a commercial scale (300,000 MWh/yr) wave farm. Levelized cost components are shown in Figure 4.76 [78]. The cost breakdown shows that the impact on the cost of electricity of O&M (operation and maintenance)

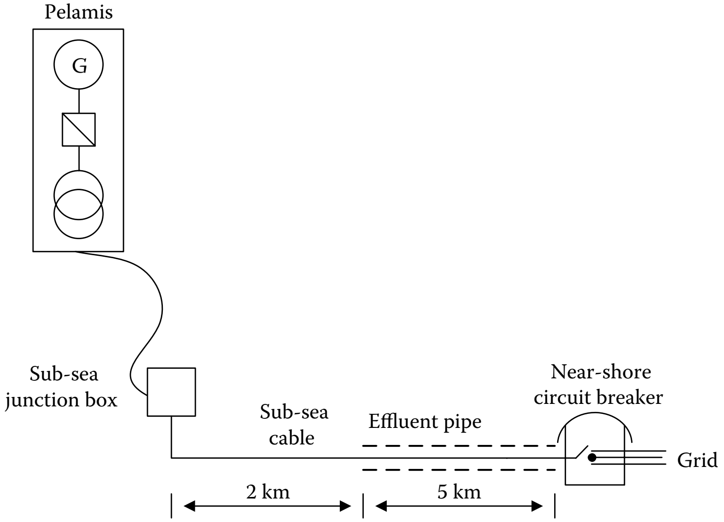

FIGURE 4.74 Electrical interconnection of Demo-Plant—in Oregon. (Redrawn from O. Siddiqui and R. Bedard. "Feasibility assessment of offshore wave and tidal current power production: A collaborative public/private partnership (Paper: 05GM0538)," EPRIsolutions, CA, *Proceedings of the IEEE Power Engineering Society 2005 Meeting Panel Session*, June 2005.)

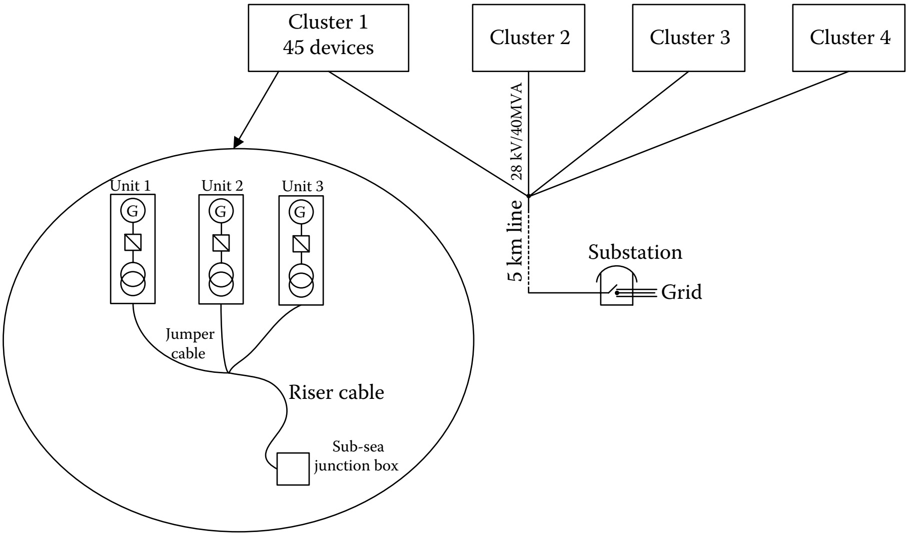

FIGURE 4.75 Electrical interconnection of Demo-Plant—Oregon Example.

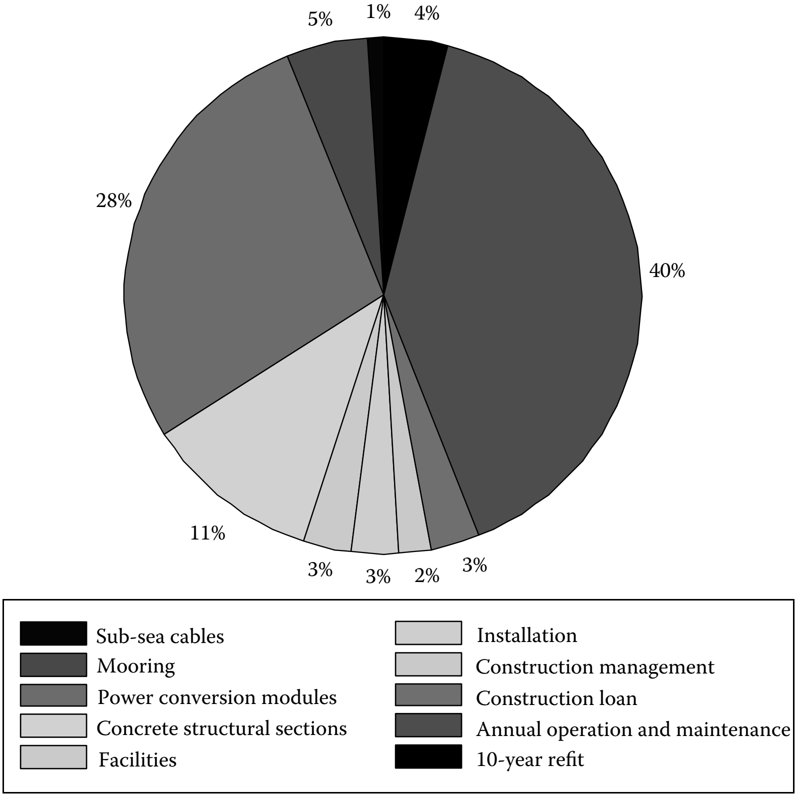

FIGURE 4.76 (**See color insert following page 80**.) Cost pie graph of the Pelamis WEC device.

is significant. The only way to bring the O&M costs down is by building demonstration projects. The second important impact of wave energy establishment is the power conversion modules.

4.4.3 Wave Dragon

The Wave Dragon is an overtopping device, which is developed by Wave Dragon Aps Company in Denmark [89]. Many other partner companies such as Spok ApS, Lowenmark Consulting Engineers FRI, Balslev, ESBI Engineering, and NIRAS AS contributed to the development processes. Wave Dragon is a floating offshore converter without any moving parts except the PTO system. The waves are channeled into a water reservoir with the aid of a wave reflector and a ramp. The reservoir is the main body of the device floating over the mean sea level. The operating principle of the Wave Dragon is shown in Figure 4.77.

The viewpoint of the Wave Dragon from the above is shown in Figure 4.78.

The reflector of the device welcomes the coming ocean waves and water is stored in the reservoir to flow through the turbine outlet channel. The potential energy is stored by taking the water into the reservoir. This potential energy helps in smoothing the generated power by regulating the water flow through the turbines. The reflector has two half-submerged rigid walls. These walls form a short narrowing channel and are wide open towards the sea and they are as high as the filling level of the reservoir. The power conversion stage includes several independent low-head water turbines [89]. These turbines are generally the Kaplan-type turbines discussed in Subsection 4.3.4.4.3 driving synchronous generators. The turbines are actively controlled so that the average amount of water is allowed to flow in order to reduce the power and voltage fluctuations. The front view of the device and the reflectors is shown in Figure 4.79, in which the reservoir is located between the reflectors to collect more amount of water carried by the waves.

In 2003, a prototype was deployed with seven turbines each with 20 kW rated power and driving individual PM generators. In 2004, this Wave Dragon started delivering power to the grid till 2005, which was damaged by a storm due to mooring failure [80].

4.4.4 AWS

Teamwork Technology located in the Netherlands is the developer company of the AWS, which is an offshore submerged device. The device is activated by the oscillations of static pressure caused by the surface waves. Figure 4.80 shows the operating principle of the AWS [80].

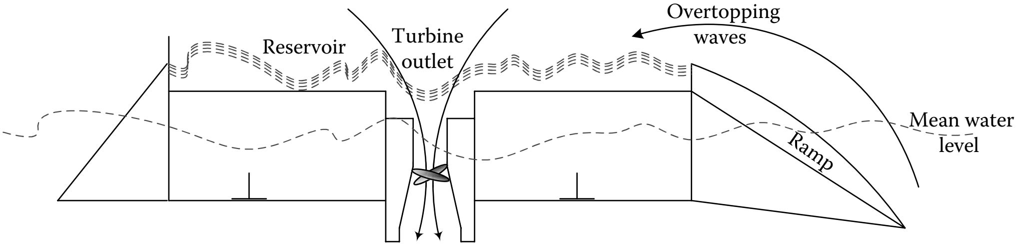

FIGURE 4.77 Operating principle of the Wave Dragon; waves overtop the ramp, water stored in a reservoir above the sea level and hydro turbines rotate as the water discharges.

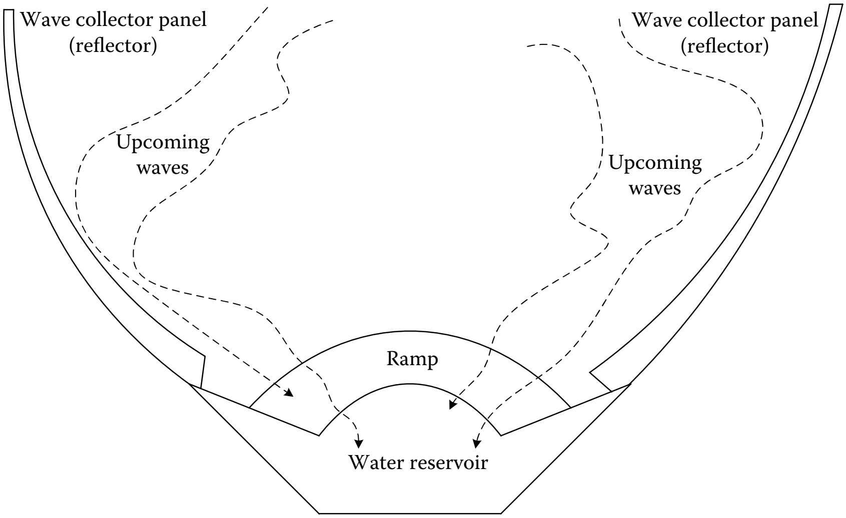

FIGURE 4.78 A bird's eye view of the Wave Dragon.

The AWS is an air-filled cylinder of which the floater is a body heaving up and down to or from the fixed bottom part. The waves create a pressure difference on the top of the device resulting in the force that moves the active part of the device. High water pressure causes the chamber volume to reduce if the wave crest is above the AWS. The floater heaves due to the action of the chamber pressure if the trough is above. Here "trough" represents the concave between the two wave crests. The behavior of the air in the chamber is similar to a spring with a variable stiffness by pumping water in or out of the chamber [80,91]. PM linear synchronous machines are used within the AWS applications as direct drive energy conversion devices. Using an auxiliary energy storage or conditioning, the efficiency of this type of energy conversion can be improved.

FIGURE 4.79 (**See color insert following page 80.**) Front view of the Wave Dragon with wave reflectors in the sides and the reservoir in the middle. (Courtesy of Wave Dragon ApS, available online at http://www.wavedragon.net/)

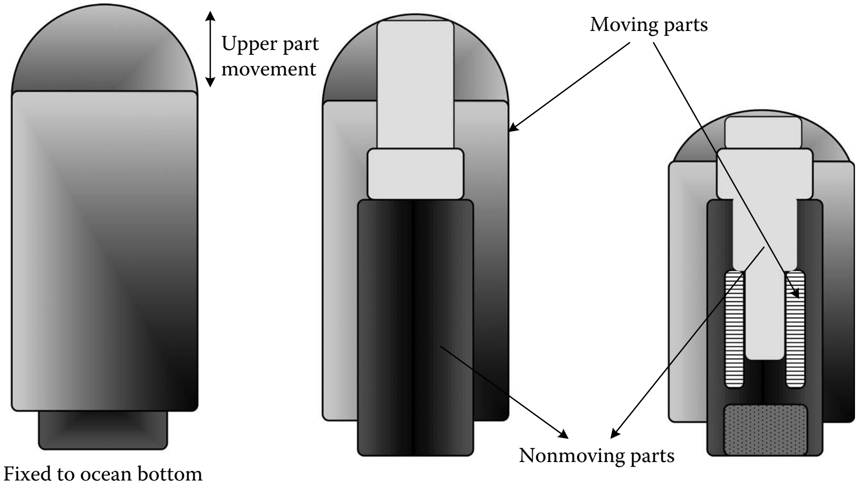

FIGURE 4.80 AWS operation principle.

The water dampers used within the AWS are actuated when the floating part approaches the mechanical end-stops. These dampers reduce the velocity of the floater and avoid the strong collision. Water dampers are also actuated with the electric generator when the floater does not have enough force required for adequate control of the movement of the AWS [91].

A 2 MW full-scaled AWS was built and deployed off the coast of Portuguese in nearly 40 m water depth [91]. The peak force the generator could have 1 MN (Mega-Newton) with 9 m width and 38 m height of the cylinder with a stroke of 7 m and maximum floater speed of 2.2 m/s.

The cylinder was placed within a steel cage on a fixed pontoon. On the fixed pontoon, there exist four ballasts, which have to be filled with water. The structure of the first version of AWS was large and expensive and was built to keep the first prototype safe in a place allowing just the floater to heave. The maintenance reduction via improvements of the generator design and building modular structures is being investigated by researchers [91].

4.4.5 Wave Star Energy

Wave Star is a device developed by Wave Star© Energy Company. Wave Star is fundamentally different from many other WEC devices. Instead of forming a barrier against the waves, upcoming waves are captured with an optimal wave movement angle. In this way, wave energy can be continuously captured, by the waves passing through the length of the machine. Wave Star© Energy is currently developing the first series production of a 500 kW wave energy converter [92]. Since July 2006, a small-scale grid-connected system has been in continuous operation. During the winter seasons from 2006 to 2008, there have been 12 major storms without causing any damage to the system. Testing of the first 500 kW device has been started in North Sea in late 2008 and it is expected that grid-connected Wave Star devices will be in operation in 2009.

There are 20 hemisphere-shaped floats that are partially submerged in the water along either side of the device as shown in Figure 4.81 [92]. The WSE is called a multipoint absorber, which means that a number of floating absorbers move upwards and downwards by an

FIGURE 4.81 View of the WSE, a multipoint absorber. (Courtesy of M. Kramer, "The wave energy converter: Wave Star, a multi point absorber system," Technical Report, Aalborg University and Wave Star Energy, Bremerhaven, Denmark.)

upcoming wave. In brief description, these movements activate the pumps, which press the hydraulic fluid to common transmission system, and drive a hydraulic motor.

When a wave rolls in, the floating absorbers in one side of the Wave Star are lifted up. Consequently, the floating absorbers of the other side will be lifted, until the wave subsides. There are individual hydraulic cylinders for each floating absorber. A piston in the cylinder applies pressure to the hydraulic fluid, inside the common transmission system of the device, when an absorber is lifted up. This pressure drives a hydraulic motor. This hydraulic motor drives a generator that produces electric power. Since the device has a length of several wavelengths, the system will operate continuously to harvest energy.

This device is storm-protected. During the storm periods, the absorbers can be lifted up to a safe position, that is, 20 m above the sea surface [92]. In Figure 4.82, the WSE is shown

FIGURE 4.82 (**See color insert following page 80**.) WSE position in storm protection mode. (Courtesy of M. Kramer, "The wave energy converter: Wave Star, a multi point absorber system," Technical Report, Aalborg University and Wave Star Energy, Bremerhaven, Denmark.)

in storm-protected position. Ahead of the device, a sensor on the sea surface measures the waves and ensures the automatic activation of the storm protection system. Moreover, absorbers can be controlled remotely through the Internet.

4.4.6 Magnetohydrodynamics Wave Energy Converter

MHD wave energy generator is a direct drive mechanical electrical energy converter and was developed by Scientific Applications & Research Associates (SARA) Inc. It is a cost-effective solution and promises to cut the costs of WEC systems by a factor of three. SARA Inc. is working on developing a 100 kW MHD unit [93,94]. This device is efficient and has high power density. The main benefit is that it is not composed of any conventional rotating electric generator. Although the output of the device has very high current and low voltage, using power electronic converters the output can be converted to practical and usable current and voltage levels.

The magnetohydrodynamics wave energy converter (MWEC) device couples the up and down motion of the heave caused by ocean waves. The wave motion is transferred by a shaft to the MHD generator that is deep under water. This shaft forces the conducting fluid through strong PMs. Therefore, this MWEC generator works on the principle that flowing seawater can conduct electric current by the aid of a strong magnetic field unlike the other MHD generators. In the operation, the seawater from the over passing waves is taken in. Then, the seawater flows through a hollow tube with flared inlet and outlet sections. These sections boost the water velocity according to the Bernoulli principle. According to this principle, if any fluid moves from a region of high pressure to a region of low pressure its speed increases. Vice versa, the speed of a fluid decreases if the fluid moves from a region of lower pressure to a region of high pressure. Strong electromagnets generate magnetic field perpendicular to the water flow. The electric current is stimulated in the passing seawater by the strong magnetic field. The electrodes placed in the tube are used to collect this electric current.

As claimed by the manufacturer, the MWEC system has several advantages such as high efficiency, capability of operating in shallow sea levels, compactness, rapid and easy deployment, high efficiency, and reliability. There are no gears, turbines, drive belts, bearings, or transmission systems. Therefore, capital needs and maintenance costs are low. MWEC is a quiet and environmental friendly device with zero greenhouse gas emissions [94].

4.5 Wave Energy in Future

Wave energy is a promising renewable energy source for future. Nearshore devices are expected to grow in size. However, due to their higher cost, longer installation period and shortage of available locations, offshore wave energy applications will be more feasible in the long term [95–97].

The wave energy development process consists of three phases. The first phase involves deployment of small-scale prototype devices. In the second phase with more funding from the government and investors, these prototypes will be improved and promising devices will installed. In the final phase, the production of grid-connected, full scale wave energy converters will be installed in farm-style configurations. Hundreds of prototype devices have been proposed but only 20 of them stepped up to the second phase and some of them are really close to the final stage and commercial deployment [96].

In order to test the durability and efficiency issues, large-scale demonstration projects are required, which have not been available yet. However, systems should be tested in their final state to assess their potential.

Over the next 5 years, the United Kingdom is expected to play a very dominant role with a forecast capacity of 10.6 MW, which is nearly half the market share. Denmark, Australia, and Portugal are the other significant markets with some projected installations. However, they lag behind the U.K. With the reasonable levels of support from the government, a number of advanced wave technologies developed recently in these countries. The U.S. market also shows increased interest in wave energy technologies; however, more research and industry involvement is required [96].

4.6 Summary

This chapter focuses on the ocean wave energy harvesting in which the kinetic and potential energy contained in the natural oscillations of ocean waves is converted into electric power. Nearshore and offshore approaches along with required absorber, turbine, and generator types are discussed. Moreover, power electronic interfaces for grid-connection scenarios for each of the possible topologies are explained. In the final sections of the chapter, commercialized ocean WEC applications and the ocean wave energy development in the future are presented.

References

1. Ocean Energy: Technology Overview, Renewable Development Initiative, available online: http://ebrdrenewables.com/sites/renew/ocean.aspx.
2. O. Siddiqui and R. Bedard. "Feasibility assessment of offshore wave and tidal current power production: A collaborative public/private partnership (Paper: 05GM0538)," EPRIsolutions, CA, *Proceedings of the IEEE Power Engineering Society 2005 Meeting Panel Session*, June 2005.
3. J.N. Newman, "The interaction of stationary vessels with regular waves," *Proceedings of the 11th Conference on Naval Hydrodynamics*, London, 1976.
4. W.J. Jones and M. Ruane, "Alternative electrical energy sources for Maine, Appendix I, wave energy conversion by J. Mays," Report No. MIT-E1 77-010, MIT Energy Laboratory, July 1977.
5. B. Kinsman, *Wind Waves*, Englewood Cliffs, NJ: Prentice-Hall, 1965.
6. S.H. Salter, "Wave power," *Nature*, 249, 720–724, 1974.
7. S.H. Salter, "Characteristics of a rocking wave power device," *Nature*, 254, 504–506, 1975.
8. M. Wolley and J. Platts, "Energy on the crest of a wave," *New Scientist*, 66, 241–243, 1975.
9. H. Kayser, "Energy generation from sea waves," *Proceedings of the Ocean 1974 IEEE Conference*, Halifax, NS, Canada, Vol. 1, pp. 240–243, 1974.
10. J.D. Isaacs, G.L. Wick, and W.R. Schmitt, "Utilization of energy from ocean waves," *Proceedings of the Wave and Salinity Gradient Energy Conversion Workshop*, University of Delaware, pp. F1–F36, May 1976.
11. J.B. Isaacs, D. Caste1, and G.L. Wick, "Utilization of the energy in ocean waves," *Ocean Engineering*, 3, 175–187, 1976.
12. M.E. McComick, "A modified linear analysis of a wave energy conversion buoy," *Ocean Engineering*, 3, 133–144, 1976.

13. J.D. Isaacs and R.J. Seymour, "The ocean as a power source," *International Journal of Environmental Studies*, 4, 201–205, 1974.
14. "Ocean Energy," Report of the U.S. Department of Interior Minerals Management Service, available at http://www.mms.gov/mmsKids/PDFs/OceanEnergyMMS.pdf, retrieved in May 2009.
15. S.H. Salter, D.C. Jeffrey, and J.R.M. Taylor, "The architecture of nodding duck wave power generators," *The Naval Architect*, London, 15, 21–24, 1976.
16. R.E. Dingwell, "Predictions of power production by a cam type wave energy converter for various locations," MSc dissertation, MIT, 1977.
17. L.S. Slotta, "Recoverable wave power concepts," ERDA Report No. COO-2946-1, 1976.
18. M.E. McCormik and Y.C. Kim, "Utilization of ocean waves—wave to energy conversion," *Proceedings of the International Symposium: Scripps Institute of Oceanography*, 1986.
19. N.A. Tornqvist, "Theoretical analyses of some simple wave power devices," *International Journal of Energy Research*, 2 (3), 281–294, 2007.
20. A.F. Richards, "Extracting energy from the oceans," *Marine Technical Society Journal*, 10 (2), February–March, 1976.
21. K. Budal, "Theory for absorption of wave power by a system of interacting bodies," *Journal of Ship Research*, 1977.
22. L. Duckers, "Wave power," *IET Engineering Science and Educational Journal*, 9 (3), 113–122, 2000.
23. F. Huang and W C. Beattie, "Modeling and simulation of the Islay wave power conversion system," *Proceedings of the IEEE International Electric Machines and Drives Conference Record*, pp. 2/2.1–2/2.4, May 1997.
24. C.E. Tindall and X. Mingzhou, "Optimising a wells-turbine-type wave energy system," *IEEE Transactions of Energy Conversion*, 11 (3), 631–635, 1996.
25. T.H. Kim, T. Setoguchi, M. Takao, K. Kaneko, and S. Santhaumar, "Study of turbine with self-pitch-controlled blades for wave energy conversion," *International Journal of Thermal Sciences*, 41, 101–107, 2002.
26. T. Miyazaki, "Utilization of coastal seas by floating wave energy device 'Mighty Whale'," *Proceedings of the European Wave Energy Symposium*, Edinburgh, pp. 373–378, 1993.
27. Y. Washio, H. Osawa, Y. Nagata, F. Fujii, H. Furuyama, and T. Fujita, "The offshore floating type wave power device 'Mighty Whale': Open sea tests," *Proceedings of the 10th International Offshore and Polar Engineering Conference*, ISOPE, Seattle, Vol. 1, pp. 373–380, 2000.
28. S. Santhakumar, V. Jayashankar, M.A. Atmanand, A.G. Pathak, M. Ravindran, T. Setoguchi, M. Takao, and K. Kaneko, "Performance of an impulse turbine based wave energy plant," *Proceedings of the Eighth International Offshore and Polar Engineering. Conference*, ISOPE, Vol. 1, pp. 75–80, 1998.
29. A.F. de O. Falcão, T.J.T. Whittaker, and A.W. Lewis, "JOULE II preliminary action: European pilot plant study," *Proceedings of the European Wave Energy Symposium*, Edinburgh, pp. 247–257, 1993.
30. M. Inoue, K. Kaneko, T. Setoguchi, and K. Shimamoto, "Studies on wells turbine for wave power generator (Part 4; Starting and running characteristics in periodically oscillating flow)," *Bulletin of JSME*, 29 (250), 1177–1182, 1986.
31. M. Brezovec, I. Kuzle, and T. Tomisa, "Nonlinear digital simulation model of hydraulic power unit with Kaplan turbine," *IEEE Transactions on Energy Conversion*, 21 (1), 235–241, March 2006.
32. T. Setoguchi, K. Kaneko, H. Hamakawa, and M. Inoue, "Some techniques to improve the performance of biplane Wells turbine for wave power generator," *Proceedings of the 1st Pacific/Asia Offshore Mechanics Symposium*, The International Society of Offshore and Polar Engineers, Seoul, Korea, Vol. 1, pp. 207–212, 1990.
33. T. Setoguchi, K. Kaneko, H. Taniyama, H. Maeda, and M. Inoue, "Impulse turbine with self pitch-controlled guide vanes connected by links," *International Journal of Offshore Polar Engineering*, 6 (1), 76–80, 1996.
34. T. Setoguchi, M. Takao, Y. Kinoue, K. Kaneko, and M. Inoue, "Study on an impulse turbine for wave energy conversion," *Proceedings of the Ninth International Offshore and Polar Engineering*

Conference, The International Society of Offshore and Polar Engineering, Brest, France, Vol. 1, pp. 180–187, 1999.

35. T.H. Kim, M. Takao, T. Setoguchi, K. Kaneko, and M. Inoue, "Performance comparison of turbines for wave power conversion," *International Journal of Thermal Science*, 40 (7), 681–689, 2001.
36. M. Hineno and Y. Yamauchi, "Spectrum of sea wave," *Journal of the Society of Naval Architecture*. Japan, 609, 160–180, 1980.
37. T. Omholt, "A wave activated electric generator," *Oceans*, 10, 585–589, 1978.
38. H. Luan, O. Onar, and A. Khaligh, "Dynamic modeling and optimum load control of a PM linear generator for ocean wave energy harvesting application," *Proceedings of the IEEE 34*th *Applied Power Electronics Conference and Exposition*, Washington, DC, February 2009.
39. M.A. Muller, "Electric generators for direct drive energy converters," *Proceedings of the IEE General, Transactions and Distribution*, 49 (4), 446–456, 2002.
40. M.A. Muller and N.J. Baker, "A low speed reciprocating permanent magnet generators for direct drive wave energy converters," *Proceedings of the Power Electronics, Machine Drives*, no. 487, pp. 16–18, April 2002.
41. A. Wolfbrandt, "Automated design of a linear generator for wave energy Converters-a simplified model," *IEEE Transactions. on Magnetics*, 42 (7), 1812–1819, 2007.
42. M. Leijon, H. Bernhoff, O. Ågren, J. Isberg, J. Sundberg, M. Berg, K.-E. Karlsson, and A. Wolfbrandt, "Multi-physics simulation of wave energy to electric energy conversion by permanent magnet linear generator," *IEEE Transactions on Energy Conversion*, 20 (1), 219–224, 2005.
43. J. Falnes, *Ocean Waves and Oscillation Systems*, Cambridge, U.K.: Cambridge University Press, p. 221, 2002.
44. K. Budal and J. Falnes, "A resonant point absorber of ocean waves," *Nature*, 256, 478–479, 1975 (with Corrigendium in vol. 257, p. 626).
45. D.V. Evans, "A theory for wave-power absorption by oscillating bodies," *Journal of Fluid Mechanics*, 77, 1–25, 1976.
46. J.N. Newman, "The interaction of stationary vessels with regular waves," *Proceedings of the 11th Symposium on Naval Hydrodynamics*, London, pp. 491–501, 1976.
47. G. Bertotti, A. Boglietti, M. Chiampi, D. Chiarabaglio, F. Fiorillo, and M. Lazzari, "An improved estimation of iron losses in rotating electrical machines," *IEEE Transactions in Magnetics*, 27 (6), 5007–5509, Nov. 1991.
48. C.S. Hoong and S. Taib, "Development of three phase synchronous generator for ocean wave application," *Proceedings of the Power Engineering Conference*, Vol. 15–16, pp. 262–267, December 2003.
49. L. Drouen, J.F. Charpentier, E. Semail, and S. Clenet, "Study of an innovative electrical machine fitted to marine current turbines," *Proceedings of the Oceans 2007 Europa*, 18–21, pp. 1–6, 2007.
50. S.M. Abu-Sharkh, S.H. Lai, and S.R. Turnock "Structurally integrated brushless PM motor for miniature propeller thrusters," *IEE Proceedings of the Electronics Power Applications*, 151 (5), 513–519, 2004.
51. O. Krovel, R. Nilssen, S.E. Skaar, E. Lovli, N. Sandoy, "Design of an integrated 100 kW permanent magnet synchronous machine in a prototype thruster for ship propulsion," *Proceedings of the ICEM'*2004, Cracow, Poland, pp. 117–118, September 2004.
52. M. Lea et al., "Scale model testing of a commercial rim-driven propulsor pod," *Journal of Ship Production*, 19 (2), 121–130, 2003.
53. A. Grauers, "Design of direct-driven permanent-magnet generators for wind turbines," PhD dissertation, Chalmers University of Technology, Goteburg, Sweden, 1996.
54. A. Grauers and P. Kasinathan, "Force density limits in low-speed permanent magnet machines due to temperature and reactance," *IEEE Transactions on Energy Conversion*, 19 (3), 518–525, 2004
55. Z.Q. Zhu, D. Howe, E. Bolte, and B. Ackermann, "Instantaneous magnetic field distribution in brushless permanent magnet dc motors, Parts I to IV," *IEEE Transactions on Magnetics*, 29 (1), 124–158, 1993.

56. H. Polinder van der Pijl, G.J. de Vilder, and P. Tavner, "Comparison of direct-drive and geared generator concepts for wind turbines," *IEEE Transactions on Energy Conversion*, 21 (3), 725–733, 2006.
57. P.V. Indiresan and S.S. Murthy, "Generating electrical power from the wave energy—the Indian experiment," *Proceedings of the 24*th *Energy Conversion Engineering Conference*, Vol. 5, pp. 2121–2126, August 1989.
58. A.L. Naikodi and G.S. Rao, "Efficient operation of AC voltage controller fed induction machine for wave power generation," *Proceedings of the International Conference on Power Electronics, Drives and Energy Systems for Industrial Growth*, Vol. 1, pp. 265–270, January 1996.
59. J. Vaidya and E. Gregory, "Advanced electric generator & control for high speed micro/mini turbine based power systems," patent pending.
60. P.C. Krause, O. Wasynczuk, and S.D. Sudhoff, *Analysis of Electric Machinery*, New York: Wiley–IEEE Press, 2002.
61. D.A. Torrey, X.M. Niu, and E.J. Unkauf, "Analytical modelling of variable-reluctance machine magnetisation characteristics," *IEE Proceedings—Electric Power Applications*, 142 (1), 14–22, 1995.
62. H. Polinder, B.C. Mecrow, A.G. Jack, P.G. Dickson, and M.A. Muller, "Conventional and TFPM linear generators for direct drive wave energy conversion," *IEEE Transactions on Energy Conversion*, 20 (2), pp. 260–267, 2005.
63. T.J.E. Miller, *Switched Reluctance Motors and Their Control*, Oxford, U.K.: Magna Physics Clarendon, 1993.
64. G.W. Taylor, J.R. Burns, S.M. Kammannm, W.B. Powers, and T.R. Welsh, "The Energy Harvesting Eel: a small subsurface ocean/river power generator," *IEEE Journal of Oceanic Engineering*, 26 (4), 539–547, 2001.
65. J. Allen, *Proceedings of the IUTAM Symposium Bluff Body Wakes and Vortex Induced Vibrations*, Marseille, France, June 13–16, 2000.
66. V. Schmidt, "Theoretical power output per unit volume of PVF and mechanical to electrical conversion efficiencies as function of frequency," *Proceedings of the IEEE Sixth International Symposium on Applications of Ferroelectrics*, Bethlehem, PA, June 8–11, 1986.
67. K. Thorburn and M. Leijon, "Farm size comparison with analytical model of linear generator wave energy converters," *Ocean Engineering*, 34, 908–916, 2006.
68. M. Molinas, O. Skjervheim, P. Anderson, T. Undeland, J. Hals, T. Moan, and B. Sorby, "Power electronics as grid interface for actively controlled wave energy converters," *Proceedings of the International Conference on Clean Electrical Power ICEEP*, pp. 188–195, May 2007.
69. N.G. Hingorani and L. Gyugyi, *Understanding FACTS; Concepts and Technology of Flexible AC Transmission Systems*, IEEE Press, New York, 2000.
70. M. Molinas, J. Kondoh, J.A. Suul, and T. Undeland,"Reactive support for wind and wave farms with a STATCOM for integration into the power system," *Proceedings of the International Conference Renewable Energy 2006*, Japan, October 2006.
71. J. Svensson, P. Jones, and P. Halvarsson, "Improved power system stability and reliability using innovative energy storage devices," *Proceedings of the Eigth IEE International Conference on AC and DC Power Transmission*, ACDC 2006, pp. 220–224, March 2006.
72. B. Naess, M. Molinas, and T. Undeland, "Laboratory tests of ride through for doubly fed induction generators," *Proceedings of the Nordic Wind Power Conference NWPC 2006*, Espoo, Finland, May 2006.
73. F. Blaabjerg, Z. Chen, and S.B. Kjaer, "Power electronics as efficient interface in dispersed power generation systems," *IEEE Transactions on Energy Conversion*, 19 (5), 1184–1194, 2004.
74. R. Pena, J.C. Clare, and G.M. Asher, "Doubly fed induction generator using back-to-back PWM converters and its application to variable-speed wind-energy generation," *IEE Proceedings–Electronic Power Applications*, 143 (3), 1996.
75. P. Lobato, A. Cruz, J. Silva, and A.J. Pires, "The switched reluctance generator for wind power generation," *Proceedings of the IEEE PES Conference Asociación Española para el Desarrollo de la Ingeniería Eléctrica*, 2009.
76. P.J. Lawrenson, J.M. Stephenson, P.T. Blenkinsop, J. Corda, and N.N. Fulton, "Variable-speed switched reluctance motors," *IEE Proceedings*, 127, Part B, (4), 253–265, 1980.

77. V. Nedic and T.A. Lipo, "Experimental verification of induced voltage self-excitation of a switched reluctance generator," *Proceedings of the IEEE Industry Applications Conference*, Vol. 1, pp. 51–56, 2000.
78. M. Presivic, "Wave power technologies (Paper 05GM0542)," Electric Power Research Institute, Palo Alto, CA., *Proceedings of the IEEE Power Engineering Society 2005 Meeting Panel Session*, June 2005.
79. R.S. Tseng, R.H. Wu, and C.C. Huang, "Model study of a shoreline wave-power system," *Ocean Engineering*, 27 (8), 801–821, August 2000.
80. H. Polinder and M. Scuotto, "Wave energy converters and their impact on power systems," *Proceedings of the International Conference on Future Power Systems*, pp. 1–9, November 2005.
81. O. AF Falcao, "The shoreline OWC wave power plant at the Azores," *Proceedings of the Fourth European Wave Energy Conference*, Aalborg, Denmark, pp. 42–48, 2000.
82. J. Falnes, *Ocean Waves and Oscillating Systems*, Cambridge: Cambridge University Press, 2002.
83. M. Vantorre, R. Banasiak, and R. Verhoeven, "Modeling of hydraulic performance and wave energy extraction by a point absorber in heave," *Applied Ocean Research*, 26, 61–72, 2004.
84. C. Josset and A.H. Clement, "A time domain numerical simulator for oscillating water column wave power plants," *Renewable Energy*, 32, 1379–1402, 2007.
85. J.M. Paixao Conde and L.M.C Gato, "Numerical study of the air-flow in an oscillating water column wave energy converter," *Renewable Energy*, 33, 2637–2644, 2008.
86. R. Yemm, R. Henderson, and C. Taylor, "The OPD Pelamis WEC, current status and onward programme," *Proceedings of the Fourth European Wave Energy Conference*, Aalborg Denmark, 2000.
87. Pelamis Wave Power Ltd., available online at http://www.pelamiswave.com
88. R. Henderson, "Design, simulation, and testing of a novel hydraulic power take-off system for the Pelamis wave energy converter," *Renewable Energy*, 31 (2), 271–283, 2006.
89. J.P. Kofoed, P. Frigaard, E.F. Madsen, and H. Chr. Soransen, "Prototype testing of the wave energy converter wave dragon," *Renewable Energy*, 31 (2), 181–189, 2006.
90. Wave Dragon ApS, available online at http://www.wavedragon.net/
91. D. Valerio, P. Beirao, and J.S. da Costa, "Optimization of wave energy extraction with the Archimedes Wave Swing," *Ocean Engineering*, 34 (17–18), 2330–2344, 2007.
92. M. Kramer, "The wave energy converter: Wave Star, a multi point absorber system," Technical Report, Aalborg University and Wave Star Energy, Bremerhaven, Denmark.
93. T.M. Rynne, "Ocean wave energy conversion system," U.S. Patent 5,136,173, to Scientific Applications & Research Associates, Inc., Patent and Trademark Office, Washington, DC, 1991.
94. MWEC, A power take off solution to convert the forces from ocean wave motion to usable electricity, Scientific Applications and Research Associates Incorporated (SARA Inc.), available online: http://www.sara.com/RAE/pdf/MWEC_infosheet.pdf
95. A.T. Jones and A. Westwood, "Recent progress in offshore renewable energy technology development," *Proceedings IEEE Power Engineering Society 2005 Meeting Panel Session*, June 2005.
96. A.T. Jones and A. Westwood, "Economic forecast for renewable ocean energy technologies," *Proceedings of the Energy Ocean 2004*, Palm Beach, Florida, 2004.
97. A.T. Jones and W. Rowley, "Global perspective: Economic forecast for renewable ocean energy technologies," *MTS Journal*, 36 (4), 85–90, Winter 2002.